Contents

A Spectroscopical and Photochemical study on Covalent and Non-Covalent Bonds

Federico Mazzoni

31/12/2014

Chapter 1

Introduction

Spectroscopy and photochemistry. Molecular spectroscopy was born for the study of molecular properties like electronic, vibrational and rotational levels, that are related to the energetic and to the structure of chemical systems. As in many areas of pure research and applied sciences the need of a reliable theoretical modeling of molecular materials was growing drastically, spectroscopical data became crucial and have also been used as benchmark for the development of fast and accurate computational approaches.

Nowadays, modern spectroscopy is focused to extend our knowledge to always more complex systems, such as biologically interesting molecules and supramolecular adducts like weakly bounded systems and organometallic complexes. But complexity requires, to be studied, a major capability from the user and therefore a big effort is also addressed to the development of new experimental methods.

First of all, we need to spend a few words on what we mean by complexity and complex system. Increasing molecular size, changes in structure, presence of substituents or ethero-atoms, presence and conjugation of

multiple bonds, they all contribute to complexity of a molecular system. Anyway, a molecular system of small size is not necessarily a simple system and a molecular system of big size can be very simple to study. The complexity of a chemical system is indeed related to the kind of property or behaviour we are interested in. A triatomic molecule like water for example shows very interesting properties whose study and interpretation is not straightforward at all, as its ability to form hydrogen bonds and its effect as proton acceptor or donor. Moreover, complexity is related to the environmental conditions: pressure, temperature, presence of solvents or solutes, chemical impurities, are all factors that determine the behaviour of a chemical system. Water is again a very useful and interesting example, as in the very last years it was proved that, changing pressure and temperature by several orders of magnitude, in the phase diagram two different liquid phases are present, high-density water and low-density water, with a well defined phase transition.[1,2]

From the experimental point of view, the first step in the analysis of chemical species is the sample preparation. If, for example, for an UV analysis with a fluorometer the sample is liquid at ambient temperature and pressure, filling a cuvette is all we need to do. If instead, we are interested in properties of the single molecule, or of a limited group of molecules, we probably need to spend much more time in the sample preparation. In general, this requires to isolate the molecular system of interest from the chemical environment or to control and study also the chemical environment. Then, it requires to prepare a given initial set of quantum states, whether it can be described classically by pressure and temperature at the chemical equilibrium or out of this condition. For the finest analysis for example, a really narrow set of quantum states is prepared. To reach the desired conditions, modern experiments allow for the study of extremely

different conditions: pressure for example can range for more than 16 orders of magnitude and temperature from almost $0K$ up to 10^3K.[1,3–6] Once the desired initial conditions are reached, spectroscopic analysis starts: the properties of the system are probed. Optical spectroscopy concerns the interaction between light and matter. Different light sources can be used, starting from black bodies to different kind of lamps. The most used light sources are obviously lasers because of their unique properties in brightness, short pulse duration or narrow bandwidth, coherence. Only using lasers it is indeed possible to observe phenomena like Raman effect or multiphoton absorption. Moreover, in special cases, light from high power sources can induce other non-linear processes in matter: for example the laser radiation can be frequency doubled (or eventually tripled) just by passing through a material with high non linear optical properties (provided specific boundary conditions are satisfied).[7]

After the excitation, an observable of the light-matter interaction must be monitored. It can be the depletion of the exciting light intensity in case of absorption, the emission of secondary radiation in case of fluorescence or phosphorescence, the production of charged particles in ionization processes as will be described later in details.

In the spectroscopical analysis the quantum state of the sample changes. Usually, the chemical composition of the sample is the same before and after the analysis. Anyway, some photochemical transformation can occur, e.g. ionization, isomerization, dissociation, polymerization. Then, the different chemical products have to be monitored in their chemical identity and in their spatial distribution. A deep understanding of the chemical process and its energetics can be obtained. Moreover, it is possible to study the kinetics of even the fastest processes with time resolved experiments.

Any chemical transformation is connected to the breaking and/or the

formation of chemical bonds between atoms. It is therefore important to study in depth the nature and the properties of the chemical bond for the comprehension of transformation dynamics. Different interactions are possible between atoms: from covalent bonds to dispersion interactions. Covalent bonds between atoms, for example, are responsible for the formation of molecules, while different molecules can interact together thank to multipolar interactions and van der Waals forces. Organic molecules can indeed interact with other molecules and atoms forming weakly bonded complexes. In aromatic molecules, for example, π-orbitals are present. An interaction of these conjugated systems with other molecules or atoms is possible, due to π-stacking interactions (e.g. anisole dimer[8]) or to multipolar (dipole-dipole, quadrupole-quadrupole and so on) interactions (e.g. benzene dimer[9,10]). Molecules where an OH group or an NH group is present can give origin to H-bonded clusters (e.g. phenol-water[11]). Aromatic molecules with different substituent can interact together in a subtle balance of different interactions (e.g. anisole-phenol cluster[12]).

Non-covalent interactions. Weak non-covalent interactions between molecules are present almost everywhere around us and even inside us. The role that they play in nature and life processes is not really less relevant than their diffusion: folding of proteins, DNA helical shape, interactions enzyme-substrate, interactions drug-target and much more.[13] In order to clarify how important they are, we will briefly focus on the role these interactions play for example in DNA folding. As it's widely known DNA is a double chain of nucleotides, each chain is held together by covalent bonds formed by deoxyribose and phosphate groups, then the nucleobases (Adenine, Guanine, Thymine, Cytosine) are side substituents of deoxyribose units. Each nucleobase interacts in the chain with its neighbors thank to $\pi - \pi$ interactions and with nucleobases on the other chain thanks to H bonds. As result of the

balance between these non-covalent interactions the DNA structure is not just double, but also twisted as an helix with the hydrophilic groups (phosphate, deoxyribose) pointing out and the hydrophobic core (nucleobases) packaged inside. Non-covalent interactions are therefore responsible for reactivity and functions of DNA.

As it's obvious the growing interest for weak interactions has lead to extensive studies over the last years,[14] when several new techniques were developed in order to overcome the problems that, in the past, made experiments on weakly bonded systems not straightforward. Indeed, as already mentioned before, we're dealing with complexity: an excellent control capability is necessary.

A quite common way to study model systems for the spectroscopical characterization of weak interactions is to produce them in the gas phase at very low temperatures through an adiabatic, supersonic expansion, using a carrier gas (usually Helium or Argon) flowing onto the compounds of interest.[15] In such a way, molecules and supramolecular aggregates that can form during the expansion are isolated from the environment and prepared in the ground state. If the number of collisions during the first moments of the expansion is small enough, it is highly probable that the compounds of interest survive as long as they can be studied with laser techniques.

Spectroscopy on jet cooled molecules. Linear and non-linear spectroscopic techniques have been widely employed in studies on jet cooled molecules. Linear spectroscopies imply a response from the system that is linearly proportional to the power of the exciting radiation as the absorbed light intensity I(x) in the Lambert Beer law.

$$I(x) = I_0 e^{-\alpha c x} \tag{1.1}$$

Where α is the molar extinction coefficient, c is the concentration of the sample and x is the path length of light through the sample. However, the density of molecules is very low in molecular beams and the path length very short. The absorption of jet cooled molecules is therefore extremely hard to monitor, and different techniques with higher sensitivity are more suitable. Typical experiment with linear response is the Laser Induced Fluorescence (LIF): the sample is excited with a laser beam of suitable energy to promote the population of an excited level of the system, usually a single vibronic level. Indeed, lasers with a spectral purity of $\Delta\nu/\nu \simeq 10^{-5}$ (about $1cm^{-1}$ for UV-VIS) are typically employed. After the perturbation, the excited level population possibly decays with the emission of photons. Photons are therefore a suitable observable for spectroscopy: the total emission of photons can be monitored as a function of the exciting wavelength (integrated fluorescence) or, for a fixed exciting wavelength, the wavelength of the emitted photon can be studied (dispersed fluorescence).

A very powerful technique used for gas phase samples is the High Resolution LIF (HR-LIF),[16–18] that allows for the measurement of rotationally resolved vibronic spectra. In this experiment a continuous laser beam with an extremely narrow bandwidth ($\Delta\nu/\nu \simeq 10^{-9}$), is used for the excitation of the sample prepared in a molecular beam. The integrated fluorescence signal emitted is recorded as a function of the exciting wavelength. After data analysis, rotational constants of the system in both ground and excited state can be obtained, allowing for the reconstruction of structural information and the comparison with finest quantum calculations. Anyway, since it is not possible to immediately correlate emitted photons and emitting chemical species, a serious limitation to this kind of analysis exists. For this reason LIF is usually coupled with different techniques (i.e. ionization followed by mass analysis of the resulting ions) in order to recognize the

contribution of the different chemical species present in the environment to the observed signal.

Non-linear spectroscopies are instead based on the absorption of high-power radiation, usually produced by pulsed lasers. High power radiation interacts with matter in different ways. Different processes can occur, like the multiphoton absorption of light from the sample. The absorption of more than one photon is usually an extremely improbable process. This is related to the transition rate, that in the simplest and more probable case of the two-photon absorption from an initial a state to a final b state through a single intermediate virtual state k can be written as:

$$\Gamma_{ab}^{(2)} \propto \frac{|D_{ka}^{(2)}|^2 D_{bk}^{(2)}|^2}{\Delta^2} I_1 I_2 \tag{1.2}$$

with

$$\Delta = \omega_1 - \omega_{ak} \tag{1.3}$$

being the detuning of the first laser with respect to the ak transition and $D_{ka}^{(2)}$ and $D_{bk}^{(2)}$ being the transition moments respectively for $a \rightarrow k$ and $k \rightarrow b$.

If the detuning term is big, then this transition probability is negligible. Only when the resonance $\omega_1 = \omega_{ka}$ is reached and k represent a real state so that the transition moment is large enough, an enhancement of the absorption rate is obtained. A schematic representation of the two photon absorption processes is reported in fig. 1.1

Multiphoton absorption is the basis for Resonance Enhanced two-Photons Ionization (R2PI) spectroscopy.[19,20] Also this technique will be presented in details later on, but it is important to note here that if the experiment is carried on using UV radiation, then the sample molecules can be excited

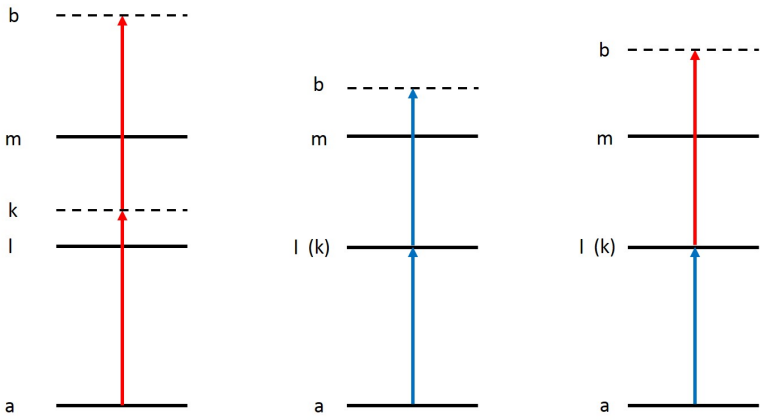

Figure 1.1: *Two photon absorption processes: off resonance (left), resonant absorption with two photons of the same wavelngth (center), resonant two photon absorption with two photons of different wavelength (right). Quantum states are labeled: initial (a), final (b), intermediate (k), excited (l,m)*

well above the ionization threshold, so that at least two charged particles (ion and electron) are produced and can be detected. In this latter case a mass spectrometer is used to record the signal, so it is possible to separate, thanks to their different charge to mass ratio, the contribution to the total production of ions of different species. It is therefore possible to study molecular properties even in a gas mixture.[21,22]

The same mass detection system can be used for electron detection even if, obviously, almost the same limitation already mentioned for fluorescence spectroscopy exists: electrons coming from different species they all hit the detector at the same time because they all have the same charge to mass ratio. Anyway, once an electronic transition of a given species has been determined by means of ionization spectroscopy coupled to an ion mass selective detection, the excitation wavelength can be set to this value

and electrons produced in the ionization process can be collected. When energy is transferred from internal modes to kinetic energy release (KER) of the particles involved, as in case of photoionization or photodissociation, then the mass detection scheme can be coupled with a position sensitive detector in order to reconstruct the energetical information they carry on. This allows for the reconstruction of different molecular properties: in the case of the *Electron Imaging* for example, the ionic vibrational spectrum of the system is obtained and the measure of its Ionization Potential (IP) is possible.

The energy resolution limiting factors are mainly four in the case of resonant experiments: bandwidth of the exciting laser, homogeneous and inhomogenous broadening of the bands in the spectrum, detector maximum resolution. Nanosecond pulsed lasers have narrow bands in the order of $1 - 0.1 cm^{-1}$, so they are not so relevant as limiting factors, allowing also for the resolution of rotational contour of vibronic bands. The maximum energy resolution of detector is a serious limitation for example in the case of dispersed fluorescence, where the slit width choice is crucial for the desired accuracy in results, and in Ion Imaging experiments (see chapter 2). Homogeneous broadening of the bands in the spectrum is due to the nature of the involved excited state and in particular to its lifetime (τ in eq. 1.4) by the energy-time formulation of the uncertainty principle:

$$\tau \delta E \geq \frac{1}{2}\hbar \tag{1.4}$$

whereas inhomogeneous broadening in gas phase experiments comes mainly from the Doppler effect and is therefore related the experimental configuration. Ionization experiments are indeed optimized to minimize this latter problem: using a supersonic beam as source and crossing it perpendicularly

with the laser beam, the Doppler effect can be effectively reduced and the bandwidth is therefore mainly an effect of the homogeneous broadening and of the spectral congestion.

When the system is projected into a continuum of states, observables of the involved states are produced with indirect processes: the energy resolution in such experiments is therefore much worse. This is the case of ionization experiments like Electron/Ion Imaging or REMPI, when, holding the first laser in resonance with a given vibronic transition, the second photon is used to produce observables of the ionic states.

The energy resolution of ordinary laser spectroscopy experiments goes from a few wavenumbers for excited bound states to tens or even hundreds wavenumbers for ionic states. If in the first case the problem can be overcome by coupling for example with the HR-LIF [23–25] experiment whose resolution, thanks to stabilized CW laser sources, is lower than $0.1 cm^{-1}$, in the latter case the problem can be solved with techniques as Zero Electron Kinetic Energy (ZEKE) and Mass Analyzed Threshold Ionization (MATI). [26–29] The ionization of neutral near-threshold Rydberg states formed in the excitation process is revealed separately from spontaneous ionization, allowing for signal detection only when the system is prepared just below vibrational ionic levels that are optically active. Using these methods the resolution of ionic spectra increases up to $1 - 5 cm^{-1}$.

These techniques were successfully employed to describe structural and energetical properties of organic molecules and non-covalently bonded systems. Probably the most interesting results were obtained for hydrogen bonded clusters [30,31] and clusters formed by aromatic molecules (benzene, phenol, anisole,...) and rare gases (Ar, Kr,...), [32,33] small polyatomic molecules (N_2, water, NH_3,...), [34–36] or other polyatomic aromatic molecules (dimers,...) [8,37] Recently, R2PI was employed for the study of nucleobase couples [30,38] and

for the study of modeled drug-target interactions (Propofol-isopropanol cluster was characterized[39]).

Binding energies. Nevertheless, as we are studying bonds, we want to measure their effective strength, i.e. binding energy (BE), in a given quantum state. This parameter corresponds to the minimum amount of energy that has to be provided to the system to make it dissociate along the appropriate molecular coordinate. The direct measurement of the BE in the neutral ground state is not easy, as the produced fragment must be probed, and its contribution has to be separated from the total signal. Anyway, it is possible to determine quite accurately this energy using photoionization experiments.

Using energy resolved experiments, it is possible to determine ionic photodissociation energies and, knowing some very important energy parameters of the involved chemical species, to calculate data for neutral states.

The system can be pumped well above the ionization potential, up to a point where, after removing a low (almost zero) energy electron, enough vibrational energy is stored in the system and it can dissociate into a neutral and a charged fragment. Using mass spectrometers like TOF, the contribution of the ionic fragment can easily be separated from the total ion yield signal. The excess of energy initially stored in the system is distributed in both internal energy of the fragments and kinetic energy release (KER) of the particles. Assuming that it would be possible to produce a neutral and an ionic fragment in the ground state, and transform all the excess of energy in kinetic energy release of the particles, it is possible to determine the BE of any system in the ionic state and, knowing the IP of a single fragment, to determine by difference the BE in the neutral state. It's like filling the correlation diagram reported in fig. 1.2, where on the left side en-

ergetic levels of the fragment are reported and on the right side are the ones of the parent system with the dissociation threshold. At the dissociation threshold it is energetically equivalent for the system to exist as a cluster or as a separated pair of molecules, one in the neutral and one in the ionic ground state. Using an ionization experiment like the one described here, it is therefore possible to observe a detectable signal thank to the production of ionic fragments deriving from the photodissociation.

The experiments described above are extremely useful in the case of cluster photodissociations where internal and external vibrations are well separated so that the population of vibrational levels of the fragments is difficult. Some cases of covalent molecule photodissociations exist where the production of hot fragments was observed, e.g. the photodissociation of CH_3I.[40,41] In this case, the energy partitioning following the dissociation along the CH_3 + I reaction coordinate makes possible the population of both vibrational levels of the methyl (mostly ν_1, ν_2 and ν_4, that were observed while monitoring the iodine fragment distribution) and electronic levels of the iodine ($^2P_{(3/2)}$ and $^2P_{(1/2)}$, that were observed while monitoring the methyl fragment distribution).

More specifically what is determined in this kind of experiment is just the upper limit for the BE: the production of fragments starts only when population is promoted on the first excited ionic level that is optically accessible and energetically above the dissociation threshold, furthermore it has to be effectively connected to the dissociation coordinate.[42] The true value of the BE may be different from the observed one, but this difference is expected to be rather small because we assume that the correlation diagram in fig. 1.2 is respected, i.e. there is no energy loss due for example to the production of "hot" fragments. Indeed, for most of the cases studied up to now a very good agreement between experimentally observed values and

highest level quantum calculations has always been found.

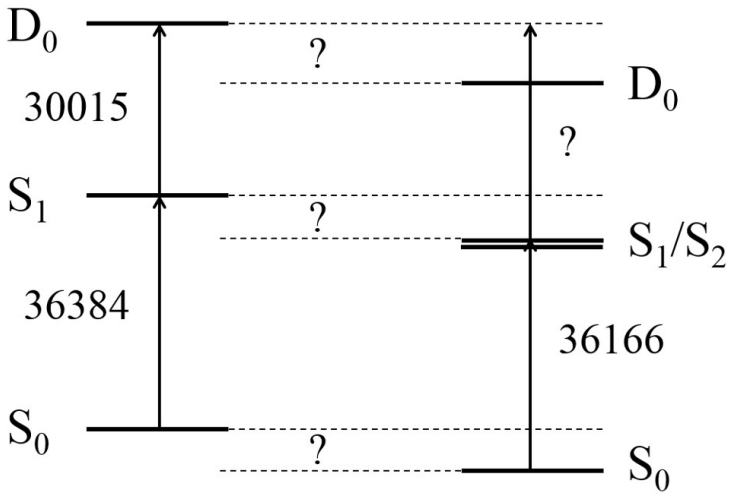

Figure 1.2: *Correlation diagram between electronic levels of a parent cluster (right) and of a daughter fragment (left) associated to the production of a ground state neutral fragment. If excitation through electronic levels of the parent occurs above the dissociation threschold, enough energy for the dissociation of an ionic fragment is stored in the system. This example shows the case of anisole dimer photodissociation: already known values are reported, measuring the missing value of the dissociation threshold (question mark on the right) allows for the determination of the binding energies (question marks in the center) in the neutral ground and excited states and in the ionic ground one.*

Photo-dissociations dynamics have been studied with multiphoton absorption spectroscopies. The simpler experiment that has been employed is the R2PI. The production of fragments in the mass spectrum is monitored while changing the total energy provided to the system. The recorded photo-fragmentation efficiency (PFE) curves show no production of fragments below the dissociation threshold and the signal increase once the

threshold is reached. The same information can be obtained in an Ion Imaging[43] experiment where, applying a mass gate to the detector, it is possible to reveal selectively the fragments.[44,45] In addition in the Ion Imaging it is possible to measure the maximum KER of the fragments. It is therefore also possible to compare two independent determinations of the BE, one deriving from the change with the excitation wavelength of the fragment ion signal, the other from determination of the maximum KER of the fragment upon dissociation. When the dissociation occurs at threshold, the maximum KER allowed for a fragment is zero. Unfortunately, we are now measuring properties of an ionic state. As already mentioned, the energy resolution of these techniques is quite limited and if a better resolution is needed, we draw again upon the MATI experiment. Monitoring both mass channels of parent and daughter ions it is indeed possible to see the cut off of the parent ionic spectrum coincide with the beginning of the daughter one. Excited neutrals at threshold for dissociation are field ionized with production of low energy electrons, that leave the system in an unstable highly excited state. These ions dissociate with high probability into smaller fragments and therefore leave no trace in the parent mass spectrum.

The Ion imaging technique was used to determine the binding energy of non-covalent complexes ($benzene{-}Ar_n$ $(n = 1, 2)$[46] and $p{-}difluorobenzene{-}Ar$[47]) by Lawrences group. MATI experiments were performed among others by Neusser group ($phenol - H_2O$, $1 - naphtol - H_2O$,...)[48] and Müller-Dethlefs group ($phenol - Ar_n$,[49] $phenol - CO$,[50] $phenol - N_2$,.[34]) in collaboration with Fujii and Dopfer groups.

From the computational point of view, different approaches for the evaluation of these quantities are available. In the neutral ground state the highest accuracy is reached with Coupled Clusters (CC) methods,[13,30] in-

cluding triple and eventually quadruple excitations. This method is unfortunately computationally expensive, so often cheaper methods like those based on DFT (Density Functional Theory) are performed using functionals like M06-2X, including parameters for the modeling of dispersion interactions.[8,12] Several non-covalent clusters have been studied up to now, most of them formed by an aromatic molecule and a rare gas or a small polyatomic molecule. The agreement between the finest experimental values for the BE and the most accurate calculations is in the order of $5 - 10\%$, but this comparison is still restricted for dispersion interaction: for example π-stacked clusters were missing, just as cluster formed by two aromatic molecules.

Ultrafast time resolution. A complementary view of dynamic molecular processes, like photodissociations, is provided by energy resolved experiments and time-resolved experiments.[51,52] To fully understand photodissociation dynamics, it is indeed necessary to understand the kinetics of the process.

The basic processes involved in a photodissociation are extremely fast. The temporal duration of an electronic transition itself for example falls in the range of attoseconds ($10^{-18} sec$). The lifetime of an electronic excited state, as to say the average survival time of an electronic excited state once it is prepared, can spread over many orders of magnitude in time. The electronic excited states of an ordinary aromatic molecule that can only relax with radiative processes can live as long as tens of nanoseconds ($10^{-8} sec$), while if non-radiative relaxation processes are possible, its lifetime can become as short as femtoseconds ($10^{-15} sec$). If somehow a triplet excited state is prepared, then the lifetime of such state is much longer and can even be in the order of hours ($10^{3} sec$), that is the case of phosphorescence.

Anyway, all the already mentioned processes involve electronic motions. In a dissociation process also nuclear motions are involved. Therefore, the minimal timescales for photodissociations are not related to the population of an excited electronic state, but to the time employed by the nuclei to move among the dissociation coordinate from the equilibrium position to a position where the distance between them is so high that they do not interact any more. The heavier the fragments, the longer the time that is necessary to reach this condition. It is important to note here that different dissociation processes can occur depending on the nature of the electronic state involved. If the potential energy surface (PES) for the reactive coordinate decays monotonically to a minimum at long internuclear distances, then the process is barrierless, and it leads to a short timescale for the photodissociation dynamics. If instead, in a dissociative PES, a stable relative minimum exists around an equilibrium position, then an energetic barrier to the dissociation is present. When an energy barrier is present, for the dissociation it is usually necessary to push the system over the barrier. In the case of production of very small molecular fragments, like hydrogen or methyl, tunneling through the barrier on the dissociation coordinate is sometimes possible. Therefore, the production of hydrogen radicals and methyl radicals occurs also when the system is pumped below the real dissociation threshold.[53–55] Anyway, at the edge for dissociation, the system can oscillate even millions of times before the effective dissociation. Therefore, the production of fragments happens on longer timescales with respect to barrierless cases.

Since the fastest photodissociations occur in timescales of femtoseconds, a probing system with a temporal resolution of at least the same order of magnitude is required. Ultrafast lasers with a time resolution of tens of femtoseconds per pulse are nowadays available for the study of such dy-

namics. Unfortunately, as the time resolution is that high, then the energy resolution is quite low. The bandwidth of femtosecond lasers is indeed limited by the uncertainty principle in the time and frequency formulation:

$$\Delta_t \Delta_\nu \geq \frac{1}{2} \tag{1.5}$$

An ultrafast $50fs$ pulsed laser with band center at $800nm(12500cm^{-1})$ has a broad bandwidth of about $500cm^{-1}$.

A very useful experiment to determine ultrafast dynamics in the gas phase is the Time-Resolved Ion/Electron Imaging.[56–58] In the Ion Imaging experiment, a two or three photon excitation scheme is employed. The first photon is used to pump the system to an excited dissociative state. Then, a different photon (or two different photons) is employed to ionize the neutral fragments produced and probe their formation as a function of the delay between the two processes. Images of the spatial distributions of the recoiling fragments at different delay times between the first and the second photon are recorded and the KER of fragments is recovered as a function of the time delay.

Among many different photodissociation dynamics that have been described with TR Ion Imaging (e.g. NH_3,CH_3I...)[57,59] we found very interesting the study of hydrogen and methyl radical tunneling dissociations from excited states of biologically relevant molecules (nucleobases, substituted phenols,...) that Stavros and his group were performing.[55,60] In adenine and phenol, for example, the dissociation into radicals was indeed evidenced well below the dissociation threshold, and the fragment release was associated to a certain maximum kinetic energy release coherent with a tunneling mechanism.

Up to now, TR Ion imaging has not been employed for the photodis-

sociation of molecular clusters. The reasons are related to the nature of the produced neutral fragments and to the typical lifetimes of these photodissociations that are much longer than in the case of single molecules. From the spectroscopical point of view the fragments arising from the dissociation of a molecular cluster are extremely similar to the parent species and to the monomers that are always present in a molecular beam. It is therefore evident that it is not straightforward to probe them selectively without the interference of the parent species and of the environment.

Aim and collaborations. This thesis is focused on the dissociation of organic aromatic molecules and their clusters induced by the absorption of UV light. Most of aromatic compounds show absorption bands in the UV region due to the presence of the aromatic electrons. In the case of jet cooled molecules, only the ground state is populated and the single vibronic transitions are observed in the electronic spectra.

Phenols and substituted phenols have been studied as prototype aromatic molecules. The O-H reaction coordinate was probed with a time-resolved Ion Imaging experiment in the laboratories of the Warwick University, thank to the collaboration with Dr. Stavros and his group. In particular, the existence of a dissociation reaction via hydrogen tunneling was observed in syringol but not in guaiacol. Whereas in phenol the tunneling mechanism was already known from a previous work,[55] in the case of guaiacol the hydrogen-bond between the hydroxil and the methoxy group is responsible for a total quenching of the $O-H$ reaction coordinate. In syringol a low efficiency dissociation mechanism is instead possible, but still not efficient as in phenol.

In phenols, the $O-H$ reaction coordinate is quenched also when the hydrogen is involved in an intermolecular bond with a different chemical

species. This is for example the case of water, that is bonded with an H-bond to the hydrogen of phenol when forming a bimolecular cluster. Moreover, the dissociation dynamics of such supramolecular structures, occurs probably in a longer timescale through a statistical process, so that it is not convenient to study it with a time-resolved experiment. The phenol-water complex dissociation via ionic PES was studied with the energy-resolved Ion Imaging experiment. This system was already described in literature through different approaches and was used as benchmark for the study of complexes with the apparatus.

The H-bonded phenol dimer was then the natural choice as a model system for the dissociation of aromatic dimers and its photodissociation was already known from the work of Dopfer *et al.*[37] that already studied it with a ZEKE experiment.

An aromatic dimer with a different intermolecular interaction was therefore studied. The anisole dimer was known to be the first observed aromatic dimer with pure π-stacking interaction and a center-symmetric structure, and the spectroscopic characterization was performed in the LENS laboratories in Florence. All the information about its ionic states were missing, so both the IP and the BE have been measured using first an Ion Imaging spectrometer and then a REMPI-TOF experiment where the sensitivity was enhanced at its maximum. To increase the accuracy of the results, the high resolution MATI-ZEKE synchronous experiment was performed in collaboration with the University of Manchester in the laboratories of Prof. Müller-Dethlefs.

Finally, the ZEKE-MATI experiment was performed on clusters formed by anisole and argon (anisole-Ar_n, n=1-3), where the main interactions are dispersive.

Bibliography

[1] S. Fanetti, A. Lapini, M. Pagliai, M. Citroni, M. Di Donato, S. Scandolo, R. Righini and R. Bini, *The Journal of Physical Chemistry Letters*, 2013, **5**, 235–240.

[2] A. K. Soper and M. A. Ricci, *Physical review letters*, 2000, **84**, 2881.

[3] V. Schettino, R. Bini, M. Ceppatelli, L. Ciabini and M. Citroni, *Advances in Chemical Physics*, 2005, **131**, 105.

[4] L. Ciabini, M. Santoro, F. A. Gorelli, R. Bini, V. Schettino and S. Raugei, *Nature materials*, 2006, **6**, 39–43.

[5] S. Buchsbaum, R. L. Mills and D. Schiferl, *The Journal of Physical Chemistry*, 1984, **88**, 2522–2525.

[6] F. A. Gorelli, L. Ulivi, M. Santoro and R. Bini, *Physical review letters*, 1999, **83**, 4093.

[7] U. Österberg and W. Margulis, *Optics letters*, 1986, **11**, 516–518.

[8] G. Pietraperzia, M. Pasquini, N. Schiccheri, G. Piani, M. Becucci, E. Castellucci, M. Biczysko, J. Bloino and V. Barone, *The Journal of Physical Chemistry A*, 2009, **113**, 14343–14351.

[9] P. Hobza, H. L. Selzle and E. W. Schlag, *The Journal of Physical Chemistry*, 1996, **100**, 18790–18794.

[10] E. Arunan and H. Gutowsky, *The Journal of chemical physics*, 1993, **98**, 4294–4296.

[11] H. Watanabe and S. Iwata, *The Journal of chemical physics*, 1996, **105**, 420–431.

[12] G. Pietraperzia, M. Pasquini, F. Mazzoni, G. Piani, M. Becucci, M. Biczysko, D. Michalski, J. Bloino and V. Barone, *The Journal of Physical Chemistry A*, 2011, **115**, 9603–9611.

[13] P. Hobza and K. Müller-Dethlefs, *Non–covalent interactions: theory and experiment*, Royal Society of Chemistry, 2010.

[14] K. Müller-Dethlefs and P. Hobza, *Chemical reviews*, 2000, **100**, 143–168.

[15] G. Scoles, *Atomic and molecular beam methods*, Oxford University Press, USA, 1992.

[16] H. Zuckermann, Y. Haas, M. Drabbels, J. Heinze, W. L. Meerts, J. Reuss and J. van Bladel, *Chemical physics*, 1992, **163**, 193–208.

[17] C. Eisenhardt, G. Pietraperzia and M. Becucci, *Physical Chemistry Chemical Physics*, 2001, **3**, 1407–1410.

[18] M. Becucci, G. Pietraperzia, M. Pasquini, G. Piani, A. Zoppi, R. Chelli, E. Castellucci and W. Demtroeder, *The Journal of chemical physics*, 2004, **120**, 5601–5607.

[19] J. M. Hollas, *Modern spectroscopy*, John Wiley & Sons, 2004.

[20] L. Zandee and R. Bernstein, *The Journal of Chemical Physics*, 1979, **70**, 2574–2575.

[21] P. Dao, S. Morgan and A. Castleman Jr, *Chemical physics letters*, 1985, **113**, 219–224.

[22] G. Piani, M. Pasquini, G. Pietraperzia, M. Becucci, A. Armentano and E. Castellucci, *Chemical physics letters*, 2007, **434**, 25–30.

[23] G. Meijer, G. Berden, W. L. Meerts, H. E. Hunziker, M. S. de Vries and H. R. Wendt, *Chemical physics*, 1992, **163**, 209–222.

[24] M. Becucci, G. Pietraperzia, N. Lakin, E. Castellucci and P. Bréchignac, *Chemical physics letters*, 1996, **260**, 87–94.

[25] C. Ratzer, J. Küpper, D. Spangenberg and M. Schmitt, *Chemical Physics*, 2002, **283**, 153–169.

[26] E. W. Schlag, *ZEKE spectroscopy*, Cambridge University Press, 1998.

[27] K. Muller-Dethlefs and E. W. Schlag, *Annual Review of Physical Chemistry*, 1991, **42**, 109–136.

[28] L. Zhu and P. Johnson, *The Journal of chemical physics*, 1991, **94**, 5769–5771.

[29] C. Jouvet, C. Dedonder-Lardeux, S. Martrenchard-Barra and D. Solgadi, *Chemical physics letters*, 1992, **198**, 419–423.

[30] M. S. de Vries and P. Hobza, *Annu. Rev. Phys. Chem.*, 2007, **58**, 585–612.

[31] P. Hobza and J. Šponer, *Chemical reviews*, 1999, **99**, 3247–3276.

[32] I. Kalkman, C. Brand, T.-B. C. Vu, W. L. Meerts, Y. N. Svartsov, O. Dopfer, X. Tong, K. Müller-Dethlefs, S. Grimme and M. Schmitt, *The Journal of chemical physics*, 2009, **130**, 224303.

[33] S. Ullrich, G. Tarczay and K. Müller-Dethlefs, *The Journal of Physical Chemistry A*, 2002, **106**, 1496–1503.

[34] S. Haines, W. Geppert, D. Chapman, M. Watkins, C. Dessent, M. Cockett and K. Müller-Dethlefs, *The Journal of chemical physics*, 1998, **109**, 9244–9251.

[35] T. S. Zwier, *Annual review of physical chemistry*, 1996, **47**, 205–241.

[36] H.-T. Kim, R. J. Green, J. Qian and S. L. Anderson, *The Journal of Chemical Physics*, 2000, **112**, 5717–5721.

[37] O. Dopfer, G. Lembach, T. G. Wright and K. Müller-Dethlefs, *The Journal of chemical physics*, 1993, **98**, 1933–1943.

[38] J. G. Hill and A. Das, *Physical Chemistry Chemical Physics*, 2014, **16**, 11754–11762.

[39] I. León, I. Usabiaga, J. Millán, E. J. Cocinero, A. Lesarri and J. A. Fernández, *Physical Chemistry Chemical Physics*, 2014, **16**, 16968–16975.

[40] A. T. Eppink and D. Parker, *The Journal of chemical physics*, 1999, **110**, 832–844.

[41] A. Eppink and D. H. Parker, *The Journal of chemical physics*, 1998, **109**, 4758.

[42] F. Mazzoni, M. Pasquini, G. Pietraperzia and M. Becucci, *Physical Chemistry Chemical Physics*, 2013, **15**, 11268–11274.

[43] B. J. Whitaker, *Imaging in molecular dynamics*, Cambridge University Press, 2003, vol. 1.

[44] A. J. Heck and D. W. Chandler, *Annual review of physical chemistry*, 1995, **46**, 335–372.

[45] G. Piani, L. Rubio-Lago, M. A. Collier, T. N. Kitsopoulos and M. Becucci, *The Journal of Physical Chemistry A*, 2009, **113**, 14554–14558.

[46] J. R. Gascooke and W. D. Lawrance, *The Journal of Physical Chemistry A*, 2000, **104**, 10328–10335.

[47] S. M. Bellm, J. R. Gascooke and W. D. Lawrance, *Chemical Physics Letters*, 2000, **330**, 103–109.

[48] J. Braun, T. Mehnert and H. Neusser, *International Journal of Mass Spectrometry*, 2000, **203**, 1–18.

[49] C. E. Dessent, S. R. Haines and K. Müller-Dethlefs, *Chemical Physics Letters*, 1999, **315**, 103–108.

[50] S. R. Haines, C. E. Dessent and K. Müller-Dethlefs, *The Journal of chemical physics*, 1999, **111**, 1947–1954.

[51] A. H. Zewail, *Angewandte Chemie International Edition*, 2000, **39**, 2586–2631.

[52] L. R. Khundkar and A. H. Zewail, *Annual Review of Physical Chemistry*, 1990, **41**, 15–60.

[53] A. Sobolewski, W. Domcke, C. Dedonder-Lardeux and C. Jouvet, *Physical Chemistry Chemical Physics*, 2002, **4**, 1093–1100.

[54] G. Pino, A. Oldani, E. Marceca, M. Fujii, S.-I. Ishiuchi, M. Miyazaki, M. Broquier, C. Dedonder and C. Jouvet, *The Journal of chemical physics*, 2010, **133**, 124313.

[55] G. M. Roberts, A. S. Chatterley, J. D. Young and V. G. Stavros, *The Journal of Physical Chemistry Letters*, 2012, **3**, 348–352.

[56] A. Stolow and J. G. Underwood, *Advances in chemical physics*, 2008, **139**, 497.

[57] K. L. Wells, G. Perriam and V. G. Stavros, *The Journal of chemical physics*, 2009, **130**, 074308.

[58] T. Suzuki, *Annu. Rev. Phys. Chem.*, 2006, **57**, 555–592.

[59] R. De Nalda, J. Izquierdo, J. Durá and L. Bañares, *The Journal of chemical physics*, 2007, **126**, 021101.

[60] M. Staniforth and V. G. Stavros, *Proceedings of the Royal Society A: Mathematical, Physical and Engineering Science*, 2013, **469**, 20130458.

Chapter 2

Experimental techniques

Schematically, the experiments that we performed consist of three different parts. First, the sample preparation in a supersonic molecular beam. Second, the excitation of the sample with pulsed lasers allowing for electronic ionization spectroscopy. Finally, the charged particle detection, signal collection and software elaboration.

Supersonic Molecular Beams. A supersonic molecular beam[1] is produced by an adiabatic expansion of a gas mixture from a source, a pulsed valve, where the pressure is high, to a region, expansion chamber, where the gas pressure is several orders of magnitude lower. The gas mixture is formed by a carrier gas and the molecules of interest. As carrier gas, noble gases like He, Ne and Ar are used because of their extremely low reactivity and their low atomic weight. These gases flow into the sample holder and trail molecules of the sample in the pulsed valve, where the pressure is in the order of $10^3 mbar$. When the valve is opened the gas mixture flows through a $200 - 500 \mu m$ nozzle and then expands into a chamber where the pres-

sure is about $10^{-6} mbar$. During the first stages of the expansion process, numerous collisions are taking place. The collisions equalize the speed of carrier gas and molecules, quenching the excited internal states and making possible the cluster formation. The ratio (P_i/P_f) between the initial and final pressures defines the expansion speed of the gas mixture: the higher the ratio, the faster the expansion. If the ratio is high enough, then it allows for molecules moving faster than sound in the expansion, meaning that molecules that start their flight first can not be reached by molecules that start their flight later: the beam is therefore almost collision-free in the propagation direction and molecules in the beam are not exchanging energy. If there is no energy exchange, once a molecule or a molecular aggregate is prepared in a certain quantum state, then it stays in that quantum state as long as an external perturbation occurs. Moreover, as the gas expands, molecules are freezing. Now, despite a non-equilibrium system like this can not be described classically in terms of temperature, it is possible to define translational temperatures that are extremely low in the directions perpendicular to the molecular beam direction. These temperatures can reach less then $10K$, so that the beam results highly collimated in the propagation direction.

Once the gas mixture is reaching stationary conditions, the central part of the expansion is selected by a skimmer placed $10 - 50mm$ from the nozzle. The alignment of the nozzle in front of the skimmer is crucial for the selection of the central part of the beam. This part corresponds indeed to the coldest one, where clusters concentration is higher.

When the gas mixture passes through the nozzle, thousands of collisions between molecules and carrier gas atoms take place and a relatively elevate quantity of supramolecular aggregates is formed. The final concentration of bimolecular clusters in the beam, for example, is usually 10^{-3}

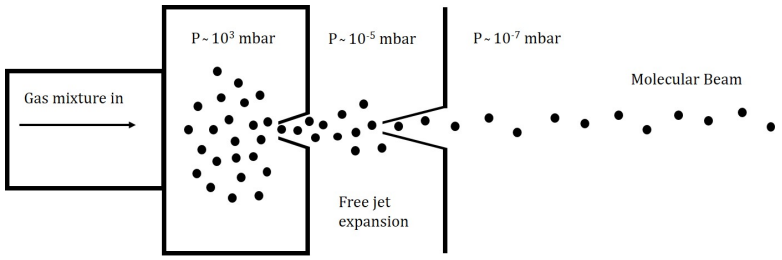

Figure 2.1: *Schematic representation of a molecular beam*

times the monomer concentrations, allowing for detection of signal after the laser excitation. Fig. 2.1 reports a schematic view of the molecular beam production.

The excitation is produced with laser beams traveling perpendicularly to the molecular beam, in order to minimize the Doppler effect. Indeed, if the molecular beam can be represented by a single velocity vector $\vec{v}$, the Doppler broadening of a REMPI peak for example results:

$$\Delta\nu = \nu\frac{\vec{v}}{c}\sin\alpha \tag{2.1}$$

where α measures the difference from the orthogonality condition between the molecular and the laser beam. If α, half of the residual divergence of the molecular beam, is 1° and ν is $36000cm^{-1}$, the Doppler broadening is lower than $0.002cm^{-1}$.

For this thesis, we have used a General Valve Series 9 pulsed valve (fig. 2.2) for energy-resolved experiments and an Even-Lavie pulsed valve (fig. 2.3) for the time-resolved experiment.

Electronic spectroscopy. Photoionization spectroscopy [2] implies the transition between different electronic states. Electronic transitions from an

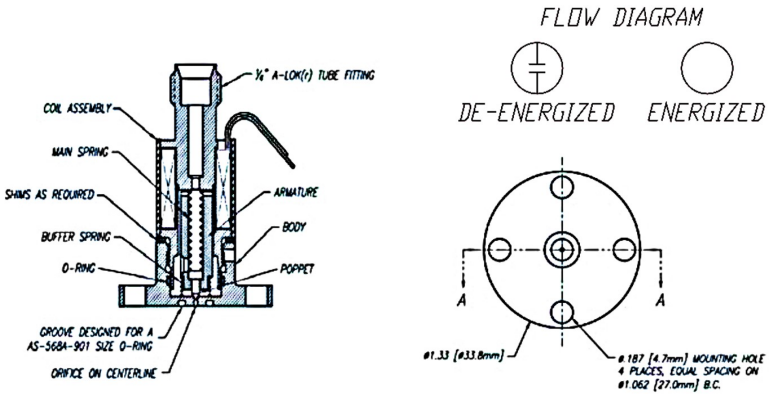

Figure 2.2: *Schematic representation of a General Valve Series 9 valve*

initial $|\psi''\rangle$ state to a final $|\psi'\rangle$ state are produced by the interaction of matter with ultraviolet or visible light.

Following the Born-Oppenheimer approximation it is possible to separate nuclear (ψ_n) and electronic (ψ_e) contributions to ψ. The nuclear contribution is then described by translational (T_n), rotational (ϕ_l), vibrational (θ_v) and nuclear spin (I_i) terms, while the electronic contribution is described by orbitalic (φ_e) and electronic spin (S_s) terms. In the approximation of total independence of these components, ψ can be written as:

$$\psi = T_n \phi_l \theta_v I_i \varphi_e S_s \tag{2.2}$$

but, since spin components don't interact with electric fields and translational components only originate a continuum of levels, they can be neglected. Then, as a further approximation, nuclear motions like vibrations and rotations happen on much longer timescales with respect to electronic transitions, so if the exciting frequencies of light are in the UV or visible part of the spectrum, the only term that has to be considered for the

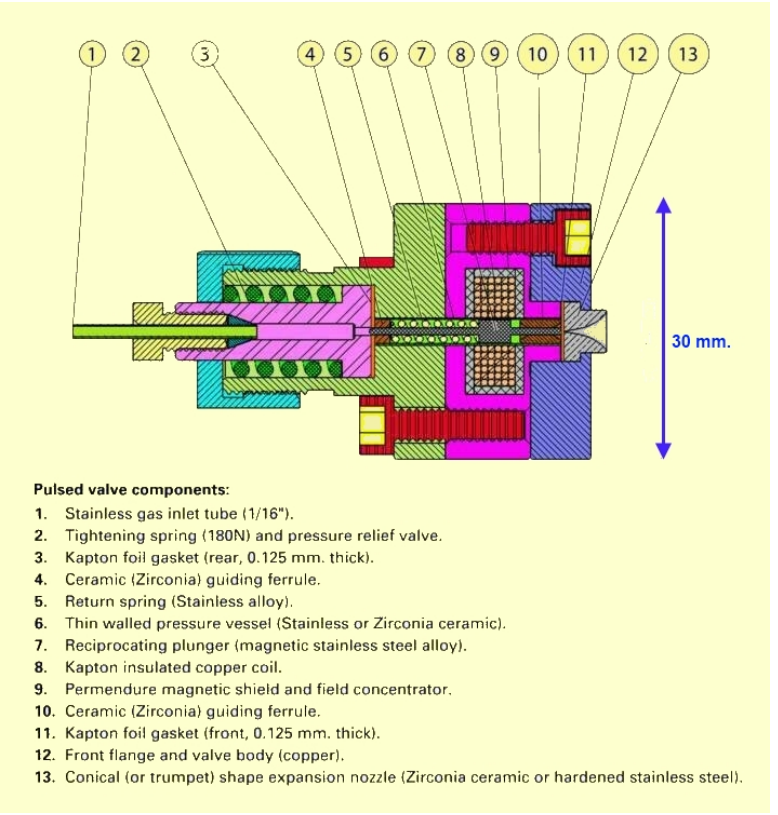

Figure 2.3: *Schematic representation of an Even Lavie valve*

interaction light-matter is the electronic orbitalic term.

An electronic transition is the result of the perturbation of the molecular system, due to the coupling of its dipole-moment with the external oscillating electric field. It can be described by an operator H' that is the scalar product between the electric field E and the electric dipole moment μ

$$H' = \mu E \tag{2.3}$$

acting on electronic states. The efficiency of the perturbation is measured by the transition probability

$$P \propto |\langle \psi' | H' | \psi \text{“} \rangle|^2 \tag{2.4}$$

that can be easily written as

$$P \propto |\langle \psi' | \mu | \psi \text{“} \rangle|^2 \tag{2.5}$$

since the electric field E does not operate on wavefunctions. Considering that the Born-Oppenheimer approximation is valid also for the electric dipole moment μ, we can write:

$$\mu = \mu_n + \mu_e \tag{2.6}$$

as the sum of the nuclear electric dipole moment and the electronic electric dipole moment. Anyway, as already discussed above, the electronic orbitalic part of the wavefunction is in first approximation the only term that have to be considered in the case of electronic spectroscopy, so we can neglect

the nuclear component and focus only on the electronic one, that is:

$$\mu_e = -e \sum_i r_i \tag{2.7}$$

where e is the electron charge and r_i is the position vector for the i-th electron. The transition probability can therefore be written as:

$$P \propto |R_e|^2 \tag{2.8}$$

with

$$R_e = -e \sum_i \langle \varphi'_e | r_i | \varphi“_e \rangle \tag{2.9}$$

that, since the transition probability has to be $R_e \neq 0$, leads to:

$$\Gamma(\varphi'_e) \times \Gamma(r_i) \times \Gamma(\varphi''_e) \supset A \tag{2.10}$$

which means that the condition is achieved only if the direct product between the single irreducible symmetry representations (Γ) of the different terms contains the irreducible totalsymmetric representation (A).

Two things are immediately evident: first of all the initial state $|\varphi“_e\rangle$ is typically the ground state and therefore its irreducible representation is totalsymmetric, secondly r_i are vectors that can be expressed in cartesian coordinates, so they transforms as translations along the three axes with representations (T_x, T_y, T_z). The arising selection rules are:

$$\Gamma(\varphi'_e) = \Gamma(T_x) \text{ or } \Gamma(\varphi'_e) = \Gamma(T_y) \text{ or } \Gamma(\varphi'_e) = \Gamma(T_z) \tag{2.11}$$

i.e. the electronic function of the excited state must have the same irre-

ducible representations of the electric dipole moment and therefore:

$$\Delta l = \pm 1 \tag{2.12}$$

To obtain this important result, very strong approximation was made neglecting all the other components of the wavefunction. The first term to consider out of this approximation is the vibrational term:

$$\psi = \varphi_e \theta_v \tag{2.13}$$

so that eq. 2.9 becomes:

$$R_{ev} = -e \sum_i \langle \varphi'_e | r_i | \varphi \text{“}_e \rangle \langle \theta'_v | \theta''_v \rangle \tag{2.14}$$

or

$$R_{ev} = R_e S_v \tag{2.15}$$

where S_v is the superposition integral between the vibrational functions of the excited and the ground state. This term is the Frank-Condon factor, i.e. the transition probability is higher as vibrations have similar character and as geometries of excited and ground state are similar.

The contribution of spin functions to the transition probability is

$$P \propto \langle I'_i | I \text{“}_i \rangle \langle S'_s | S \text{“}_s \rangle \tag{2.16}$$

that gives the selection rules:

$$\Delta I = 0 \ ; \ \Delta S = 0 \tag{2.17}$$

Finally we have to consider the contribution of rotational functions. These

functions interact with the dipolar moment and their contribution in terms of selection rules is the same of pure rotational spectroscopy:

$$\Delta J = 0, \pm 1 \; ; \; \Delta K = 0, \pm 1 \tag{2.18}$$

for a symmetric rotor (J is the quantum number for the total angular momentum and K is its projection on the principal rotation axis) and

$$\Delta K_{+1} = 0, \pm 1, \pm 3, ... \iff \Delta K_{-1} = 0, \pm 2, \pm 4, ... \tag{2.19}$$

or

$$\Delta K_{-1} = 0, \pm 1, \pm 3, ... \iff \Delta K_{+1} = 0, \pm 2, \pm 4, ... \tag{2.20}$$

or

$$\Delta K_{+1} = 0, \pm 1, \pm 3, ... \iff \Delta K_{-1} = 0, \pm 1, \pm 3, ... \tag{2.21}$$

for non-symmetric rotors, with K_{+1} and K_{-1} being pseudo-quantum numbers obtained from the expansion in a complete *eigenfunctions* set of the asymmetric rotor equations and they correspond to the limit of the approximations of the rotor as prolate and oblate ellipsoid.

Anyway, as the techniques that we have used they are all based on two photon absorption, the selection rules in eq. 2.12 become:

$$\Delta l = 0, \pm 2 \tag{2.22}$$

while all other restrictions, except the ones on magnetic moments I and S, almost fall and vibronic transitions are possible to every final state.

Pulsed lasers To observe multiphoton absorption, a high power laser source is required.[3] Common continuous wave (CW) lasers are usually not

able to produce high enough power outputs to induce multiphoton absorption processes. Pulsed lasers indeed produce high energy in a very small time interval, so that for example the output power of a nanosecond pulsed laser can be 9 orders of magnitude higher than that of a CW laser.

Nanosecond pulsed lasers that we have used in Florence and Manchester are frequency doubled tunable dye lasers pumped by the second ($532nm$) and third ($355nm$) harmonic emission of a Q-switched solid state (Nd:YAG) pulsed laser. The gain factor (Q) of a laser cavity is defined as 2π times the ratio between the energy (E_c) in the cavity and the energy loss (dE_t/dt) times the oscillation period ($\frac{1}{\nu}$):

$$Q = \frac{2\pi\nu E_c}{dE_t/dt} \tag{2.23}$$

This Q factor can be changed very quickly in order to maximize the laser peak power. In our case, the active Q-switching is obtained with a Pockels cell in the oscillator cavity of the Nd:YAG laser. A Pockels cell is an electro-optic material that changes its refractive index when a certain voltage is applied. When no voltage is applied to the cell, the Q-factor of the laser is extremely small: the active medium is pumped by a flash light and the maximum population inversion is obtained. Once the maximum of the inversion is obtained a voltage is applied to the cell and the Q factor becomes immediately high: the optical amplification is allowed, the stimulated emission process takes place and high power laser light leaves the cavity. This emission process is very quick and in about $5ns$ the system goes back to the initial conditions and the voltage applied to the cell is turned off again.

However, ultrafast dynamics require much shorter pulses that cannot be produced with Q-switched lasers. Pulses in the order of femtoseconds are produced with mode-locked lasers.

Dye lasers and solid state lasers permit the oscillation in the cavity of multiple modes with random phases. These modes in the time domain generate interference that can be destructive or constructive. Placing into the laser cavity a fast enough shutter it is possible to allow for light transmission in a time interval comparable with the constructive interference peak profile. It is therefore possible to let this interference pulse pass and cut all other noise. The amplification of laser light is therefore due to this photon packet that is very broad in the energy domain, but extremely narrow in the time domain, traveling back and forth in the cavity. To do this, the shutter must be tuned to a frequency

$$\omega = \frac{c}{2L} \tag{2.24}$$

where L is the cavity length and c is the speed of light: this frequency correspond to the oscillation of the interference peak making one trip in the cavity.

A quite common way to produce active mode-locked lasers is to use as shutter in the cavity an Acusto-Optic Modulator (AOM). A drive signal is used as clock for the AOM. The regenerative mode-locking is obtained when the drive signal is derived directly from the laser cavity. This means that if the cavity length changes slightly, the drive signal to the modulator changes accordingly.

Charged particles detection If the system absorbs two ultraviolet photons, an electron can be promoted up above the ionization threshold. Once the ionization occurs, at least two charged particles are produced and can be detected.

Charged particles can be separated thanks to their charge to mass ratio

in a mass spectrometer. In all our experiments Wiley Mc-Laren[4] Time-Of-Flight (TOF) mass spectrometers were employed. When the integral signal produced by particles hitting the detector was detected as in the case of REMPI spectroscopy, a Reflectron TOF spectrometer (RETOF) was used in order to improve the mass resolution ($1uma$ over $1000uma$). In the case of Ion and Electron Imaging experiments instead, the interest is in the kinetic energy release of ionic particles, so a position sensitive detector is coupled with a TOF in linear configuration.

A RETOF is schematically presented in fig. 2.5. The excitation region is between the two armours of a capacitor: a high positive voltage is applied to the back plate and a positive lower voltage is applied to the front plate. The potential difference generates a field that pushes ions through a grounded grid in the field free TOF tube. In this region a first set of electrostatic optics compensates the dispersion of the particles and focuses the ion beam. At the end of the tube the reflectron apparatus (a series of parallel plates, where the applied voltages at each plate are partitioned from the high voltage applied to the back plate, to the lower voltage applied to the front plate) makes the ion beam curve and directs it back to the micro channel plate (MCP) detector. The MCP delivers a current that is proportional to the number of ions hitting the detector in a given time interval.

A linear TOF like the ones that we have used for Ion Imaging experiments is schematically presented in fig. 2.4. The electrostatic lens is formed by three electrodes (Repeller-Extractor-Ground). The higher voltage is applied to the repeller, the third electrode is grounded. As the ionization region is between the first two electrodes, the voltage of the second electrode is tuned to a suitable potential in order to reach a good Velocity Mapping condition.

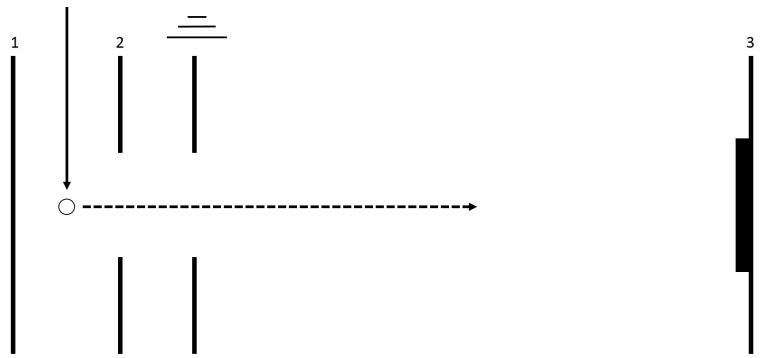

Figure 2.4: *Schematic representation of a linear TOF with the capacitor (1 and 2) on the left, the grounded electrode that separates the field free region and, on the right, the detector (3). With the filled arrow the laser path is shown, with the dashed arrow the ionic path is shown.*

2.1 REMPI-TOF

An overview on the REMPI spectroscopy was already given in the introduction, together with the description of the multiphotonic absorption. From now on, as we consider just the 2-photons excitation scheme, we will talk of R2PI (Resonant 2-Photon Ionaization): the first photon exciting the system from the ground state to an excited one is called *pump* and the second one bringing the system above the dissociation threshold is called *probe*. We usually perform pump and probe experiments in order to control the total energy provided to the system.

R2PI spectroscopy in our studies was coupled with a Wiley McLaren TOF spectrometer in reflectron configuration (RETOF), in order to enhance the mass resolution of the instrument with respect to a linear TOF spectrometer.

Usually, a preliminary analysis consists of shining a laser with very high

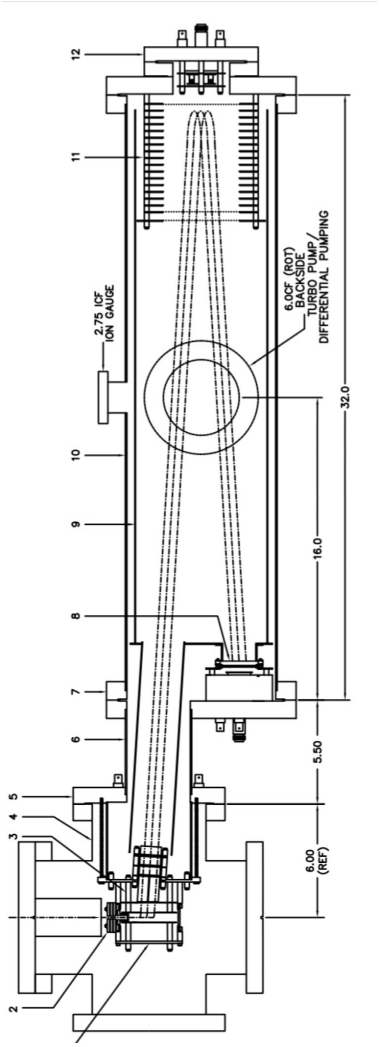

Figure 2.5: *Schematic representation from the manual of a Jordan AREF D-850 TOF*[5] *spectrometer in reflectron configuration. On the left part of this picture the excitation region (marked with 3) is reported, then ions fly following the dashed trajectories and are reflected by the reflectron on the right (marked with 11). Ions finally hit the detector (marked with 8).*

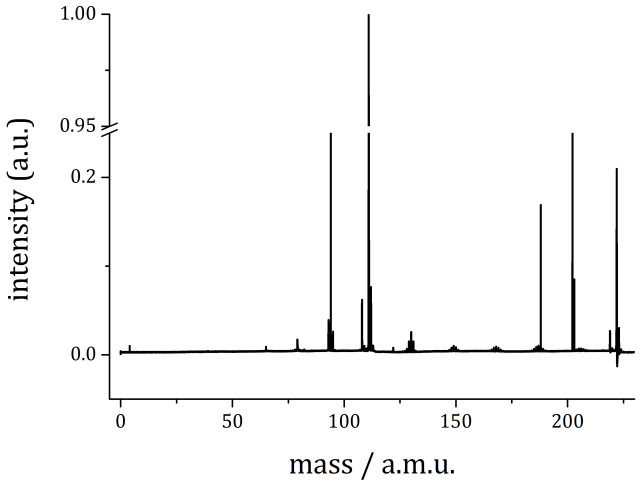

Figure 2.6: *Example of TOF Mass spectrum*

power on the molecular beam. In such way every present chemical species is ionized through non-resonant multiphoton absorption processes. As a result many peaks in the mass spectrum are observed (fig. 2.6). Once the mass of the different peaks reported in the spectrum is assigned, it is possible to focus on the peak, or the peaks, of interest.

In a R2PI experiment usually the wavelength of the probe laser is held to a constant value and the wavelength of the pump laser is changed, while monitoring the PhotoIonization Efficiency (PIE) for a single mass peak. When the resonance with an optically active transition is reached by the pump laser, an increase in the signal rate is observed. The vibronic bands observed in the spectrum have to be related with the population of electronically excited states with the pump laser and then to their ionization through the absorption of the second. In the spectrum we obtain therefore

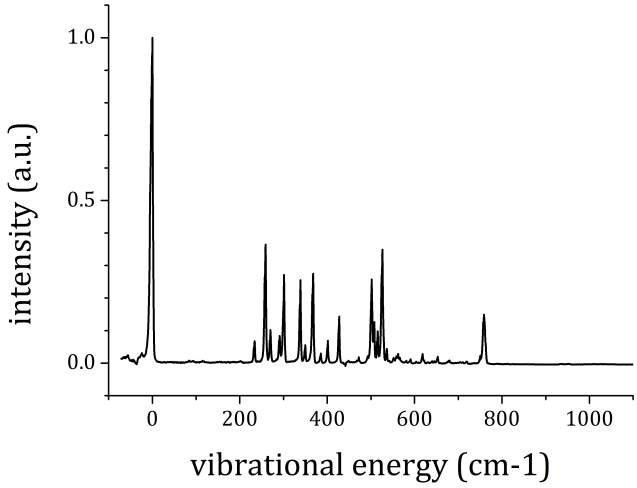

Figure 2.7: *R2PI electronic spectrum of anisole, the excitation energy is scaled on the origin transition.*

the vibrational structure of the electronically excited states.

In the spectrum of the $S_1 \leftarrow S_0$ electronic transition of a single aromatic molecule, if the transition is allowed, the lowest energy band of the spectrum, usually the most intense, is assigned as the origin (0_0^0) of the vibronic spectrum, as the geometry of ground and excited states are similar. However, if the equilibrium geometries are different and the FC factors low for the transition to the first excited state, it is also possible that the first peak is not the strongest one. Fig. 2.7 reports an example of an electronic spectrum obtained with R2PI.

Holding the pump laser in resonance with a given vibronic transition and changing the wavelength of the probe laser it is possible to monitor the ionic states. Below the ionization threshold there is no production of

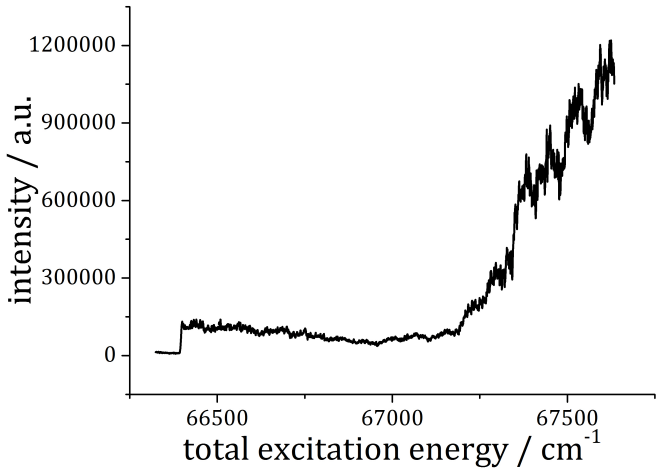

Figure 2.8: *PIE curve of anisole, it is evident the first step corresponding to the ionization threshold at* $66400cm^{-1}$*. Then, many steps corresponding to different ionic vibrational levels are observed above* $67200cm^{-1}$*.*

ions, once the threshold is reached the PIE rises immediately. When the excitation energy is higher than the threshold, the excess of internal energy in the excited system is converted in kinetic energy of the electron, so the PIE curve always grows from lower to higher excitation energies above the ionization threshold. Usually, when the probe laser finds a resonance with a vibronic transition of the ion, then the PIE curve rises more quickly. Fig 2.8 reports an example of a PIE curve where many steps are present, corresponding to different vibrational levels of the ion.

As already discussed above, this technique is more accurate for the study of excited states than ionic states. Anyway, extremely useful information can be obtained also for ionic states: for example the ionization potential

(IP) and the binding energy (BE).[6–8] Indeed, holding the first laser in resonance with a vibronic transition of the parent ion and monitoring the mass channels of both parent and daughter ion while changing the energy of the probe photon, it is possible to observe the rise in the PFE of the daughter one once the dissociation threshold is reached.

2.2 MATI-ZEKE

A high resolution method for the study of ionic states consists of the detection of threshold ions and electrons apart from other charged particles produced in the excitation process through a R2PI scheme.[9,10] The excitation ($h\nu$) of a neutral particle above its ionization threshold implies the formation of an ion with an internal energy E_{int} corresponding to an energetically accessible vibrational state and of an electron with a kinetic energy (KE) equal to the excess of energy, with respect to the vibration, brought to the system by the excitation process.

$$KE = h\nu - E_{int} \tag{2.25}$$

This ionization process takes place immediately. If instead the excitation energy takes the system almost at threshold to a vibronic level of the ion, then the electron can stand on a state that is still neutral called Rydberg state,[11] for a certain time before leaving the system.

Rydberg states are long living neutral excited states corresponding to electronic excitation of the system at high values ($n > 200$) of the principal quantum numbers. The Rydberg series for high values of the quantum numbers converge to the ionic thresholds: the higher the quantum number,

the closest the energy of the excited level to the ionic threshold. Moreover, also the difference between following Rydberg states decreases as the values of the quantum numbers increases. These states correspond to electrons promoted on the more diffused electronic functions but still bonded to the ionic core. The radius of these functions tend to infinite: the core of the molecule is seen as an hydrogenic system by the electron so far on the orbit, being the interaction core-electron almost purely coulombic. With respect to a real hydrogenic system where the energy E_n of Rydberg series can be written as:

$$E_n \propto -\frac{Ry}{n^2} \tag{2.26}$$

where Ry is the Rydberg constant ($13.6eV$) and n is the principal quantum number, in a non-hydrogenic system the perturbation of core electrons cannot be neglected and is accounted as the quantum defect δ_l with l quantum number for the orbital angular momentum:

$$E_{n,l} \propto -\frac{Ry}{(n-\delta_l)^2} \tag{2.27}$$

As the difference in energy between the highest Rydberg levels and the ionic threshold is negligible, a very small perturbation can promote electrons above the threshold and ionize the system producing an ion with high internal energy and an electron with almost zero kinetic energy. The small perturbation can be provided by a low voltage electric pulse. First of all the field removes the degeneracy between levels and allows for m (magnetic quantum number) and l mixing, then induces a change in the Coulomb potential curve as shown in fig. 2.9. The field effect can be seen as a lowering of the ionization threshold: some Rydberg states (red Stark states) are immediately ionized and the others (blue Stark states) that need a

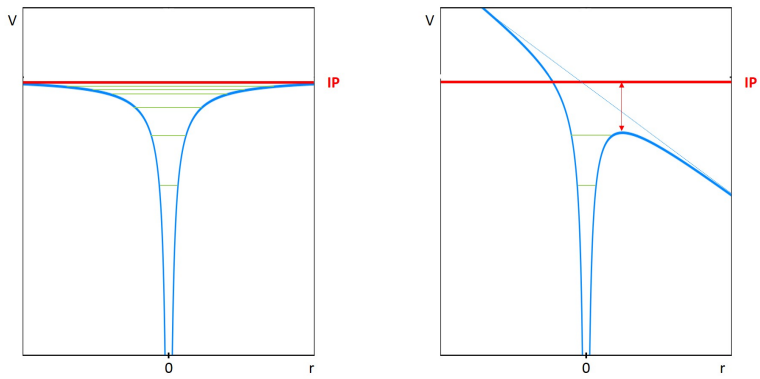

Figure 2.9: *Field effect on Rydberg series before perturbation (left) and after the perturbation (right), potentials represent pure Coulomb interactions. This simplified representation neglects Stark effects. After the perturbation it is evident the presence of a saddle point, that lowers the observed IP of a quantity ΔV corresponding to the red arrow. The production in the ionic or electronic mass channel of signal with the same energy width is observed.*

stronger field to ionize are still populated after the perturbation. Fig. 2.9 illustrates Rydberg states before the field perturbation (left) and after the field perturbation (right) with respect to the ionic threshold, Stark effect is neglected for simplification. It is evident on the right side the presence of a saddle point that lowers the limit of the ionization continuum below the real ionic potential.

From the experimental point of view,[12,13] the system is prepared in a molecular beam that is perpendicularly crossed by the laser beam. The laser-molecule interaction region is between the two armours of a capacitor. When the excitation occurs no potential is applied. Let's assume that the pump laser is in resonance with the origin transition of the electronic spectrum of a given species and that the probe laser takes the system just below the ionization threshold. No direct ionization is possible due to two-

photon process and long living Rydberg states are populated. Anyway, a very small amount of directly ionized particles will be produced thanks to higher order multiphoton absorption processes. After the laser excitation a low voltage (about $1V$) is applied to one of the plates of the capacitor: free electrons are accelerated in the direction of the capacitor and will collide to the charged plate, positively charged particles are deflected in the opposite direction. At the same time, some Rydbergs (the closest to the ionization threshold) are ionized and behave as directly ionized ones. Rydbergs that are still neutral are not deflected by the applied voltage and continue flying in the beam direction. The low voltage stays on to separate neutrals and charged particles. Finally a high voltage ($10^2 - 10^3 V$) pulse field ionizes neutral particles and push them and the other directly ionized particles into the mass spectrometer. When the HV pulse is turned on, the two groups of different particles are in the same position with respect to the direction of propagation of the beam, but the Rydbergs being still in the axis of propagation and the direct ions slightly displaced. Therefore, the two groups of particles last in the capacitor for different times and takes slightly different accelerations. As a result they hit the detector at slightly different times.

Changing the probe energy above the ionization threshold means producing just direct ions: no Rydbergs are formed. In the mass channel of the direct ionization the PIE increases. In the Rydbergs mass channel, when a resonance is found, a transition corresponding to the first optically accessible ionic state is observed then the signal goes down.

Anyway, the information of the higher Rydbergs get lost with this simple setup. To recover this information, at some point after the excitation the low voltage is reversed and for a very small time interval (about $300ps$) a voltage of about $-2V$ is applied to the same plate. The reversed field

reverses blue populated and red ionized Stark states, mixing again their population. Again the effect of the field is to take some red states over the ionization threshold and push some blue ones down. Usually, after the small time interval the voltage is set to positive again and the new group of charged particles, formed by Rydbergs that were in the beam axis, start moving in the same direction of previously ionized ones. The signature of these states is the so called High Resolution MATI as it comes from higher Rydbergs.

Electrons produced by the field reversion can be collected and their signature (totally identical to HR-MATI) recorded. This experiment is named ZEKE. A synchronous detection scheme for ZEKE and MATI was presented by Dessent *et al.*[14] An alternative method was developed during the work for this thesis and will be presented later on.

This powerful technique was employed for the study of photodissociations as, once the dissociation threshold is reached in the ionic states, the MATI signature disappears from the parent MATI mass channel and appears in the daughter one. The uncertainty for a dissociation threshold determined with this experiment is related mostly to the uncertainty in the determination of the exciting frequency.

2.3 Ion/Electron Imaging

With the R2PI absorption scheme, the molecular system is ionized and two charged particles are produced: an ion with internal energy E_I and an electron with kinetic energy EKE. The energy balance of the ionization process can be written as:

$$h\nu_1 + h\nu_2 = E_I + \mathrm{EKE} \tag{2.28}$$

where on the left the energy provided to the system by the two photons is reported. Anyway, since the internal energy of the ion is quantized, only discrete KER values are possible for electrons. In the ionization region several molecules are present, detached electrons start expanding on a spherical distribution thanks to their velocity vector. If the energy excess with respect to the IP is enough, more than one ionic vibrational level can be populated, so more than one discrete value of KER is possible and electrons expand on concentric spheres. As in previous experiment, the ionization region is located between the plates of a capacitor and charged particles are accelerated in the field free region of the TOF thank to voltages applied to the electrodes. During the flight in the field free region (about $10\mu s$) the electron spheres can expand for a long enough time. At the end of the TOF tube a position sensitive detector records a bidimensional image of the 3D spherical distributions. The detector consists of an MCP coupled with a phosphor screen. Charged particles with high kinetic energy hit the front of the MCP producing electrons. These electrons are accelerated, thanks to the applied high voltage, into the closest channel where they are multiplied. A bunch of electrons comes out from the back of the MCP and is transformed into light by the phosphor screen. The channel of the phosphor screen that produces light corresponds to the portion of the detector hit by the charged particle. The light is then captured by a video camera. The radius of each circle obtained in the 2D image is proportional to the speed of the fragment.

In order to focus the image on the phosphor screen, a setup called Velocity Map Imaging was developed.[15] This setup (left of fig. 2.10) consists of using a three plates electrostatic lens: the back plate is called Repeller and provides the higher voltage, the second electrode is called Extractor and is tuned to obtain the optimum VMI condition (the applied voltage is

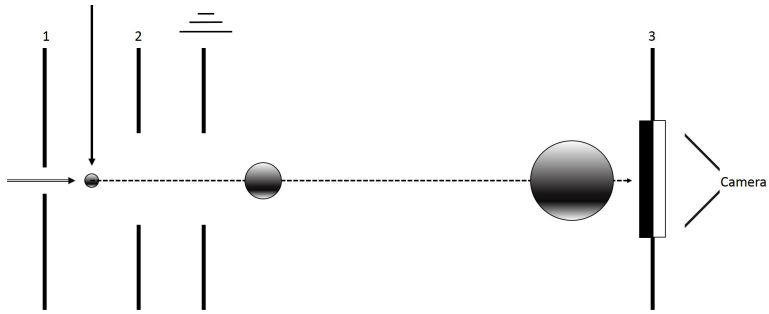

Figure 2.10: *Schematic representation of the Ion/Electtron imaging experiment: from the left the molecular beam enters the interaction region between the repeller (1) and the extractor (2), the laser beam crosses it perpendicularly, then charged particle start their flight. The charged particle sphere expands in the axis of the linear TOF and reaches the detector (3). The 2D image of the 3D sphere is then recorded by a camera.*

usually 2/3 or 3/4 of the Repeller voltage), the third electrode is grounded and delimits the field free region of the TOF. The optimum VMI condition is reached when the FWHM of the peaks is minimum: when the voltages are appropriately set, all the particles with the same velocity are focused on the same point of the detector.

To obtain the photoelectron spectrum it is first necessary to process the image. Usually the Abel Inversion method and the Onion Peeling algorithm are used. The result is a spectrum of the radial intensity of the image.[16,17]

In fig. 2.10 a schematic representation of the experimental setup is reported. In fig. 2.11 a 3D graph of the electron image is shown on the left and the relative photoelectron spectrum (obtained with Onion Peeling) is shown on the right.

This experimental setup was successfully employed for the determination of ionization potential of molecular systems.[18] It is indeed possible to calibrate the detector introducing a relation pixel-energy of the particle. As

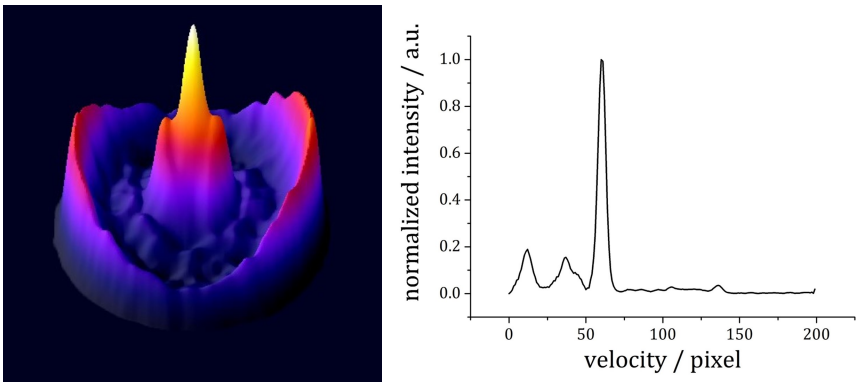

Figure 2.11: *Electron imaging of phenol exciting through the* 0_0^0 *at* $36348cm^{-1}$ *and setting the probe energy at* $32803cm^{-1}$*. Photoelectron image on the left and photoelectron spectrum on the right. The very well known IP of phenol is* $68624cm^{-1}$*, so the energy excess is* $527cm^{-1}$ *and it is attributed to the most external peak, corresponding to electrons ejected with the maximum EKE.*

the radius of the particle distribution is a measure of their speed, a linear relation exists between its square and the energy of the particle. There are two ways of doing this calibration. The first one employs an internal standard: the difference between the total energy stored in the system ($E_{pump} + E_{probe}$) and the known IP of the particle must correspond to the maximum EKE value in the photoelectron spectrum. The ratio between this energy difference and the squared value of the radius corresponding to the most external photoelectron peak gives the energy calibration. A different approach consists of taking different photoelectron spectra of the same chemical species at different probe energies and plotting the total energy provided to the system against the squared value of the radius corresponding to the most external peak in each image. A linear fit of the plotted

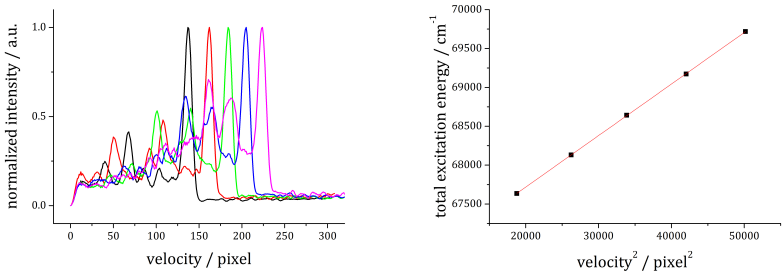

Figure 2.12: *Photoelectron imaging spectra of anisole at different excitation energies (left) and linear energy calibration (right) obtained reporting in the plot the total excitation energy versus the pixel value for the external peak maximum for each single spectrum.*

data is possible according to the expression:

$$h(\nu_1 + \nu_2) = mr^2 + IP \tag{2.29}$$

where the term on the left is the total excitation energy, that corresponds to the sum of the IP and the energy excess given by the squared value of the most external peak radius, times m that is the angular coefficient of the line and gives the energy calibration of the detector. An example of this latter approach is reported in fig. 2.12, using anisole as reference system.

The same experiment described for electrons can be employed for ion detection by changing the signs of the applied potentials. In a simple ionization process a negligible amount of kinetic energy is stored in ions (they are almost $10^4 - 10^5$ times heavier than electrons) and very narrow ion distributions are recorded, but the information they carry can be important. If instead a photodissociation process[19–21] is occurring, then the KER of

the ionic fragment can be measured and the energy balance becomes:

$$h\nu_1 + h\nu_2 = E_I + E_N + \mathrm{EKE} + \mathrm{KER}_I + \mathrm{KER}_N \tag{2.30}$$

where E_I is the internal energy stored in the ionic fragment and KER_I is the kinetic energy release of the ionic fragment, E_N is the internal energy of the neutral fragment and KER_N is the kinetic energy release of the neutral fragment, EKE is as before the electron kinetic energy.

Once the system is pumped at the edge of the dissociation threshold, then it can dissociate only if the electron leaves the system in a highly excited state, i.e. leaves the system with almost zero EKE. Indeed, if a lot of energy is stored in the electron channel and is converted into kinetic energy, the ion is left below the dissociation threshold.

As it's obvious, it is not possible to monitor the KER_N of neutral fragments in a R2PI experiment and their information gets lost. For the determination of dissociation threshold we assume that no internal energy is left in the neutral fragment, whose KER_N is proportional to the mass ratio of the two fragments. The BE is then related to the observed KER_I by the equation:

$$\mathrm{BE} = \mathrm{KER}_I(1 + \frac{m_I}{m_N}) \tag{2.31}$$

where m_N and m_I are the neutral and ionic fragment masses, respectively.

2.4 Time Resolved Ion Imaging

As evidenced in the previous section, the Ion Imaging apparatus is extremely useful for the study of photodissociations. Energy resolved experiments were performed successfully, nonetheless the same approach was

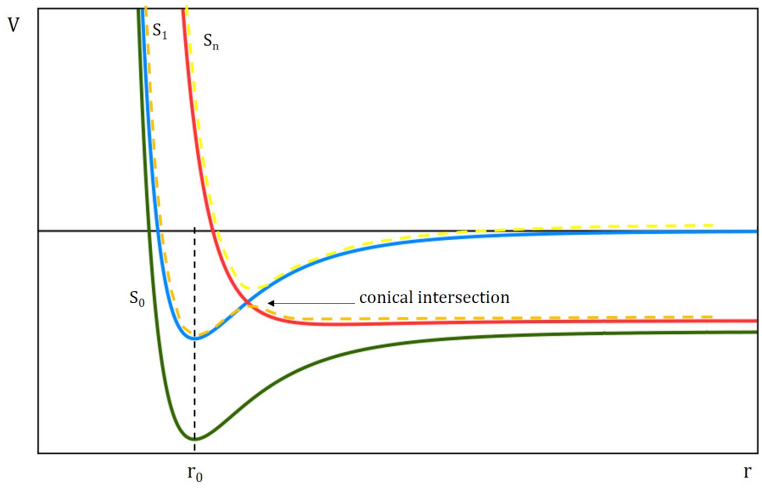

Figure 2.13: *Solid curves represent diabatic PES of ground (S_0, green), first excited (S_1, blue) and highly excited (S_n, red) electronic states. Dashed curves represent adiabatic PES of first excited (S_1, orange) and highly excited (S_n, yellow) electronic states. The conical intersection between S_1 and S_n is evidenced. The reaction coordinate is reported in the x axis.*

employed also for time resolved experiments giving very interesting results. Ultrafast dynamics in electronic excited state were studied with Ion Imaging experimental setup using exciting laser systems providing femtosecond pulses. [16,22]

In a diabatic approach to photodissociations, when the potential energy surface (PES) of a non-dissociative excited state is crossed by the PES of a dissociative upper excited state, a conical intersection is present between the two states. This problem is schematically reported in fig. 2.13. [23]

Adiabatically instead, the PES of the first excited state shows a dip centered at the equilibrium distance r_0 among the dissociative coordinate, where vibrational levels are present. As r increases, an energy barrier is

present and, after a saddle point, the PES is dissociative. Only when enough energy is provided to the system (i.e. the system is pumped above the dissociation barrier), two neutral fragments are produced and move one away from the other with a certain velocity related to the total excitation energy and the internal energy of the fragments.

Using a pulsed laser to promote an electron from the ground state to an excited one, it is possible to induce a dissociation of the neutral system. After the excitation, the production of fragments is probed thanks to a second laser pulse of energy comparable with one electronic transition of the neutral fragment of interest. If the laser power is high enough then the fragment can absorb sinchronously two photons and ionize. This experimental setup is therefore based on a $1 + 2$ photon absorption scheme and allows for two different approaches to the problem. First of all, the dynamics can be probed for different excitation energies while changing the energy of the first photon. Then, it is also possible to probe the production of fragments while changing the delay between the first and the second pulse. The integrated signal due to ions production is measured in a mass spectrometer and, thanks to the position sensitive detector, also the momentum is measured.[24]

The delay between pump and probe photons is ensured by optics mounted on a translator stage that make the optical path of the probe beam longer or shorter with respect to the pump path.

For neutral dissociation of small fragments, like hydrogen or methyl radical, the production of fragments was observed also below the direct dissociation threshold. A tunneling dynamics was suggested as an explanation. In fig. 2.14 the detail of a dissociative adiabatic PES of an electronic excited state is reported and the possible dissociation pathways are shown.[25]

The total ion yield of the parent molecule is due to the R2PI (1+1')

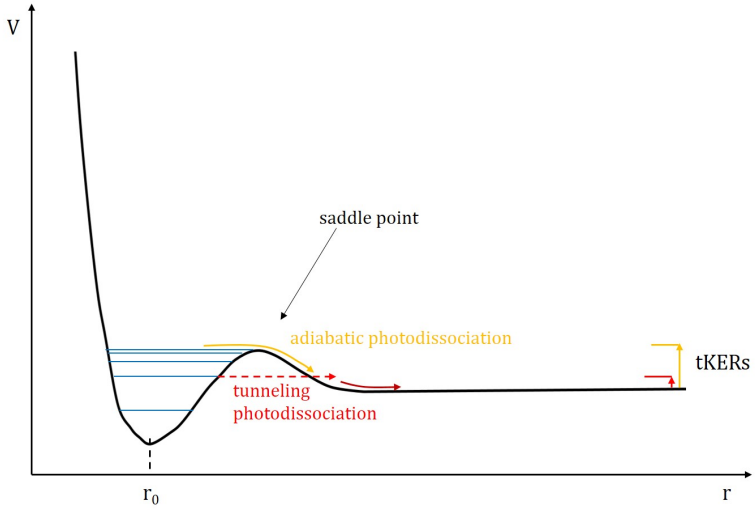

Figure 2.14: *Dissociative adiabatic PES of an electronic excited state. The x axis is the dissociation coordinate (e.g. a RO-H stretching or a RO-CH_3 stretching, in molecular coordinates) On the left, vibrational modes of the undissociated compound are present below the energy barrier. When the system is pumped above the saddle point, a direct dissociation occurs (orange arrow) and the fragment is produced with high kinetic energy release (tKER stands for total KER). When the system is pumped below the saddle point, a tunneling dynamics is possible*

absorption and is monitored as a function of the time delay between 1 and 1' photons (transient spectra are obtained). If dissociation occurs the parent ion yield drops and the fragment ion yield increases as a function of time delay.

2.5 Synchronous ZEKE-MATI

The last section of this chapter is dedicated to the synchronous acquisition scheme for ZEKE and MATI spectra that we developed in the laboratories of the University of Manchester. This new experimental setup was specifically designed for the study of larger mass non-covalent clusters.

This work is going to be submitted in the early 2015 for publication in an international journal.

A new experimental scheme for simultaneous measurement of high resolution and high sensitivity photoelectron (ZEKE) and photoion (MATI) spectra

*François Michels, **Federico Mazzoni**, Maurizio Becucci and Klaus Müller-Dethlefs*

Abstract

An improved setup for the simultaneous measurement of ZEKE and MATI spectra is presented, which has been specifically designed for the study of non-covalently bound aromatic clusters and their photodissociation. A preliminary test was performed on the bare molecule anisole. Some differences

in the results from new detection scheme compared to a previous one[14] *are discussed.*

Introduction

The study of molecular clusters and non-covalent interactions in the gas phase with molecular beam high-resolution spectroscopies such as ZEKE (Zero Electron Kinetic Energy) and MATI (Mass Analysed Threshold Ionisation) has produced a plethora of results for many different systems.[26,27] In particular, clusters formed by a polyatomic molecule with an aromatic system (aniline, phenol) and by a monoatomic rare gas[28–34] (Ar,Kr) or small polyatomic molecules[35–37] (N_2,H_2O) have been studied. The results have been compared to highest level quantum calculations[38] offering a very big contribution to our knowledge of non-covalent interactions by producing very interesting results. In order to extend the experimental methods to more complicated systems, we have further improved the experimental set up with the goal of studying larger molecular clusters by a combined ZEKE/MATI scheme.[39]

Here, a variant experimental scheme has been developed for an improved acquisition of ZEKE and MATI spectra. A method for the synchronous acquisition of and ZEKE has already been presented before[14] : The MATI signal was separated in two components; low-resolution LR-MATI and high resolution HR-MATI. These two components, originating from the field ionization of respectively "red" (field shifted to lower energy) and "blue" (field shifted to higher energy) Rydberg Stark states,[40] were recorded separately in the mass spectrum. This leads to the observation of three mass peaks for each species of interest in the mass spectrum: the direct ion peak, the HR-MATI peak and the LR-MATI peak. Experimen-

tal conditions were chosen to optimize the separation between these three peaks. The optimized conditions need to be changed according to the mass of the fragment of interest. For dissociation processes under study there are at least six peaks of interest: three for the parent species and three for the daughter species. Simultaneously recording the signal over the six mass channels requires a good separation of the triplet peaks for species whose mass difference can be significantly high, and this is not trivial.

However, the new detection scheme presented here has been designed specifically for improving detection sensitivity while also maintaining or improving the resolution required for the study of molecular non-covalently bound clusters of increasing size. Indeed, as will be presented hereafter, the new setup provides a better separation in the mass spectrum between the MATI peak and the direct ion peak. By simultaneously recording the ZEKE electron signal, high-resolution information is obtained allowing for the study of complex dynamics.

Experimental details and results

The experimental apparatus has been described in details in recent papers,[12,41,42] but for clarity the electron/ion extraction system is shown in Figure 2.15. The employed pulse sequence will be discussed further below.

The total ion yield of the parent molecule is due to the R2PI (1+1') absorption and is monitored as a function of the time delay between 1 and 1' photons (transient spectra are obtained). If dissociation occurs the parent ion yield drops and the fragment ion yield increases as a function of time delay.

A supersonic pulsed jet is originated by a General Valve Series 9 valve with $0.5mm$ diameter nozzle. The central part of the expansion, i.e. the

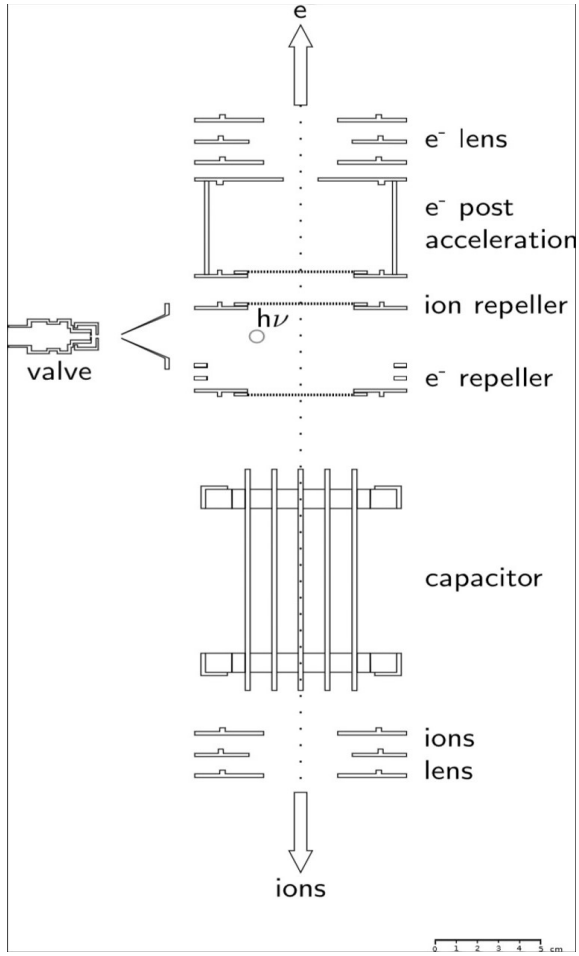

Figure 2.15: *Schematic representation of the experimental setup. The central part of the jet expansion produced by the valve is selected thank to a skimmer and then crossed perpendicularly by the laser beam (hν). After the laser excitation, the voltage sequencies applied to ion repeller and electron repeller allow for charged particles detection in the mass spectrometer.*

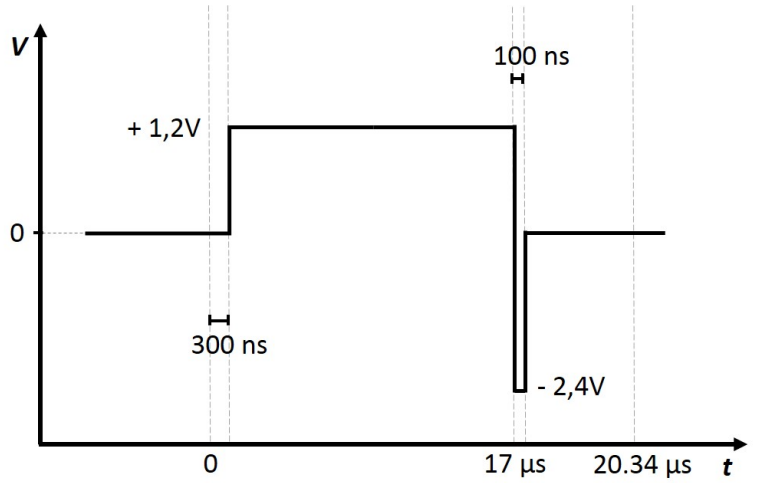

Figure 2.16: *Low voltage sequence applied to the electron repeller for the new synchronous ZEKE-MATI detection scheme.*

coldest one, is selected with a $1.5mm$ diam. skimmer of $30mm$ height and is admitted into the laser interaction region. The distance between skimmer and nozzle is about $4cm$.

Two co-propagating laser beams traveling perpendicularly to the jet expansion are superimposed to permit the two-photon (pump-probe) absorption by the molecular system. The interaction of the laser light with the molecular beam occurs in between the electrodes of the electron/ion extraction system: electron and ion repeller in Fig. 2.15.

The low voltage pulse sequence applied to the electron repeller for the synchronous detection scheme of ZEKE and MATI is reported in figure 2.16. About $300ns$ after the laser excitation a small positive pulse ($+1.2V$) is applied in order to deflect eventually formed ions and electrons, so that they are separated from neutral molecules that remain in the beam. Given

the different mass to charge ratio, the electrons collide with the positive electrode while the ions are just slightly displaced from the neutrals. Possibly, some excited molecules are still neutral, due to electrons promoted to Rydberg states by the laser excitation. The "red" Stark Rydberg states closer to ionization threshold are field-ionized by this pulse and the signature of these states is lost because the corresponding ions/electrons fly away together with the other charges formed by direct laser excitation. The positive pulse lasts $17\mu s$ and a very short ($100ns$) negative pulse of $2.4V$ is then applied. As a result, the "red" and the "blue" Stark states are reversed because the polarity of the field is inverted and the population of the Rydberg states is redistributed over all the Stark states due to this perturbation. The energy higher "blue" states are now field ionized. The resulting electrons are collected to form the zero kinetic energy electrons ZEKE spectrum. These electrons are accelerated through the upper grid of the capacitor that is grounded. Once they have passed this grid, a short ($3\mu s$) $+10V$ pulse is applied to the post-acceleration grid in order to send them into the time-of-flight field free drift tube, at the end of which they are detected by a MCP. The ZEKE signal is then recorded using a Boxcar integrator (Stanford Research Systems SR250). The whole system is enclosed into a three-fold μ-metal tube for magnetic field shielding.

Once the $17\mu s$ pulse is off, ions and both ionized and neutral Rydbergs still fly in between the capacitor plates for $3.04\mu s$, being the neutrals in the molecular beam axis and the ions slightly displaced by the previous electrostatic field. Finally, a high positive voltage ($600 - 1000V$) is applied to the upper plate of the capacitor, the surviving Rydbergs are ionized and all the ions are accelerated downwards through a Reflectron time-of-flight mass spectrometer and revealed with an MCP detector. When the excitation laser is in resonance with a given species and threshold ionization

occurs thanks to the second laser, two different peaks are observed at the relevant mass-to-charge ratio channel in the mass spectrum. The first one is related to the ions directly produced by lasers excitation (together with the few Rydbergs field ionized by the first electric pulse) and the second one is related to all other field ionized Rydbergs. The intensity of first and second peak measured as a function of the laser excitation energy gives the mass-analyzed photoionization efficiency (PIE) spectrum and the mass-analyzed threshold ionization (MATI) spectrum, respectively. TOF mass spectra are measured by an Ortec Fast-Flight2 Digitizer transferred via USB-2 to a PC running dedicated data acquisition software.

The duration of the positive pulse is a compromise between an optimization of the ZEKE signal and a good separation of the ion and MATI signals in the mass spectrum. Shorter pulses will result in a stronger ZEKE signal and a worse separation of ions generated directly by laser excitation or field ionization. Therefore, shorter pulses of higher voltage can be used. Unfortunately, even if it will result in a better temporal separation for the ion peak, this option cannot be considered. Indeed, a worse signal to noise ratio for the threshold signals will be obtained because too many Rydbergs will be field ionized without contributing to the MATI/ZEKE signal, i.e. core Rydbergs will be field ionized by the initial pulse and their signature will be lost in the direct ionization peak.

The new setup has been tested on jet-cooled anisole ($C_6H_5 - O - CH_3$) whose well-known ionic spectrum[43] shows an origin band at $66399 \pm 5 cm^{-1}$.

The dye laser system is described in previous reports. The dye lasers fundamental emission in the visible range is frequency doubled to obtain UV radiation; the finest step for UV tuning is around $0.01 cm^{-1}$ and the emission bandwidth is around $0.06 cm^{-1}$. After every single laser shot, it is possible

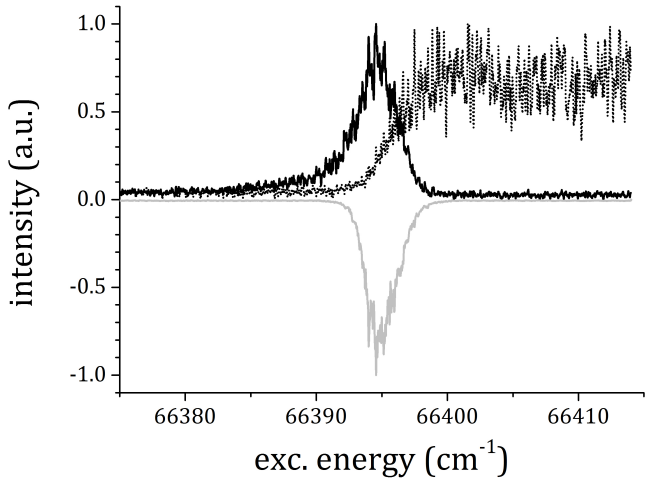

Figure 2.17: *PIE (dotted line), MATI (black line) and ZEKE (grey line, reversed) curves for the anisole showing the origin band of the ionic spectrum.*

to record synchronously more than $50\mu s$ of the mass spectrum thank to the Fast Flight Digitizer. We decided to record the information after one laser shot every four motor-steps and to average the recorded signal for every mass channel with a 19-points weighted "triangular" function.

PIE, MATI and ZEKE curves recorded with the new setup are shown in fig. 2.17, while fig. 2.18 reports a comparison between the results from old and new setup.

The ZEKE peak generated with the new setup shows a well resolved rotational contour and a FWHM as low as $3cm^{-1}$, significantly smaller than the $4cm^{-1}$ FWHM of the HR MATI peak obtained with the old one. As evident from fig. 2.18, the "red" profile of the ZEKE peak is very close to the one of HR MATI while the "blue" profile is very close to the one of LR

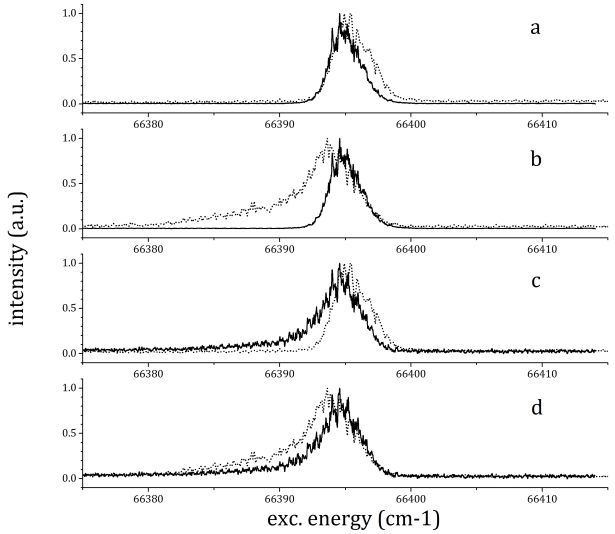

Figure 2.18: *In (a) and (b) the new setup ZEKE spectrum (black line) is compared respectively with HR MATI and LR MATI (dotted lines) from the old setup. In (c) and (d) the new setup MATI (black line) is compared respectively with HR MATI and LR MATI (dotted lines) from the old setup.*

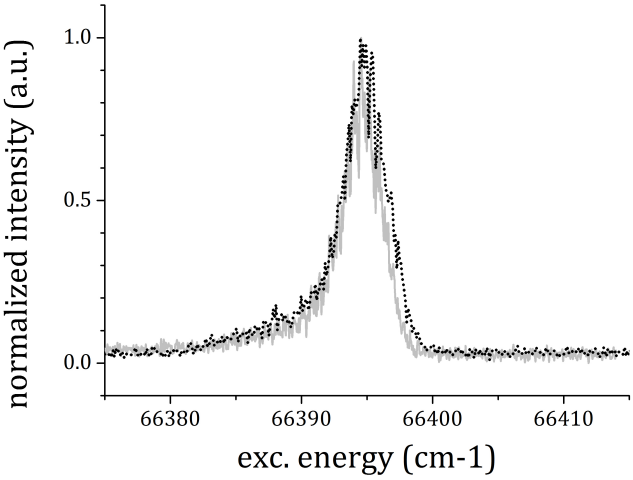

Figure 2.19: *The sum of HR MATI and LR MATI from the old setup (dotted line) is compared to MATI (grey line) from the new setup. The lack of blue tail corresponds to the loss of information from highly excited Rydberg states.*

MATI.

Furthermore, the MATI signal in the new setup gives the same information contained in the sum of HR and LR MATI recorded with the old setup. In fig. 2.19 we show that this is effectively the case for the "red" part of the peak, but not again for the "blue" part. Finally it is important to note that in the old setup for the synchronous detection ZEKE and HR-MATI profiles were identical.

The lack of the "blue" tail in this new setup is related to the long separation pulse: during their flight, neutral Rydbergs that are closer to threshold (and have longer radius) relax to lower excited ones. Obviously, the longer these highly excited Rydbergs fly, the less they survive. Unfortunately the

evidence is that after $17\mu s$ we lose the information of these highly excited states. This is totally acceptable if the aim of the new setup is to permit the study of states whose energy excess with respect to the ionic threshold is of the order of hundreds or thousands wavenumbers as it is the case of polyatomic cluster dissociations.

Conclusions

A new synchronous determination of ZEKE and MATI signals has been designed specifically for the study of big clusters. The new setup allows for a better separation of direct ions mass peak and threshold ions mass peak and permit to preserve the information due to High Resolution Rydbergs in the ZEKE spectrum.

As the purpose is to investigate excesses of energy of the order of thousands of wavenumbers probing dissociation channels in polyatomic clusters, the small information loss for every single peak is not relevant.

The new setup is therefore well suited for the study of molecular systems, such as molecular clusters, that result in weak signals and complex dissociation dynamics.

Bibliography

[1] G. Scoles, *Atomic and molecular beam methods*, Oxford University Press, USA, 1992.

[2] J. M. Hollas, *Modern spectroscopy*, John Wiley & Sons, 2004.

[3] O. Svelto and D. C. Hanna, 1998.

[4] W. Wiley and I. H. McLaren, *Review of Scientific Instruments*, 1955, **26**, 1150–1157.

[5] http://www.rmjordan.com/.

[6] D. Solgadi, C. Jouvet and A. Tramer, *The Journal of Physical Chemistry*, 1988, **92**, 3313–3315.

[7] L. Zandee and R. Bernstein, *The Journal of Chemical Physics*, 1979, **71**, 1359–1371.

[8] S. Kendler, S. Zilberg and Y. Haas, *Chemical physics letters*, 1995, **242**, 139–146.

[9] E. W. Schlag, *ZEKE spectroscopy*, Cambridge University Press, 1998.

[10] C. Jouvet, C. Dedonder-Lardeux, S. Martrenchard-Barra and D. Solgadi, *Chemical physics letters*, 1992, **198**, 419–423.

[11] F. Merkt, *Annual review of physical chemistry*, 1997, **48**, 675–709.

[12] H.-J. Dietrich, R. Lindner and K. Müller-Dethlefs, *The Journal of chemical physics*, 1994, **101**, 3399–3402.

[13] O. Dopfer, G. Lembach, T. G. Wright and K. Müller-Dethlefs, *The Journal of chemical physics*, 1993, **98**, 1933–1943.

[14] C. E. Dessent, S. R. Haines and K. Müller-Dethlefs, *Chemical Physics Letters*, 1999, **315**, 103–108.

[15] A. T. Eppink and D. H. Parker, *Review of Scientific Instruments*, 1997, **68**, 3477–3484.

[16] B. J. Whitaker, *Imaging in molecular dynamics*, Cambridge University Press, 2003, vol. 1.

[17] A. J. Heck and D. W. Chandler, *Annual review of physical chemistry*, 1995, **46**, 335–372.

[18] M. Pasquini, G. Piani, F. Mazzoni, G. Pietraperzia and M. Becucci, *Journal of Molecular Structure*, 2011, **993**, 510–515.

[19] J. R. Gascooke and W. D. Lawrance, *The Journal of Physical Chemistry A*, 2000, **104**, 10328–10335.

[20] F. Mazzoni, M. Pasquini, G. Pietraperzia and M. Becucci, *Physical Chemistry Chemical Physics*, 2013, **15**, 11268–11274.

[21] S. M. Bellm, J. R. Gascooke and W. D. Lawrance, *Chemical Physics Letters*, 2000, **330**, 103–109.

[22] R. De Nalda, J. Izquierdo, J. Durá and L. Bañares, *The Journal of chemical physics*, 2007, **126**, 021101.

[23] R. D. Levine, *Molecular reaction dynamics*, Cambridge University Press, 2005.

[24] K. L. Wells, G. Perriam and V. G. Stavros, *The Journal of chemical physics*, 2009, **130**, 074308.

[25] G. M. Roberts, A. S. Chatterley, J. D. Young and V. G. Stavros, *The Journal of Physical Chemistry Letters*, 2012, **3**, 348–352.

[26] K. Mueller-Dethlefs, O. Dopfer and T. G. Wright, *Chemical Reviews*, 1994, **94**, 1845–1871.

[27] T. L. Grebner, P. v. Unold and H. Neusser, *The Journal of Physical Chemistry A*, 1997, **101**, 158–163.

[28] S. R. Haines, C. E. Dessent and K. Müller-Dethlefs, *Journal of Electron Spectroscopy and Related Phenomena*, 2000, **108**, 1–11.

[29] M. S. Ford and K. Müller-Dethlefs, *Physical Chemistry Chemical Physics*, 2004, **6**, 23–31.

[30] S.-i. Ishiuchi, M. Miyazaki, M. Sakai, M. Fujii, M. Schmies and O. Dopfer, *Physical Chemistry Chemical Physics*, 2011, **13**, 2409–2416.

[31] Q. Gu and J. Knee, *The Journal of chemical physics*, 2008, **128**, 064311.

[32] S. Ullrich, G. Tarczay and K. Müller-Dethlefs, *The Journal of Physical Chemistry A*, 2002, **106**, 1496–1503.

[33] A. Armentano, X. Tong, M. Riese, S. M. Pimblott, K. Müller-Dethlefs, M. Fujii and O. Dopfer, *Physical Chemistry Chemical Physics*, 2011, **13**, 6071–6076.

[34] X. Tong, A. Armentano, M. Riese, M. BenYezzar, S. M. Pimblott, K. Müller-Dethlefs, S.-i. Ishiuchi, M. Sakai, A. Takeda, M. Fujii *et al.*, *The Journal of chemical physics*, 2010, **133**, 154308.

[35] S. Haines, W. Geppert, D. Chapman, M. Watkins, C. Dessent, M. Cockett and K. Müller-Dethlefs, *The Journal of chemical physics*, 1998, **109**, 9244–9251.

[36] J. Braun, T. Mehnert and H. Neusser, *International Journal of Mass Spectrometry*, 2000, **203**, 1–18.

[37] O. Dopfer, G. Reiser, K. Müller-Dethlefs, E. W. Schlag and S. D. Colson, *The Journal of chemical physics*, 1994, **101**, 974–989.

[38] K. Müller-Dethlefs and P. Hobza, *Chemical reviews*, 2000, **100**, 143–168.

[39] C. E. Dessent and K. Müller-Dethlefs, *Chemical reviews*, 2000, **100**, 3999–4022.

[40] H.-J. Dietrich, K. Müller-Dethlefs and L. Y. Baranov, *Physical review letters*, 1996, **76**, 3530.

[41] R. Lindner, H.-J. Dietrich and K. Müller-Dethlefs, *Chemical physics letters*, 1994, **228**, 417–425.

[42] K. Müller-Dethlefs, *High-resolution laser photoionisation and photoelectron studies (Chapter II)*, J. Wiley and Sons, 1995.

[43] M. Pradhan, C. Li, J. L. Lin and W. B. Tzeng, *Chemical physics letters*, 2005, **407**, 100–104.

Chapter 3

The O-H Bond in Phenols

Phenols and substituted phenols were chosen as model systems for probing photodissociation of covalent bonds in aromatic molecules. In particular the hydrogen radical tunneling dissociation among the $O-H$ reaction coordinate was studied using a time-resolved Ion imaging experiment.

3.1 Phenol, Guaiacol, Syringol

The content of this chapter was published in the Journal of Physical Chemistry Letters in 2014 (DOI:10.1021/jz500895w).[1]

Towards Understanding Photodegradation Pathways in Lignins: The Role of Intramolecular Hydrogen Bonding in Excited States

Jamie D. Young, Michael Staniforth, Jacob C. Dean, Gareth Michael Roberts, ***Federico Mazzoni****, Tolga N.V. Karsili, Michael N.R. Ashfold, Timothy S. Zwier, Vasilios G. Stavros*

Abstract

The photoinduced dynamics of the lignin building blocks syringol, guaiacol, and phenol were studied using time-resolved ion yield spectroscopy and velocity map ion imaging. Following irradiation of syringol and guaiacol with a broad-band femtosecond ultraviolet laser pulse, a coherent superposition of out-of-plane OH torsion and/or OMe torsion/flapping motions is created in the first excited $1\pi\pi^*$ (S_1) state, resulting in a vibrational wavepacket, which is probed by virtue of a dramatic nonplanar → planar geometry change upon photoionization from S_1 to the ground state of the cation (D_0). Any similar quantum beat pattern is absent in phenol. In syringol, the nonplanar geometry in S_1 is pronounced enough to reduce the degree of intramolecular H bonding (between OH and OMe groups), enabling H atom elimination from the OH group. For guaiacol, H bonding is preserved after excitation, despite the nonplanar geometry in S_1, and prevents O–H bond fission. This behavior affects the propensities for forming undesired phenoxyl radical sites in these three lignin chromophores and provides important insight into their relative "photostabilities" within the larger biopolymer.

Letter

Second only to cellulose, lignin is the most abundant naturally occurring biopolymer on Earth.[2] Present in the cell walls of all vascular plants, it is responsible for providing structural support, water transport, and protection against microorganisms.[2–6] However, due to the heterogeneous nature of the polymer itself, our knowledge of the precise macromolecular structure of lignin is still lacking. It is known that across different plant species, the various structures, and properties associated with them, are dictated by the stoichiometric proportions of just three monomers, p-coumaryl, coniferyl, and sinapyl alcohols, termed monolignols.[6,7]

Despite the importance of these molecules, very little is known about the photochemistry of lignin or the monolignols themselves. Previous high-resolution spectroscopy measurements have been carried out on the closely related analogues p-vinylphenol,[8,9] p-coumaric acid,[10] and o-methoxyphenol (guaiacol).[11] More recently, Zwier and co-workers have reported the first spectroscopic study of the monolignols and β–O-4/β–β dilignols.[12,13] These studies have provided new insights into the conformer-specific spectroscopies of model lignins, potentially yielding knowledge of structure–function relationships in the larger polymer network through this "bottom-up" study of the building blocks themselves. Here, we use an analogous reductionist approach as a stepping stone for understanding ultraviolet (UV)-induced photodegradation pathways within lignin in greater detail. Currently, it is known that one of the primary mechanisms driving this process involves the photocatalyzed formation of phenoxyl-type (ArO, where Ar refers to the phenol, guaiacol, or syringol parent molecule) radical sites, generated following the loss of H atoms from the OH moiety, eventually leading to undesired discoloration and structural weakening.[14] With this in mind, we elect

to compare and contrast the UV-induced excited-state dynamics of phenol, guaiacol, and syringol (Figure 3.1a–c), which are model chromophores of lignin, derived from p-coumaryl, coniferyl, and sinapyl alcohols, respectively. Unlike phenol, the presence of the methoxy group(s) in guaiacol and syringol, ortho to the hydroxy group, leads to an intramolecular H bond between these two functional moieties, which distorts the geometry from planarity in the first electronically excited $1\pi\pi^*$ state (S_1), relative to the planar ground-state (S_0) structure (Figure 3.1d–f).[12,15] In this Letter, we demonstrate how the different molecular structures of these three UV chromophores in their S_1 states—specifically, the degree of H bonding—can dramatically influence their excited-state dynamics and in turn the relative propensities for forming ArO sites (i.e., their relative "photostabilities"), thereby taking a first step toward a more complete structure–dynamics–function picture of photodegradation in lignin.

The detailed experimental procedure has been described elsewhere[16,17] and in the Supporting Information (SI). The techniques implemented are time-resolved ion yield (TR-IY) spectroscopy[18] and velocity map ion imaging (VMI).[19] Following excitation of phenol, guaiacol, or syringol using a broad-band ($\sim 500 cm^{-1}$) femtosecond (fs) pump pulse, a coherent superposition of low-frequency Franck–Condon (FC)-active modes is excited in the S_1 state, preparing a vibrational wavepacket.[20] As this wavepacket evolves over time, it is then projected (photoionized) onto the ground state of the cation (D_0) using a second time-delayed (Δt) fs probe pulse, and the resulting parent$^+$ ion signal is recorded as a function of Δt. The pump and probe pulses intercept a molecular beam of target molecules seeded in helium. The pump pulse is centered around the S_1 origin band, while the probe pulse is tuned to photoionize slightly above the adiabatic ionization potential (IPad) of the molecule of interest. VMI is also used to monitor

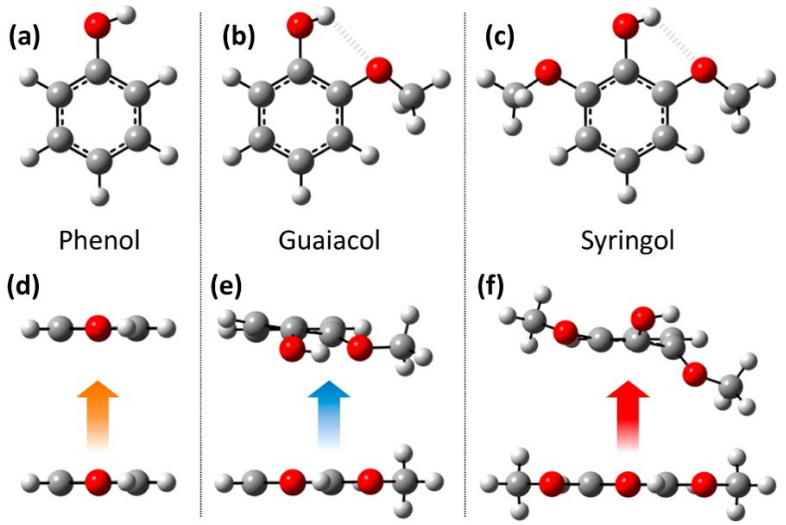

Figure 3.1: *(a–c) Chemical structures of the three monolignol chromophores and (d–f) their molecular geometries in both the ground and excited electronic states of the neutral molecule, S_0 and S_1, respectively. Geometries were calculated using TD-M05-2X/6-311++G(d,p).*

any loss of H atoms after excitation. Any H atoms are resonantly ionized to form H+ with a $243nm$ probe pulse at $\Delta t = 1.2ns$. H^+ ions are then accelerated by an electrostatic potential onto a position-sensitive detector such that ions with the same initial velocity are mapped onto a single pixel on the detector. The recorded 2-D H^+ velocity map images are transformed into desired 1-D total kinetic energy release (TKER) spectra using an image reconstruction algorithm[21] and Jacobian.

We begin our discussion with phenol, which serves as a benchmark for comparison with guaiacol and syringol. Figure 3.2a presents a phenol$^+$ transient (triangles and black line) following excitation at $275nm$ and probing with $300nm$. The IPad of phenol is evaluated as $8.51eV$,[22] and thus, the combined photon energy of $8.64eV$ ($275nm + 300nm$) means that we are only slightly above the IPad by $0.13eV$. The probe wavelengths for phenol, guaiacol, and syringol were chosen specifically in order to be slightly above the IPad, the reason for which we discuss in the ensuing paragraphs. The phenol$^+$ transient is similar to those reported previously using higher probe energies[23,24] and shows a sharp rise at $\Delta t = 0$, which then plateaus across our $5ps$ time window. This plateau is unsurprising, given that the S_1 lifetime of phenol has been previously determined as $\sim 2ns$.(22, 23) Further inspection of the transient also shows that, within the signal-to-noise, the ion signal exhibits no obvious "quantum beating",(19) which suggests that while we are creating a coherent superposition of low-frequency FC-active modes,[25] we are unable to probe this wavepacket motion, in stark contrast to guaiacol and syringol (vide infra). This is re-enforced by the fast Fourier transform (FFT) of this transient (Figure 3.2a, inset), which shows no emerging frequencies.

Figure 3.2b presents a guaiacol$^+$ transient following excitation to S_1 with $278nm$ and probing with $338nm$ (squares and dashed line). The IPad

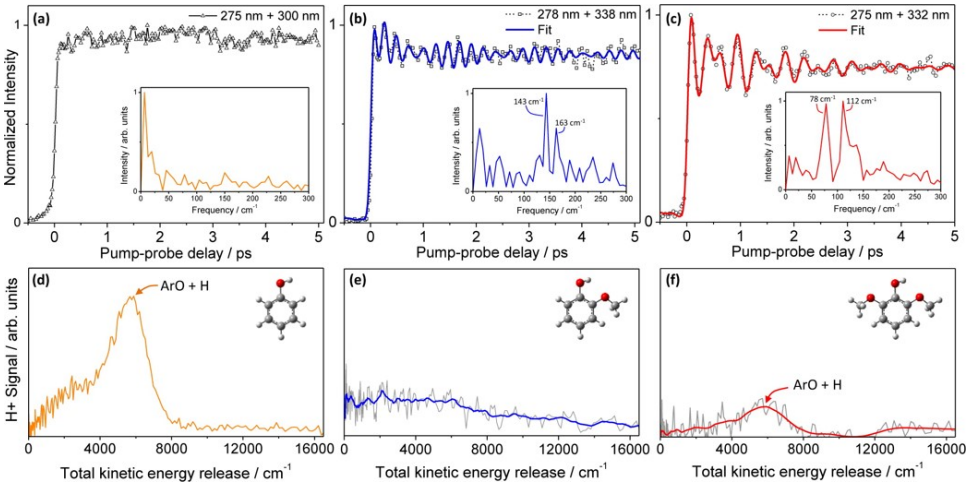

Figure 3.2: *(a–c) TR-IY transients collected from (a) phenol (triangles), (b) guaiacol (squares), and (c) syringol (circles) following UV excitation and subsequent probing (ionization) to the resulting parent$^+$ cation. Superimposed on the guaiacol and syringol data is the sinusoidal fit for each molecule (blue and red lines, respectively). See the text for details. (Inset) The FFT of the relevant transient. (d–f) TKER spectra obtained for (d) phenol at* 275*nm, (e) guaiacol at* 278*nm, and (f) syringol at* 275*nm. In (e) and (f), blue and red lines show a 10 and 15 point average through the raw data (gray), respectively.*

of guaiacol is located at $7.94eV$,[26] with the combined energy of the pump and probe being $8.13eV$, yielding an excess energy of $0.19eV$. The measured transient of guaiacol$^+$ is similar to that recorded for phenol$^+$ in so much that there is an initial sharp rise at $\Delta t = 0$ that then plateaus within our $5ps$ temporal window. However, the similarities with phenol cease here. Following the initial rise, the guaiacol$^+$ signal shows a small but evident sub-$1ps$ decay, with a pronounced quantum beat superimposed on top. We recall that, unlike phenol, the S_1 geometry in guaiacol is nonplanar (Figure 3.1e) in that it distorts out-of-plane in a double minimum potential well. The observed decay is thus attributed to an overall variation in the ionization cross section that follows the initial geometry rearrangement out of the FC region of the initially prepared S_1 state toward the nonplanar minimum (cf. catechol[27]).

We now consider the origins of the observed quantum beat. An analysis of the guaiacol$^+$ transient with a FFT (Figure 3.2b, inset) reveals that the beat contains two dominant frequencies with associated energies of 143 and $163cm^{-1}$ (resulting in periodicities of 233 and $205fs$, respectively), which correspond to wavenumber separations of vibrational eigenstates within the initially prepared wavepacket on S_1.[20] These difference frequencies align very well with the known band separations in an even quanta vibrational progression of the out-of-plane methoxy (OMe) "flapping" mode (φ), which exhibits by far the largest FC activity in the REMPI/LIF spectra (see refs[15,28,29] and the SI). Dean et al. have previously highlighted φ as the dominant motion involved in the initial geometry rearrangement on guaiacol's S_1 surface.[15] Combined with the strong FC activity, the pronounced beating in φ in Figure 3.2b can be understood with reference to the schematic in Figure 3.3, adapted from ref.[15] After excitation from the planar S_0 ground state, a coherent superposition of even quanta in φ creates a

vibrational wavepacket along this normal-mode coordinate on S_1 as the geometry relaxes toward its nonplanar minimum. However, the final D_0 state of guaiacol$^+$ is planar (see the SI), and the nuclear configuration is once again different, now between S_1 (nonplanar) and D_0 (planar), resulting in a variable ionization cross section to D_0 along φ as the wavepacket oscillates on S_1 (Figure 3.3, red arrows). Provided that the vibrational wavepacket is localized (i.e., not dephased), this results in the characteristic beat seen in Figure 3.2b. We highlight that by selecting a probe wavelength such that the combined pump and probe energies far exceed the IPad, the beats in the TR-IY signal for guaiacol$^+$ (as well as syringol$^+$; vide infra and the SI) vanish (cf. ref[27]), demonstrating the sensitivity of the detection window to the probe wavelength (Figure 3.3, green arrows).

At this juncture, it is important to emphasize that a coherent superposition of vibrational levels can be generated irrespective of structural distortion in S_1 relative to S_0 (cf. phenol). However, to probe the temporal evolution of this prepared wavepacket and observe a quantum beat using TR-IY, one requires an adequate FC detection window,[30] which is afforded here by the structural distortion between the S_1 (nonplanar) and D_0 (planar) geometries in guaiacol and guaiacol$^+$, respectively. This is absent in phenol given that S_1 and D_0 are both planar and possess similar geometries.[31,32] The situation described here can be directly likened to the classic study of vibrational wavepacket dynamics in the Cs_2 alkali metal dimer using energy-integrated photoelectron spectroscopy (analogous to TR-IY of the parent$^+$ cation here), where detection of the quantum beating is a sole consequence of different equilibrium nuclear separations for the excited C state of neutral Cs_2 and the ground state of the Cs_2^+ cation.[33,34] We also stress that the FC window for quantum beat detection using TR-IY methods is very sensitive to the probe wavelength; when the combined pump

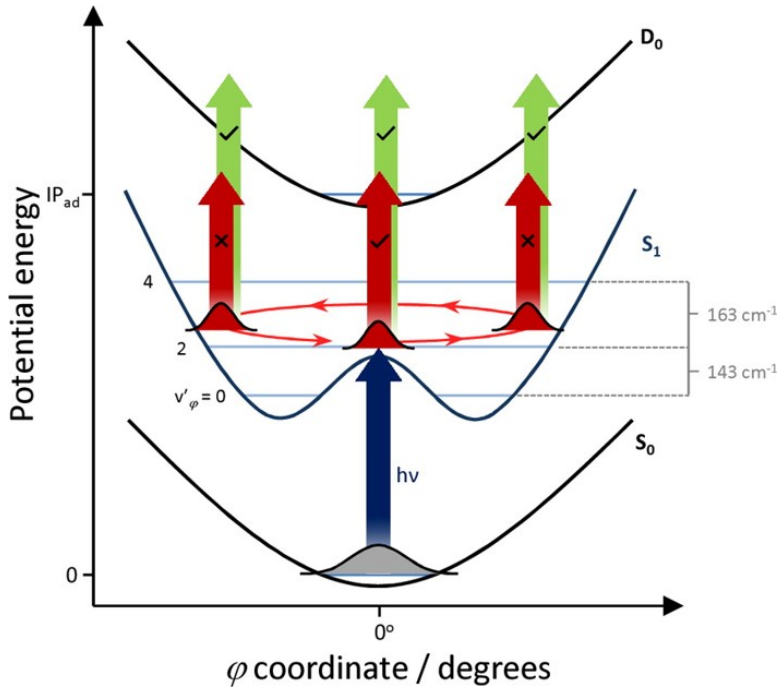

Figure 3.3: *Schematic demonstrating the evolution of the initially excited wavepacket (red) out of the FC detection window along the φ coordinate on the S_1 potential of guaiacol. See the main text for details.*

and probe pulse energy far exceeds the IPad, the beats disappear.[30] Once again, this is directly in line with what we observe here and with previous vibrational wavepacket studies.[34]

The broadness of the peaks in the FFT reflects the limited time window that these beats persist before they dampen out, most likely due to the rapid dephasing of the vibrational wavepacket. This proposition is re-enforced by recalling that our pump pulse is exciting multiple quanta in φ. Indeed, we have extended the guaiacol$^+$ transient out to $100ps$ and find no evidence of revivals, suggesting that population in S_1 is channeled irreversibly into modes orthogonal to φ. This contrasts revivals (and fractional revivals) that have been observed in electronic[35–38] and vibrational wavepackets[39–43] excited in atoms and diatomic molecules, respectively. In order to extract a time constant for the dephasing time, τd, we fit our measured transient to two cosine functions (with frequencies corresponding to the wavenumber separation of the vibrational states extracted from our FFT), superimposed with an exponential decay (fit details in the SI). The results of this fit (Figure 3.2b, blue line) return a dephasing lifetime of $\tau d = 3.0ps$, and we discuss the significance of this value below, in relation to the results obtained for syringol.

Figure 3.2c shows the syringol$^+$ transient obtained following excitation at $275nm$ and probing at $332nm$ (circles and dashed line). The combined photon energy of $8.2eV$ is enough to surmount the $\sim 7.9eV$ IPad in syringol (adiabatic ionization potential scan shown in the SI) with an excess of $\sim 0.3eV$. As with the transient observed in guaiacol (Figure 3.2b), following an initial sharp rise at $\Delta t = 0$, there is a clear beating in the syringol$^+$ signal that dampens almost entirely by $5ps$, with no evidence of revivals (see the SI). Shown in the inset is the FFT of the same data set, which contains two major frequency components of 78 and $112cm^{-1}$ (resulting in

periodicities of 428 and 298*fs*, respectively). There also appears to be a weaker component at $\sim 140 cm^{-1}$; however, implementing the two major frequency components in our fitting algorithm alone is sufficient to return an excellent fit (vide infra and the SI). As with guaiacol, these frequencies correspond to wavenumber separations of vibrational states within the wavepacket on S_1; however, spectral congestion in the known REMPI spectrum of syringol makes assigning these modes more cumbersome (see ref[15] and the SI). Nonetheless, on the basis of (i) the dominant FC activity of the OMe torsion (τOMe) and φ modes upon excitation to S_1 [15] and (ii) the predicted geometry changes in the S_1 state of syringol (Figure 3.1f), these frequencies most likely arise from a coherent superposition of combination modes involving τOMe and φ. Detection of these quantum beats in the TR-IY transient follows for the same reasons outlined above, that is, the presence of a FC detection window arising from the structural distortion between S_1 and D_0 in syringol and syringol$^+$, respectively.

Once again, we fit the syringol$^+$ transient using the method described above (Figure 3.2c, red line) and extract a dephasing time of $\tau d = 1.5 ps$, noticeably faster than that observed in guaiacol (cf. $3.0 ps$). Given that the measured REMPI spectrum of syringol is significantly more congested than that for guaiacol (ref[15] and the SI), it is not surprising that the dephasing time determined for syringol is faster; the greater density of states in the initial superposition drives faster dephasing of the vibrational wavepacket.

Intriguingly, we see that the beats in the syringol$^+$ transient (Figure 3.2c), relative to the total ion signal, have greater amplitude than those observed in the guaiacol$^+$ transient (Figure 3.2b). We offer two possible explanations for this and discuss the validity of each in turn. The first is that in syringol, the initial composition of the wavepacket may only include a limited set of vibrational levels, composed primarily of τOMe

and φ modes. However, the REMPI spectrum suggests that the density of vibrational states in S_1 for syringol is far greater than that of guaiacol, as one would expect for a larger molecule (ref[15] and the SI), likely ruling out this conjecture. The second is that the FC detection window is more localized in nuclear configuration space for syringol than that in guaiacol. Credence to this argument comes from the much greater deviation from planarity in S_1 for syringol versus guaiacol. Indeed, time-dependent density functional theory (TD-DFT) calculations on syringol predict that following excitation from $S_1 \leftarrow S_0$, the H-bonded OMe group distorts $\sim 50°$ out-of-plane in one direction, while the OH group, accompanied to a lesser extent by the "free" OMe group, bends $\sim 25°$ in the other direction (Figure 3.1f). The predicted geometry change is far less pronounced for the OH and OMe groups in guaiacol, as further evidenced by the contrasting profiles of the REMPI/LIF spectra for these two species (see the SI). Given this fact, coupled with the planar syringol$^+$ geometry (calculated at the TD-DFT//M05-2X/6-311++G(d,p) level of theory; see the SI), the magnitude of the modulation in ionization efficiency is expected to be enhanced by virtue of the larger displacement between S_1 and D_0 geometries in syringol (cf. ref[34]). The gradual rise in ion yield, shown in the ionization efficiency scan of syringol (relative to guaiacol) near the adiabatic threshold (see the SI), implies such a scenario.

Given the above evidence for out-of-plane geometry changes in guaiacol and syringol's S_1 states (relative to S_0 and D_0), which are absent in phenol's, we now pose the question, how does this affect the relative propensities for photoinduced H atom loss and formation of ArO sites in these three lignin chromophores? For phenol, recent experimental studies demonstrate that a $1\pi\sigma^*$ (S_2) state, which is dissociative along the O–H coordinate (see the potential energy cuts in ref[18]), is responsible for pro-

ducing ArO + H species at all excitation energies above (and including) the S_1 origin (via either tunneling below an S_1/S_2 conical intersection at $> 248nm$ or by ultrafast coupling onto S_2 at shorter wavelengths), as identified through the characteristic production of high kinetic energy (KE) H atoms([18,44,45] and in accordance with the original postulate of Sobolewski and Domcke.[46] This is illustrated by the peak at $\sim 6000cm^{-1}$ in the representative TKER spectrum in Figure 3.2d. However, as the analogous TKER spectrum in Figure 3.2e shows, no similar high KE signature is observed for the production of ArO + H species in guaiacol. A broad component peaked at low KE is observed, however, which, as we have shown in previous studies, is multicomponent in nature and attributed to both multiphoton processes and statistical unimolecular decay on S_0.[18,27] We interpret the absence of the high KE feature to be a consequence of the intramolecular H bond between the OH and OMe groups, which induces a barrier to O–H dissociation and aborts any formation of ArO + H products.[47] This also suggests that, despite the photoinduced geometry change inferred from our TR-IY measurements and earlier studies,[15] the intramolecular H bond between the OH and OMe groups is still maintained in the initially excited S_1 state of guaiacol, and as a consequence, the S_1 lifetime increases from $\sim 2ns$ in phenol[23,24] to $\sim 7ns$ in guaiacol (see ref[27] and the SI), given that O–H fission is no longer a viable decay pathway. Intramolecular H bonding is also present in the planar S_0 ground state of syringol, although our above analysis suggests that out-of-plane distortion of its OH and OMe groups in S_1 is far more dramatic than that for guaiacol. This is in line with the TD-DFT geometry optimization, presented in Figure 3.1f, which demonstrates a large decrease in the proximity of the H-bonded OH and OMe moieties following photoexcitation ($2.72\mathring{A}$ separation between the H atom in OH and the O atom in OMe in S_1, compared to $2.08\mathring{A}$ in S_0,

and a dihedral angle of $\sim 70°$ between the two groups). This will necessarily weaken the intramolecular H bond, providing a greater potential for the now "free" O–H bond to undergo dissociation. Indeed, the small high KE feature ($\sim 6000 cm^{-1}$) present in the TKER spectrum in Figure 3.2f provides evidence that ArO + H photoproducts are formed from syringol, albeit with a far smaller yield than that observed for phenol (cf. Figure 3.2d), which exhibits no steric/structural constraints to photoinduced O–H fission. In support of this, and unlike guaiacol, we note that the measured S_1 lifetime for syringol ($\sim 2.5 ns$) is more comparable to that of phenol (see the SI). The small broad feature present above $\sim 12000 cm^{-1}$ is attributed to H^+ generated directly through dissociative ionization,[18] given its persistence when setting our probe wavelength off-resonance for H atom detection ($\lambda \neq 243 nm$). For completeness, we note that at much shorter wavelengths ($\leq 220 nm$), all three chromophores generate ArO + H products (see the SI).

We close by returning to our original question of the relative photostabilities of these three lignin chromophores. On the basis of the knowledge that ArO radical formation drives photodegradation of the lignin biopolymer, the relative photostabilities of the chromophore sites can be broadly ordered as guaiacol > syringol > phenol (in order of decreasing stability), which, with the exception of phenol, we understand to largely be dictated by the degree of H bonding preserved after out-of-plane rearrangement in their S_1 excited states. Naturally, the findings from the present study only consider the photostability of lignin's isolated chromophores in the gas phase (and at select wavelengths[48]), although we note that solvation effects (e.g., from H_2O) are likely to be minimal given the highly hydrophobic nature of the larger biopolymer,[14] suggesting that the gas phase can act as a good benchmark here. It is interesting to note that there is evidence of this or-

dering in the composition of natural lignin, which is often dominated by coniferyl alcohol and in many cases contains $< 10\%$ p-coumaryl alcohol.[49] With this in mind, future studies of the lignin building blocks will be important to further verify how this behavior maps onto larger components of lignin; high-resolution spectroscopy measurements already suggest that in para-substituted analogues of these chromophores, distorted excited-state geometries will still likely play a role in the ensuing dynamics.[15] The work presented here therefore offers another key step toward developing a more intimate structure–dynamics–function understanding of photodegradation in lignin.

Supporting Informations

Further experimental details, geometry calculations of guaiacol$^+$ and syringol$^+$, ionization of syringol at higher probe energy, fitting procedure for transients, representative extended transient of syringol$^+$, ionization efficiency scan of syringol, LIF and REMPI spectra in guaiacol and syringol, S_1 lifetime of guaiacol and syringol, calculated barriers to geometric distortion for the S_1 state of guaiacol and syringol, and TKER spectra of guaiacol and syringol derived from H Rydberg atom photofragment translational spectroscopy.

Experimental

A femtosecond (fs) Ti:sapphire laser system consisting of an oscillator and regenerative amplifier (Spectra-Physics, Tsunami and Spitfire XP, respectively) operates at $125Hz$ outputting $40fs$ pulses centred at $800nm$ ($\sim 3mJ$ per pulse). This beam is split equally into three parts and up-converted to give the required pump and probe wavelengths. Pump wavelengths are formed by an optical parametric amplifier (OPA) (Light Conversion,

TOPAS-C), which yields wavelengths in the range 278–275nm ($\sim 5\mu J$ per pulse). Probe photons in the range 243.1–340nm ($\sim 7\mu J$ per pulse) are produced by a second OPA (Light Conversion, TOPAS-C). The choice of probe wavelength allowed for detection of either H atoms, through a resonance enhanced multiphoton ionization (REMPI) scheme to generate H^+ , or the target parent cation. Specifically, for detection of H atom products, this proceeds through the two photon allowed $2s \leftarrow 1s$ transition at 243.1nm. A temporal delay between the pump and probe pulses is generated by passing the 800nm seed beam for the pump OPA through a hollow-gold retroreflector mounted on a computer controlled delay stage (Physik-Instrumente, M-521.DD), providing a maximum temporal window of 1.2ns.

The molecular beam is produced by seeding the target molecules (syringol, guaiacol and phenol), heated in order to obtain sufficient vapour pressure, into helium ($\sim 2bar$). Typical operating temperatures were $\sim 50°C$, $\sim 40°C$ and $\sim 100°C$ for syringol, guaiacol and phenol, respectively. Seeded molecular beam pulses are then generated using an Even-Lavie pulsed solenoid valve[50] operating at a 125Hz repetition rate with a typical opening time of 13μs. The seeded gas pulses pass from the source region ($10^{-6}mbar$) through a 2mm skimmer into the interaction region, which contains the velocity map ion imaging (VMI) optics. Non-resonant multiphoton ionisation of methanol is used to measure the delay position corresponding to temporal overlap of the laser pulses ($\Delta t = 0$), to within an accuracy of $\pm 15fs$. The Gaussian cross-correlation/instrument response function (IRF) was also determined using this method, yielding a value of $\sim 120fs$ full width at half maximum (FWHM).

Following photolysis by the pump pulse ($h\nu_{pu}$), any resulting H atoms are probed using velocity map ion imaging (VMI). Firstly, the H atoms are

ionised by the probe ($h\nu_{pr}$) forming H^+ . The 3-D velocity distribution of H^+ is then focused using a set of three ion optics, mirroring the set up described by Eppink and Parker,[19] onto a position sensitive detector which consists of a pair of micro-channel plates (MCPs) coupled to a P-43 phosphor screen (Photek, VID-240). The rear MCP is gated using a timed voltage pulse in order to detect only H^+ (1 amu). The photoemission from the phosphor screen is captured using a CCD camera (Basler, A-312f) and the 3-D distribution is reconstructed from the collected 2-D image using a polar onion peeling (POP) algorithm.[21] By radially integrating a slice from the center of the reconstructed image, it is possible to produce a total kinetic energy release (TKER) spectrum. This is achieved by using an appropriate Jacobian ($r^2 \propto KE$) and calibration factor, and by considering the mass of the resulting co-fragment. The calibration factor is measured using the known TKER spectrum of HBr recorded at $200nm$.[51]

In addition to VMI measurements, the detector is capable of recording time-resolved ion yield (TR-IY) measurements of the parent cation by monitoring the current output directly from the phosphor screen using an oscilloscope. This enables a time-of-flight mass spectrum to be recorded at each Δt, and the measured total signal is then integrated yielding a TR-IY transient.

Guaiacol$^+$/Syringol$^+$ geometry calculations

Optimized geometry of the D_0 state of the guaiacol$^+$ (a and b) and syringol$^+$ (c and d) parent cations calculated with density functional theory using the M052X hybrid functional[52] at the 6-311++G(d,p) level of theory, using the Gaussian09 computational suite.[53]

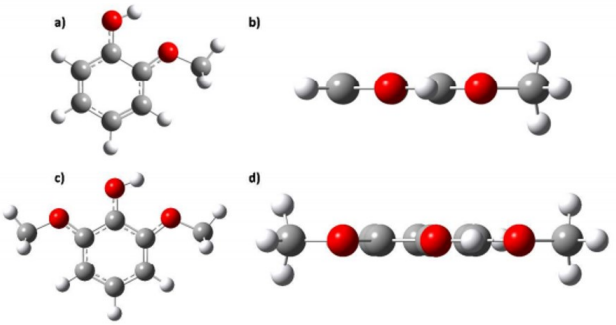

Figure 3.4: *S1*

Syringol ionization at higher energies above IP_{ad}

Ionization of syringol, such that the total pump + probe energy supersedes the adiabatic ionization potential, yields a result similar to that seen for phenol; an initial sharp rise which then plateaus across our $5ps$ time window.[18,23] Inset is the FFT of the reported data. It is clear there is very little evidence of any oscillatory components in the transient.

TR-IY transients are modelled using a combination of (i) an exponential decay, τ_{dec}, reflecting the lifetime of the S_1 state; this is convoluted with a Gaussian IRF, g(Δt), (ii) two cosine components that describe the two oscillatory components from the FFT, ω_1 and ω_2, with associated phase-shifts of p_1 and p_2 (iii) an exponential decay which takes into account the dephasing lifetime, τ_d, of the photoexcited wavepacket and (iv) an exponential decay to reflect the timescale for the initial geometry relaxation from the vertical excitation geometry in S_1, τ_{GR}. These functions are in

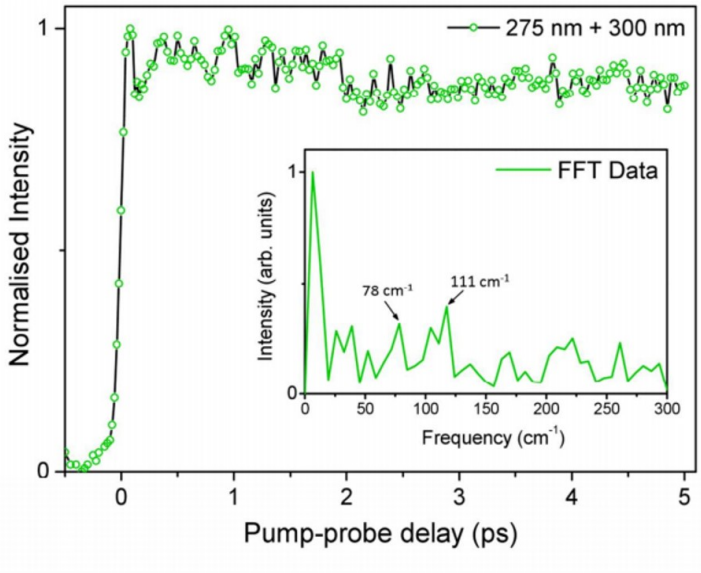
275 nm + 300 nm
Normalised Intensity
Pump-probe delay (ps)
FFT Data
Intensity (arb. units)
Frequency (cm-1)
78 cm-1
111 cm-1

Figure 3.5: *S2*

the order described above, and have the form:

$$y = \left(g(\Delta t) \otimes Ae^{-\frac{\Delta t}{\tau_{dec}}} \right) \times \left(\left[(B\cos((\omega_1 \Delta t) + p_1) + C\cos((\omega_2 \Delta t) + p_2)) \times De^{-\frac{\Delta t}{\tau_d}} \right] + Ee^{-\frac{\Delta t}{\tau_{GR}}} \right) \tag{3.1}$$

In the above, A – E corresponds to the contribution of each component function to the total fit.

Extended time scans

Upon extending to long time scales ($> 5ps$), when investigating syringol, we see no evidence of fractional or full revivals as might be expected in measurements such as this (3.6 (a)). We attribute this to the fact that the S_1 population is funnelled irreversibly into orthogonal modes (further details in main text). To confirm this, we have carried out FFT of different time slices $\Delta t = 5$–$10ps$ (b) and $\Delta t = 10$–$20ps$ (c) to show the diminishing peaks at $78cm^{-1}$ and $112cm^{-1}$ as the vibrational wavepacket dephases and population is channelled into orthogonal modes.

Ionization efficiency scan of syringol

The adiabatic ionization energy for syringol was determined by performing an ionization efficiency scan, carried out by using the frequency-doubled output of two ns-Nd:YAG pumped dye lasers (Radiant Dyes, Narrowscan). The first pulse was fixed at $36063cm^{-1}$ to pump the +308 transition in syringol ($\tau_3^0\varphi_2^0$),[50] while the second pulse was spatially and temporally overlapped with the first and frequency scanned. Upon the onset of the adiabatic ionization energy, syringol ions were generated and detected by

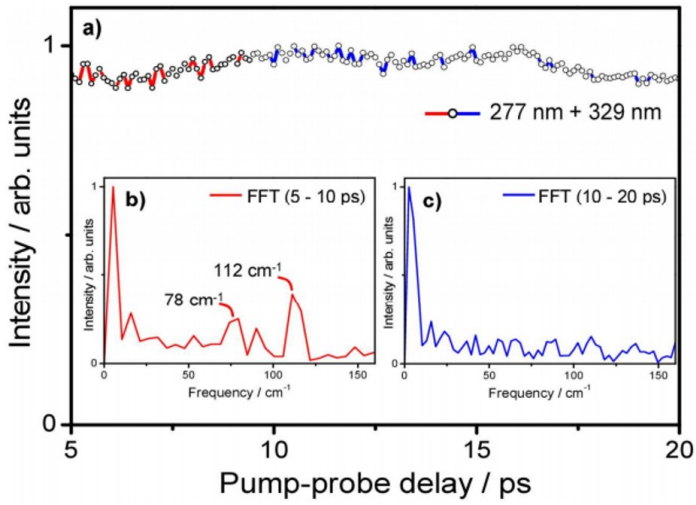

Figure 3.6: *S3*

two-color resonant two-photon ionization (2C-R2PI) in a R.M. Jordan time-of-flight mass-spectrometer. The syringol sample was entrained in a supersonic expansion of neon gas pulsed from a Parker Series 9 General pulsed valve.

LIF and REMPI spectra for guaiacol and syringol

The LIF spectrum in guaiacol was recorded by scanning the frequency-doubled output of a Nd:YAG pumped dye laser while monitoring the total fluorescence signal using a photomultiplier tube. The LIF spectrum shown is in relative wavenumbers with respect to the $S_0 - S_1$ origin ($35923cm^{-1}$), and shows a clear even quanta progression in mode 44, which is the methoxy 'flapping' motion (φ). The R2PI spectrum for syringol, around

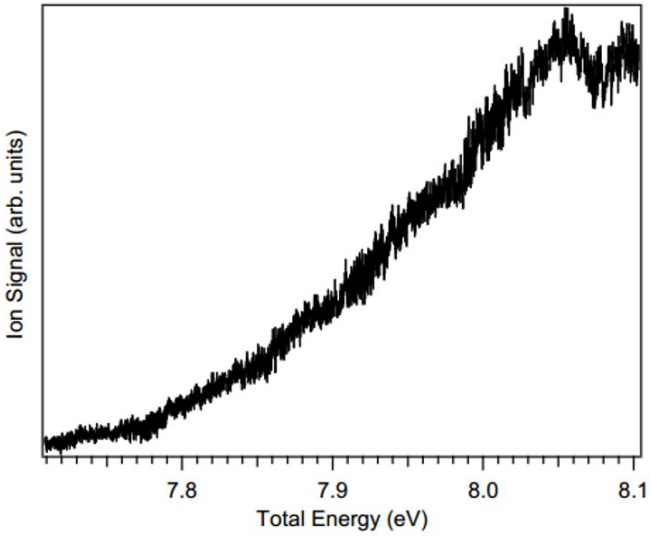

Figure 3.7: *S4*

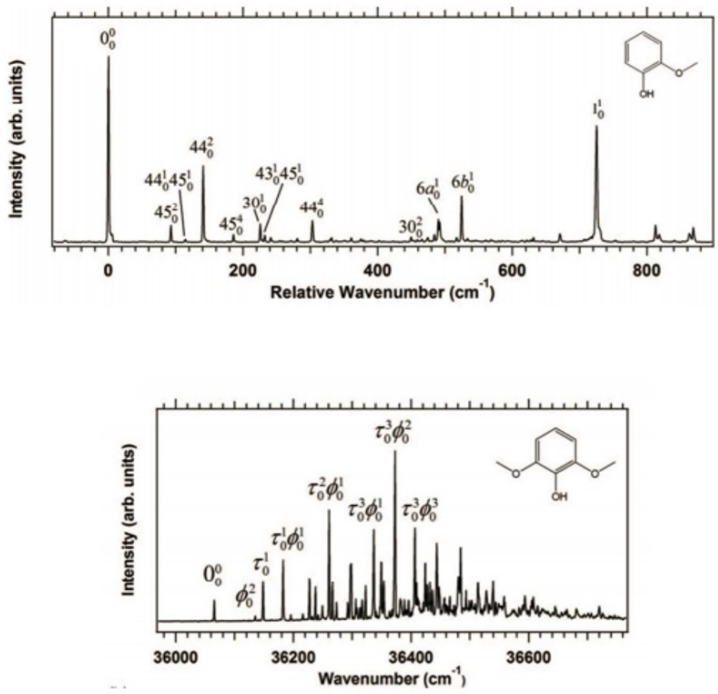

Figure 3.8: *S5*

the $S_0 - S_1$ origin ($36063cm^-1$). Clearly evident in the syringol spectrum is the long Franck-Condon progression in several low-frequency vibrational modes, reflecting the large geometry change between the S_0 and S_1 states. Figures adapted from Dean et al., J. Chem. Phys., 139 (2013) 144313.

S_1 excited state lifetime of guaiacol and syringol

The S_1 excited state lifetime of guaiacol was measured by performing TR-IY measurements on the guaiacol$^+$ parent ion, using a pump wavelength of $278nm$ and a probe wavelength of $243nm$, with pump-probe delays ex-

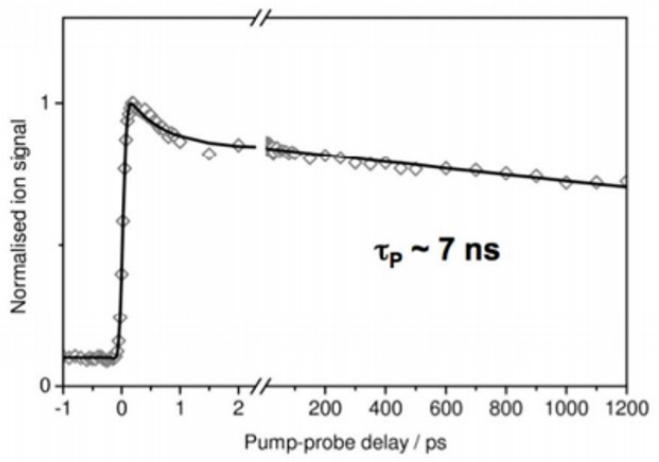

Figure 3.9: *S6*

tending out to $\Delta t = 1.2ns$. The excited state lifetime was extracted by fitting the data to an exponential decay, and yielded a value of $\sim 7ns$. An analogous TR-IY measurement is presented for syringol$^+$ (3.10), following photoexcitation at $270nm$. The S_1 lifetime in syringol is estimated at $\sim 2.5ns$.

Calculated barrier heights in O-H torsion/O-Me flapping coordinates of the S_1 state of guaiacol and syringol.

Optimised S_1 minimum energy, symmetry unconstrained geometries were calculated with time-dependent density functional theory using a variety of functionals with the 6-311++G(d,p) basis set, along with constrained, C_s symmetry, optimised planar transition state geometries. Harmonic frequency calculations were used to identify whether the geometry corre-

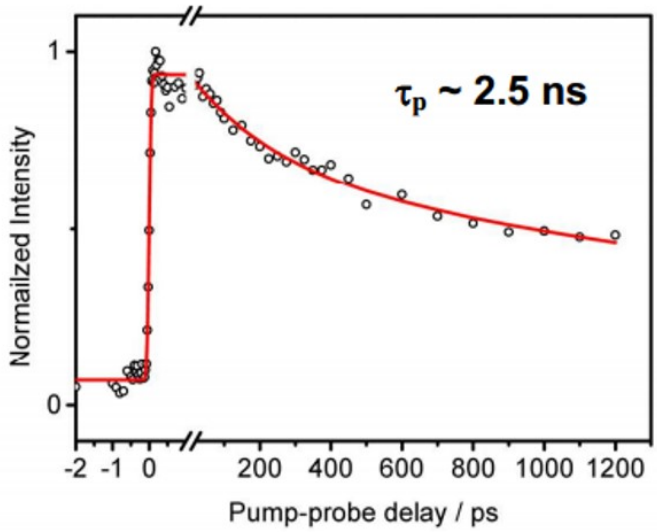

Figure 3.10: *S7*

sponded to either structural minima (no negative frequencies) or maxima (negative frequencies). The energy difference between the two gives the barrier height along the geometry-distorting coordinate in S_1 (cf. Figure 3.3) and these are presented in the table below for both guaiacol and syringol.

Functional	Guaiacol barrier height / cm^{-1}	Syringol barrier height / cm^{-1}
PBE0	610	2259
M05-2X	479	2264
M06-2X	579	2256
CAM-B3LYP	343	2265

H Rydberg atom photofragment translational spectroscopy

TKER spectra derived from H atom time-of-flight (TOF) spectra measured from photolysis of jet-cooled samples of syringol at $215nm$ (top panel) and guaiacol at $220nm$ (lower panel) are shown in Figure 3.11. Excitation of syringol and guaiacol at several shorter UV wavelengths (i.e. at energies above the S_1/S_2 CI) was investigated by H Rydberg atom photofragment translational spectroscopy. As Figure 3.11 shows, TKER spectra derived from the measured H atom TOF spectra are qualitatively similar to those reported previously for photolysis of many other phenols, exhibiting a 'fast' feature centered at TKER $\sim 10000cm^{-1}$ that is consistent with direct O–H bond fission on the[50] $\pi\sigma^*$ (S_2) potential energy surface.

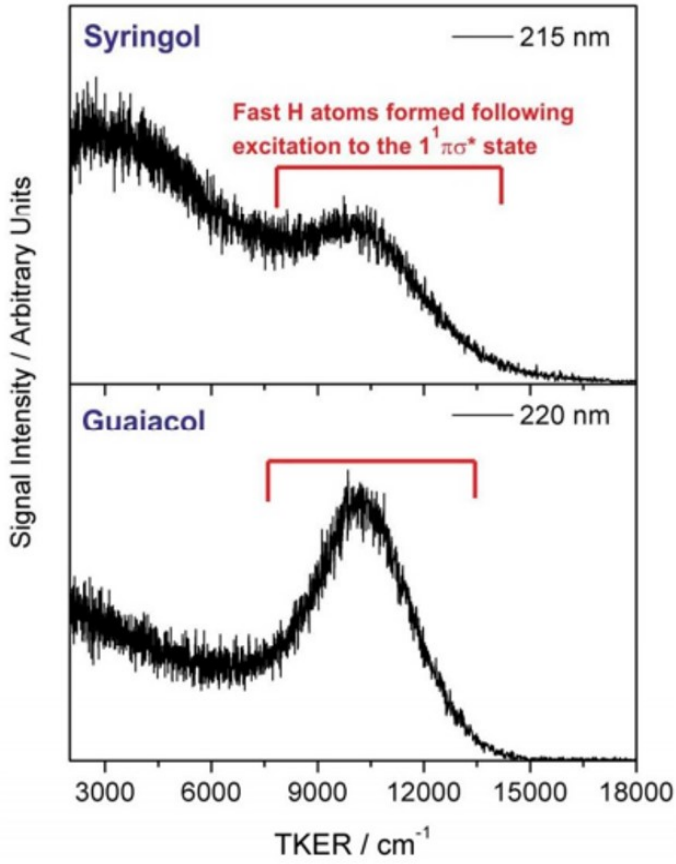

Figure 3.11: *S8*

Bibliography

[1] J. D. Young, M. Staniforth, J. C. Dean, G. M. Roberts, F. Mazzoni, T. N. Karsili, M. N. Ashfold, T. S. Zwier and V. G. Stavros, *The Journal of Physical Chemistry Letters*, 2014, **5**, 2138–2143.

[2] W. Boerjan, J. Ralph and M. Baucher, *Annual Review of Plant Biology*, 2003, **54**, 519–546.

[3] R. Vanholme, B. Demedts, K. Morreel, J. Ralph and W. Boerjan, *Plant Physiology*, 2010, **153**, 895–905.

[4] K. Morreel, H. Kim, F. Lu, O. Dima, T. Akiyama, R. Vanholme, C. Niculaes, G. Goeminne, D. Inzé, E. Messens, J. Ralph and W. Boerjan, *Analytical Chemistry*, 2010, **82**, 8095–8105.

[5] E. R. E. van der Hage, J. J. Boon, R. J. J. M. Steenvoorden and T. L. Weeding, *Analytical Chemistry*, 1994, **66**, 543–550.

[6] D. V. Evtuguin and F. M. L. Amado, *Macromolecular Bioscience*, 2003, **3**, 339–343.

[7] S. Reale, A. Di Tullio, N. Spreti and F. De Angelis, *Mass Spectrometry Reviews*, 2004, **23**, 87–126.

[8] M. de Groot, W. J. Buma, E. V. Gromov, I. Burghardt, H. Köppel and L. S. Cederbaum, *The Journal of Chemical Physics*, 2006, **125**, –.

[9] P. J. Morgan, D. M. Mitchell and D. W. Pratt, *Chemical Physics*, 2008, **347**, 340–345.

[10] S. Smolarek, A. Vdovin, D. L. Perrier, J. P. Smit, M. Drabbels and W. J. Buma, *Journal of the American Chemical Society*, 2010, **132**, 6315–6317.

[11] E. Fujimaki, A. Fujii, T. Ebata and N. Mikami, *The Journal of chemical physics*, 1999, **110**, 4238–4247.

[12] C. P. Rodrigo, W. H. James III and T. S. Zwier, *Journal of the American Chemical Society*, 2011, **133**, 2632–2641.

[13] J. C. Dean, P. S. Walsh, B. Biswas, P. Ramachandran and T. S. Zwier, *Chemical Science*, 2014, **5**, 1940–1955.

[14] B. George, E. Suttie, A. Merlin and X. Deglise, *Polymer Degradation and Stability*, 2005, **88**, 268–274.

[15] J. C. Dean, P. Navotnaya, A. P. Parobek, R. M. Clayton and T. S. Zwier, *The Journal of chemical physics*, 2013, **139**, 144313.

[16] A. Iqbal and V. G. Stavros, *The Journal of Physical Chemistry A*, 2009, **114**, 68–72.

[17] K. L. Wells, G. Perriam and V. G. Stavros, *The Journal of chemical physics*, 2009, **130**, 074308.

[18] G. M. Roberts and V. G. Stavros, *Chemical Science*, 2014, **5**, 1698–1722.

[19] A. T. Eppink and D. H. Parker, *Review of Scientific Instruments*, 1997, **68**, 3477–3484.

[20] A. H. Zewail, *Angewandte Chemie International Edition*, 2000, **39**, 2586–2631.

[21] G. Roberts, J. Nixon, J. Lecointre, E. Wrede and J. Verlet, *Review of Scientific Instruments*, 2009, **80**, 053104.

[22] R. J. Lipert and S. D. Colson, *The Journal of chemical physics*, 1990, **92**, 3240–3241.

[23] G. M. Roberts, A. S. Chatterley, J. D. Young and V. G. Stavros, *The Journal of Physical Chemistry Letters*, 2012, **3**, 348–352.

[24] G. Pino, A. Oldani, E. Marceca, M. Fujii, S.-I. Ishiuchi, M. Miyazaki, M. Broquier, C. Dedonder and C. Jouvet, *The Journal of chemical physics*, 2010, **133**, 124313.

[25] M. G. Nix, A. L. Devine, B. Cronin, R. N. Dixon and M. N. Ashfold, *The Journal of chemical physics*, 2006, **125**, 133318.

[26] L. Yuan, C. Li, J. L. Lin, S. C. Yang and W. B. Tzeng, *Chemical physics*, 2006, **323**, 429–438.

[27] A. S. Chatterley, J. D. Young, D. Townsend, J. M. Żurek, M. J. Paterson, G. M. Roberts and V. G. Stavros, *Physical Chemistry Chemical Physics*, 2013, **15**, 6879–6892.

[28] R. Wu and B. Brutschy, *Chemical physics letters*, 2004, **390**, 272–278.

[29] A. Longarte, C. Redondo, J. A. Fernández and F. Castaño, *The Journal of chemical physics*, 2005, **122**, 164304.

[30] V. Engel, *Chemical physics letters*, 1991, **178**, 130–134.

[31] J. LeClaire, R. Anand and P. Johnson, *The Journal of chemical physics*, 1997, **106**, 6785–6794.

[32] S. Schumm, M. Gerhards and K. Kleinermanns, *The Journal of Physical Chemistry A*, 2000, **104**, 10648–10655.

[33] G. Rodriguez and J. Eden, *Chemical physics letters*, 1993, **205**, 371–379.

[34] G. Rodriguez, P. John and J. Eden, *The Journal of chemical physics*, 1995, **103**, 10473–10483.

[35] J. Verlet, V. Stavros, R. Minns and H. Fielding, *Journal of Physics B: Atomic, Molecular and Optical Physics*, 2003, **36**, 3683.

[36] J. R. Verlet, V. Stavros, R. Minns and H. Fielding, *Physical review letters*, 2002, **89**, 263004.

[37] V. G. Stavros, J. A. Ramswell, R. A. L. Smith, J. R. R. Verlet, J. Lei and H. H. Fielding, *Phys. Rev. Lett.*, 1999, **83**, 2552–2555.

[38] J. Wals, H. Fielding, J. Christian, L. Snoek, W. Van der Zande and H. v. L. van den Heuvell, *Physical review letters*, 1994, **72**, 3783.

[39] M. Dantus, R. Bowman and A. Zewail, *Nature*, 1990, **343**, 737–739.

[40] P. Farmanara, H.-H. Ritze, V. Stert and W. Radloff, *Chemical physics letters*, 1999, **307**, 1–7.

[41] I. Fischer, M. J. Vrakking, D. Villeneuve and A. Stolow, *Chemical physics*, 1996, **207**, 331–354.

[42] M. J. Vrakking, D. Villeneuve and A. Stolow, *Physical Review A*, 1996, **54**, R37.

[43] H. Goto, H. Katsuki, H. Ibrahim, H. Chiba and K. Ohmori, *Nature Physics*, 2011, **7**, 383–385.

[44] R. N. Dixon, T. A. Oliver and M. N. Ashfold, *The Journal of chemical physics*, 2011, **134**, 194303.

[45] M. N. Ashfold, A. L. Devine, R. N. Dixon, G. A. King, M. G. Nix and T. A. Oliver, *Proceedings of the National Academy of Sciences*, 2008, **105**, 12701–12706.

[46] A. Sobolewski, W. Domcke, C. Dedonder-Lardeux and C. Jouvet, *Physical Chemistry Chemical Physics*, 2002, **4**, 1093–1100.

[47] Y. L. Yang, Y.-C. Ho, Y. A. Dyakov, W.-H. Hsu, C.-K. Ni, Y.-L. Sun, W.-C. Tsai and W.-P. Hu, *Physical Chemistry Chemical Physics*, 2013, **15**, 7182–7190.

[48] The present studies have focused on photoexcitation around the S1 origin of these chromophores. At higher excitation energies (less than 220nm), we acknowledge that H atom loss from the OH group becomes active in all three chromophores (see the SI). This does not, however, affect our overall conjecture about their relative photostabilities within lignin, given that (i) solar irradiance will be significantly reduced at these much shorter UV wavelengths and (ii) the total propensity for O–H bond fission across their full UV absorption range still follows the order given in the main text.

[49] M. Baucher, B. Monties, M. V. Montagu and W. Boerjan, *Critical reviews in plant sciences*, 1998, **17**, 125–197.

[50] U. Even, J. Jortner, D. Noy, N. Lavie and C. Cossart-Magos, *The Journal of Chemical Physics*, 2000, **112**, 8068–8071.

[51] P. M. Regan, S. R. Langford, A. J. Orr-Ewing and M. N. Ashfold, *Journal of Chemical Physics*, 1999, **110**, 281–288.

[52] Y. Zhao, N. E. Schultz and D. G. Truhlar, *Journal of Chemical Theory and Computation*, 2006, **2**, 364–382.

[53] M. J. Frisch, G. W. Trucks, H. B. Schlegel, G. E. Scuseria, M. A. Robb, J. R. Cheeseman, G. Scalmani, V. Barone, B. Mennucci, G. A. Petersson, H. Nakatsuji, M. Caricato, X. Li, H. P. Hratchian, A. F. Izmaylov, J. Bloino, G. Zheng, J. L. Sonnenberg, M. Hada, M. Ehara, K. Toyota, R. Fukuda, J. Hasegawa, M. Ishida, T. Nakajima, Y. Honda, O. Kitao, H. Nakai, T. Vreven, Jr, J. E. Peralta, F. Ogliaro, M. Bearpark, J. J. Heyd, E. Brothers, K. N. Kudin, V. N. Staroverov, R. Kobayashi, J. Normand, K. Raghavachari, A. Rendell, J. C. Burant, S. S. Iyengar, J. Tomasi, M. Cossi, N. Rega, J. M. Millam, M. Klene, J. E. Knox, J. B. Cross, V. Bakken, C. Adamo, J. Jaramillo, R. Gomperts, R. E. Stratmann, O. Yazyev, A. J. Austin, R. Cammi, C. Pomelli, J. W. Ochterski, R. L. Martin, K. Morokuma, V. G. Zakrzewski, G. A. Voth, P. Salvador, J. J. Dannenberg, S. Dapprich, A. D. Daniels, Farkas, J. B. Foresman, J. V. Ortiz, J. Cioslowski and D. J. Fox, *Gaussian 09 Revision A.02*, Gaussian Inc. Wallingford CT 2009, 2009.

Chapter 4

Non-Covalent interactions in Phenol Clusters

The phenol hydroxyl group can be involved in the formation of intermolecular non-covalent bonds with sorrounding molecules thank to the non-bonding electron doublet of the oxygen or to the hydrogen.[1,2] In the previous chapter it was evidenced how, if the hydrogen is involved in the formation of a bond (in that case an intramolecular hydrogen bond) as in case of guaiacol and syringol, the $O-H$ reaction coordinate is quenched totally or at least partially. When the intermolecular bond is with water for example, the $O-H$ reaction coordinate is totally quenched for the (1-1) cluster and becomes active again only from the (1-3) cluster up to bigger ones.[3,4]

The phenol-water (1-1) dissociation dynamics is not an ultrafast process and involves a statistical redistribution of the energy. As an energy barrier is present in the dissociative PES, to reach the dissociation threshold a certain excess of energy has to be provided to the system. Only when an

highly excited internal vibrational mode is populated the excess of vibrational energy is redistributed thank to IVR and non-adiabatic couplings to low energy van der Waals vibrational modes allowing for the dissociation.

The dissociation dynamics of phenol-water complex (1:1) was studied in an energy-resolved Ion Imaging experiment. Even if the values for the IP and the BE were already known from studies with different approaches,[5,6] this system has been used as a benchmark for the Ion Imaging setup, that had never been used before for the study of tightly bonded clusters and complexes with small FC factors for the $D_0 \leftarrow S_1(S_0)$ transition.

4.1 Phenol-Water

The content of this chapter was submitted to the Journal of Molecular Structure.

Determination of binding energy in molecular clusters by ion imaging methods: a test on the phenol-water 1:1 cluster

Federico Mazzoni, *Massimiliano Pasquini, Giangaetano Pietraperzia, Maurizio Becucci*

Abstract

In this paper we present a test on the velocity mapping imaging approach for the experimental direct determination of the binding energy in clusters formed by strongly interacting polyatomic molecules. The method is applied to the phenol-water cluster, a system for which the binding energies

were already determined in different experiments. The binding energy values that we obtained, $1975cm^{-1}$ *in the* S_0 *state,* $2327cm^{-1}$ *in the* S_1 *state and* $6586cm^{-1}$ *in the ionic* D_0 *state, are in very good agreement with the previous determinations. We report our results and we discuss advantages and limitations resulting from our experience.*

Introduction

Recently many experimental data have become available on molecular clusters.[7–15] The determination of the cluster structure is the key to access its properties and to evaluate the subtle balance of different terms in the intermolecular potential that is responsible for its stabilization. However the determination of the binding energy of the cluster provides an even more fundamental property of the system. Energies are the simplest quantities that are calculated in any kind of theoretical methods used for modeling of the intermolecular interaction.

The most precise structural determinations are obtained thanks to rotationally resolved spectroscopic data.[12–14] Even though the direct inversion from the moments of inertia to the structure cannot be done, a satisfactorily modeling of the system can be made with some minor assumptions. Alternatively, the frequency shift of selected vibrational bands can give an indication on the cluster geometry. In particular, this is the case of clusters formed by a direct link of the two molecular moieties through a single interatomic coordinate: many hydrogen bonded clusters were studied thanks to hole-burning infrared-UV double resonance experiments.[15]

The cluster binding energy is usually experimentally derived from microwave and infrared absorption spectroscopy, single and two photons ionization, dispersed fluorescence, and stimulated emission pumping.[16]

Here we will focus on resonance enhanced 2 photon ionization (R2PI) experiments. In this case a pump and probe scheme is used where the pump laser is in resonance with a vibronic transition of the cluster and the probe laser is frequency tuned above the ionization threshold of the cluster. When the total excitation energy is above the dissociation threshold in the ionic state, the ion yields in the different mass channels change: increasing the available energy the ion yield at the mass of the fragments grows. In order to get further details on the dissociation dynamics and to determine more precisely the binding energy also ion imaging methods were used. The first publications based on velocity mapping (VMI) [17] ion imaging experiments were dealing mostly with studies on clusters formed by aromatic molecules with rare gas atoms. [18,19] In VMI arrangement, particles with the same velocity are focused in the same point of the detector. The detector is normally time-gated in order to select particles with a given mass/charge ratio. It is then possible to reveal the fragment ions formation from the selective excitation of a cluster and also to measure their recoil speed. The kinetic energy release (KER) from dissociation can be derived from the recoil speed. If the dissociation process is really statistical then it should be possible to observe production of fragments with the maximum kinetic energy (or, equivalently, with zero internal energy). With a single measurement, this experiment could provide an upper limit to the dissociation energy. [20] Otherwise, if measurements are repeated for different total excitation energies, it could lead to a clear picture of the fragmentation dynamics, potentially increasing the accuracy in the determination of the dissociation energy (both dissociation yield and maximum recoil energy are decreasing linearly to zero when excitation energy approaches the dissociation threshold). As in conventional R2PI experiments the fragment ion yield can be measured and used to determine the ionization threshold of

the cluster.

This paper aims to validate the R2PI-ion imaging method for determination of the binding energy in tightly bonded molecular cluster and to discuss limits and possible sources of error in the experiment. The test was stimulated by the recent discussion on the S_0 binding energy determination of the anisole dimer due to the significant difference between calculated ($1480 cm^{-1}$)[21] and experimental ($3926 cm^{-1}$)[20] values. We report on a study of the phenol-water complex: a simple model cluster where a strong interaction exists, dominated by hydrogen bonding. The structure was clearly determined both by microwave and high resolution electronic spectroscopy.[1,22] The dissociation energy was already measured by the Neusser group in a mass analyzed threshold ionization (MATI) experiment carried out in a time-of-flight mass spectrometer.[6] The ionization threshold for the cluster was measured to be $64024(10) cm^{-1}$ and fragments appeared only above $70000 cm^{-1}$ excitation energy. In that spectral region the authors reported a very weak signal, much likely due to unfavorable Franck-Condon (FC) factors for the ionization from the S_1 vibrationless level. The onset for dissociation in the ionic ground state, D_0, was then set to $6520(50) cm^{-1}$. That, in combination with the accurate spectroscopic data available for phenol and for the $S_1 \leftarrow S_0$ electronic transition of the phenol-water cluster, leads to the value of $1916(50) cm^{-1}$ for the binding energy in the neutral ground state. Different ab initio evaluations of the binding energy in the ground state are in reasonable agreement with the experimental values. Calculations based on the Möller-Plesset perturbation theory, with different basis sets, gave values between 1760 and $2416 cm^{-1}$.[23,24]

Experimental

The velocity mapping ion/electron imaging spectrometer was already described in previous papers.[25,26] We form the phenol-water cluster in a pulsed molecular beam by an adiabatic expansion of a gas mixture through a pulsed valve ($500\mu m$ nozzle) in a vacuum chamber. The mixture is prepared flowing helium at $300kPa$ over a sample of phenol at room temperature: as phenol is highly hygroscopic the sample already contains enough water to observe the phenol-water cluster. The central part of the gas expansion is spatially filtered by a skimmer and enters into the interaction region where the background pressure is of the order of 10^{-6} mbar. To selectively excite the cluster and induce fragmentation we use a R2PI scheme. A first photon promotes ground state clusters to the S_1 electronically excited state (band of the $S_1 \leftarrow S_0$ electronic transition at $35996cm^{-1}$)[27] and a second one brings the cluster above the ionization threshold. In order to observe dissociation, the frequency of the second photon is scanned and a large amount of internal excitation is provided to the clusters. We scan the frequency of the second photon between 33300 and $34900cm^{-1}$. Laser interaction takes place between the electrodes of an electrostatic lens that consists of repeller, extractor and ground. The velocity mapping condition is achieved by setting an appropriate voltage ratio between repeller and extractor, given the geometry of the experiment. We use a space separation of $15mm$ between the electrodes with voltages set at 2000 and 1700 volts for repeller and extractor, respectively. The extractor voltage is optimized trying to get the maximum achievable resolution in the photoelectron spectrum of phenol. We show in Figure 4.1 the 3D reconstruction of the 2D image of photoelectrons emitted from phenol. The radial distribution function is used to calculate the electrons kinetic energy (EKE) spectra. The

"onion peeling" algorithm[28] is used for image elaboration and radial distribution determination. This photoelectron spectrum is used to calibrate the imaging detector. The calibration of the images can be immediately transferred to all the other particle distributions, provided the geometry of the experiment and the voltages (absolute values) are fixed. The images can be magnified increasing the time of flight of the charged particles, as to say, reducing the absolute value of the electrodes voltages. In case of experiments with ions the voltage reduction strongly affects the ions detection efficiency: in the present case a voltage at the repeller below 2000 volts is unpractical for the limited signal to noise ratio achieved. This factor represents a strong limitation in the present experiment as the momentum conservation law during dissociation allows only for a very low speed of the phenol fragments. In fact, the momentum of both particles released must be the same, and the speed ratio is then the reciprocal of the mass ratio. As phenol and water masses are 94 and 18 a.m.u., respectively, the speed ratio is

$$s_{\text{water}}/s_{\text{phenol}} \sim 5 \tag{4.1}$$

In our excitation scheme we produce only phenol ions, therefore the resulting images have a very small radius.

In order to detect only the desired ions, during the acquisition of images, the detector is active only at the corresponding arrival time.

Results and Discussion

Figure 4.2 shows the 3D reconstruction of the 2D image of photoelectrons emitted from the 1:1 phenol-water cluster upon 2-photon 2-color ($35996 + 28572 cm^{-1}$) resonant ionization and the associated KE photo-

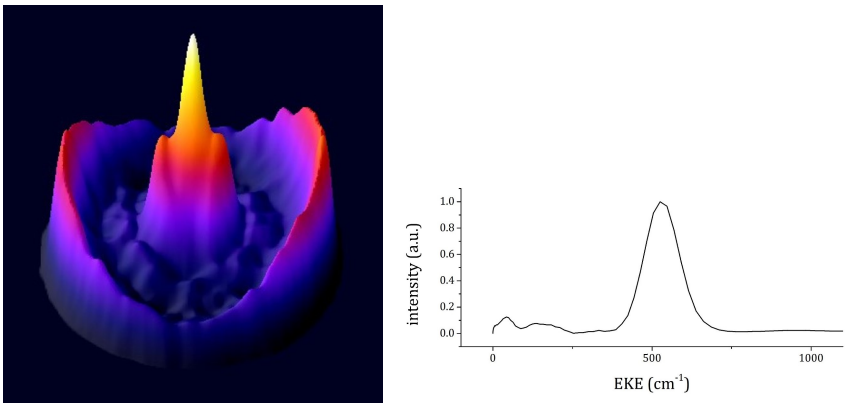

Figure 4.1: *Photoelectrons from R2PI experiment on phenol through the band of the $S_1 \leftarrow S_0$ electronic transition. 3D reconstruction of the photoelectron image on the 2D detector in use. False colours are used to represent the changes in intensity. The total excitation energy is $69151 cm^{-1}$. On the right, it is also reported the corresponding electron kinetic energy spectrum.*

electron spectrum. Assuming that the fastest electrons are associated to threshold ionization of the cluster, the phenol-water ionization potential IP is determined to be $64014(10) cm^{-1}$, in very good agreement with the value of $64025(4) cm^{-1}$ reported in literature.[6,29] Then, taking this peak as the reference it is possible to compare the energy shifts of the inner peaks with the vibrational frequencies of the ion (Fig. 4.2, right).[29] Figure 4.3 shows the 3D image of phenol ions produced by dissociation of the phenol-water cluster upon 2-photon 2-colour excitation (pump at $35996 cm^{-1}$, in resonance with the $S_1 \leftarrow S_0$ transition, and probe at $34904 cm^{-1}$). The image is acquired by summing up signals from 75000 laser shots, power normalized and background subtracted. The ions show a very limited spatial distribution and are peaked around the centre. It demonstrates how the speed acquired by phenol fragment upon dissociation is extremely low

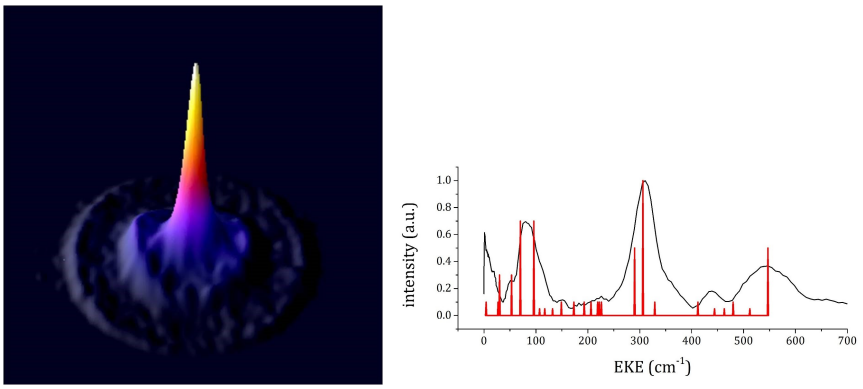

Figure 4.2: *Photoelectrons from resonant 2 photon ionization of phenol-water complex through the band of the $S_1 \leftarrow S_0$ electronic transition ($64568cm^{-1}$ total excitation energy). 3D reconstruction of the photoelectron image (left) on the 2D detector in use. False colours are used to represent the changes in intensity. Also, the experimental photoelectron kinetic energy spectrum (continuous line) is compared with the calculated one (stick plot), based on ZEKE data.*[29]

(due both to energy and momentum conservation). The peak width is very close to the experimental resolution. A magnification of the image could be realized by lowering the voltages in the electrostatic lens, but the drastic decrease in detection efficiency made this unpractical in this case.

In Figure 4.4 we report the radial distribution curves for fragments deriving from dissociation of the phenol-water cluster in the ionic potential surface. The curves are almost identical to the instrumental function of the imaging spectrometer, as obtained by the collection of bound phenol-water cluster ions (Fig. 4.4, inset). This demonstrates how the radial speed distribution is not a good parameter for the description of the dissociation dynamics of indicator for this class of molecular clusters, given the unfavourable mass ratio between the two fragments.

In Figure 4.5 we report the total yield of phenol cation production at

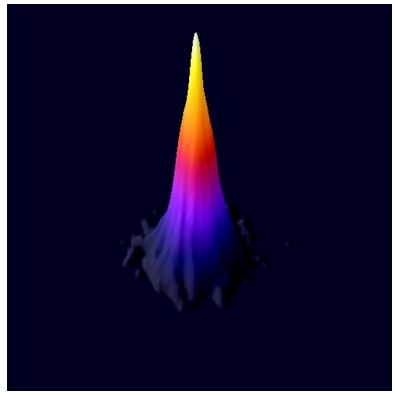

Figure 4.3: *Phenol ion produced from resonant 2 photon ionization of phenol-water complex through the band of the $S_1 \leftarrow S_0$ electronic transition with total excitation energy of $70900cm^{-1}$. 3D reconstruction of the photoelectron image on the 2D detector in use. False colours are used to represent the changes in intensity. The intensity distribution goes to zero at about 30 pixels radius.*

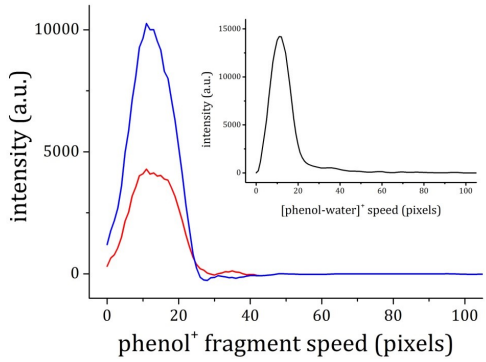

Figure 4.4: *Plot of the radial distribution of phenol ionic fragments from excitation of the phenol-water cluster at 70900 and $70718cm^{-1}$ through R2PI processes via the $S_1 \leftarrow S_0$ transition (stronger and weaker signal respectively). In the inset, the radial distribution of the phenol-water parent ions provides a measure of the instrumental resolution.*

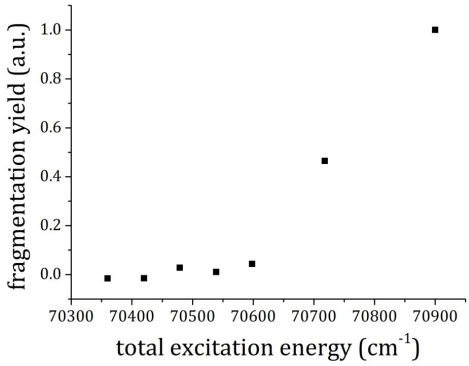

Figure 4.5: *The total phenol ion yield upon dissociation of the phenol-water cluster after its excitation above the ionization threshold through R2PI processes via the $S_1 \leftarrow S_0$ transition.*

different excitation energies. The experiment is carried-out using the usual 2-photon 2-colour resonant excitation scheme. The total yield is obtained integrating over the complete range of observed velocity for this fragment, after background subtraction. It can be immediately noticed how this signal is negligible for total excitation energy below $70600 cm^{-1}$ and then it raises with the total excitation energy. This is a measure of the appearance energy E_a for fragments upon ionization of the cluster. The binding energy BE for the ionic cluster is then readily obtained

$$BE = E_a - IP \tag{4.2}$$

and it results $6586(60) cm^{-1}$ in very good agreement with the value reported, $6520(50) cm^{-1}$.[6] The binding energy of the phenol-water cluster in the electronic states involved in the excitation process can be derived thanks to the simple level scheme reported in Fig. 4.6.

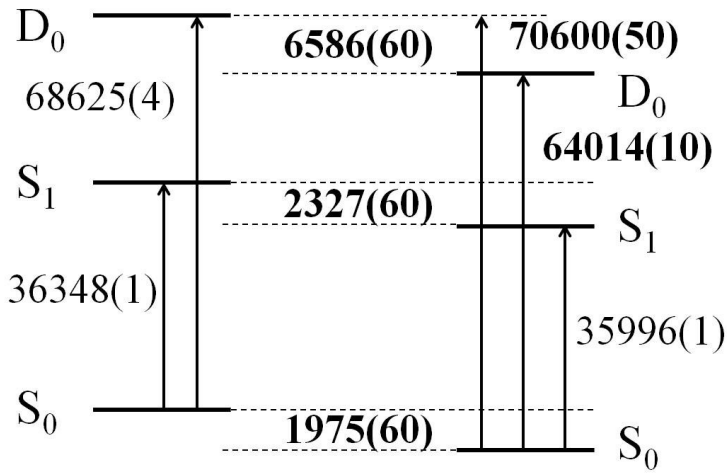

Figure 4.6: *Scheme of the relevant electronic energy levels of phenol and phenol-water cluster. Data reported in bold are from the present experiment.*

The reported results are quite relevant for a critical revision of the data we presented on the anisole-dimer.[20] Despite the structural difference between the two systems they share some relevant common feature. In both cases the binding energy is quite large (about $1800cm^{-1}$ or $5kcal/mol$), a large decrease of the ionization potential is observed for the cluster with respect to the bare chromophore and small FC factors for ionization exist, related to a large change in the equilibrium geometry between the neutral and ionic states. The appearance of fragment ions and the change in their production yield with the probe photon energy in the R2PI experiment is a good indicator for the determination of the cluster dissociation threshold. Due to the unfavourable FC factors for transitions from the vibrationless S_1 state to the high-lying cationic vibrational states at $\sim 6500cm^{-1}$ no sharp resonances are observed in the mass analyzed threshold ionization

experiments. This was shown in MATI experiments by Neusser for phenol-water.[6] In this situation a scan over a large spectral regions around the dissociation threshold can be quite tedious, given the small FC factors and the lack of clear resonances. Long data acquisition of the dissociation yield at a few different excitation energies are possibly simpler to perform and the results have a much similar accuracy in the determination of the onset of the process. If the measurement is made on an imaging detector a possible advantage is represented by the determination of the recoil speed of fragments, a parameter that goes to zero at the dissociation onset. In the case of phenol-water the large mass difference between the two fragments leads to a very small recoil speed for the detected phenol fragment, below the instrumental resolution. In the case of anisole dimer the recoil speed was measured and converged to zero at the same excitation energy as the fragmentation quantum yield. In that case, the two contemporary determination of the onset for dissociation was a clear demonstration that the experiment provided a real threshold for the process and was not limited only by the unfavourable FC factors. The discrepancy between the experimental and theoretical data could then be related to the existence of a "dark channel", a sink for excitation energy that becomes unavailable for dissociation. Under this hypothesis the dissociation of the anisole dimer should be seen as a not completely statistical process leading to the production of fragments with significant internal excitation. Further researches are under way both on the theoretical and experimental side.

Conclusions

The reported data clearly demonstrate how ion imaging experiments in velocity mapping conditions can be successfully used for determination of

the appearance energy of fragments upon ionization of a molecular cluster formed by two strongly interacting polyatomic molecules. The ion yield as a function of the total excitation energy is a good parameter for the monitoring of the process. Instead, the determination of the maximum kinetic energy available upon dissociation is not always a good indicator as, in unfavourable cases, the limited velocity acquired from the ionic fragments falls below the experimental resolution. Previous reports on aromatic dimers or complexes formed by aromatic molecules and argon atoms were not limited by this factor as the relative masses of the two fragments are much similar[18–20] than in the case of phenol-water.

The binding energy determined for phenol-water cluster by velocity mapping ion imaging experiments is in very good agreement with previous results obtained by high resolution spectroscopic methods, $1975(60) cm^{-1}$ vs $1916(30) cm^{-1}$[6] for the S_0 state, and $6586(60) cm^{-1}$ vs $6520(50) cm^{-1}$[6] for the ionic ground state D_0.

Bibliography

[1] M. Gerhards, M. Schmitt, K. Kleinermanns and W. Stahl, *The Journal of chemical physics*, 1996, **104**, 967–971.

[2] T. Ebata, A. Fujii and N. Mikami, *International journal of mass spectrometry and ion processes*, 1996, **159**, 111–124.

[3] S. Sato and N. Mikami, *The Journal of Physical Chemistry*, 1996, **100**, 4765–4769.

[4] A. L. Sobolewski and W. Domcke, *The Journal of Physical Chemistry A*, 2001, **105**, 9275–9283.

[5] O. Dopfer, G. Reiser, K. Müller-Dethlefs, E. W. Schlag and S. D. Colson, *The Journal of chemical physics*, 1994, **101**, 974–989.

[6] J. Braun, T. Mehnert and H. Neusser, *International Journal of Mass Spectrometry*, 2000, **203**, 1–18.

[7] K. Müller-Dethlefs and P. Hobza, *Chemical reviews*, 2000, **100**, 143–168.

[8] C. E. Dessent and K. Müller-Dethlefs, *Chemical reviews*, 2000, **100**, 3999–4022.

[9] H. Neusser and H. Krause, *Chemical Reviews*, 1994, **94**, 1829–1843.

[10] X. Zhang, J. M. Smith and J. Knee, *The Journal of chemical physics*, 1992, **97**, 2843–2860.

[11] M. S. de Vries and P. Hobza, *Annu. Rev. Phys. Chem.*, 2007, **58**, 585–612.

[12] D. W. Pratt, *Annual review of physical chemistry*, 1998, **49**, 481–530.

[13] M. Biczysko, G. Piani, M. Pasquini, N. Schiccheri, G. Pietraperzia, M. Becucci, M. Pavone and V. Barone, *The Journal of chemical physics*, 2007, **127**, 144303.

[14] M. Pasquini, N. Schiccheri, G. Piani, G. Pietraperzia, M. Becucci, M. Biczysko, M. Pavone and V. Barone, *The Journal of Physical Chemistry A*, 2007, **111**, 12363–12371.

[15] E. G. Robertson and J. P. Simons, *Physical Chemistry Chemical Physics*, 2001, **3**, 1–18.

[16] Y. Haas and S. Kendler, *Israel journal of chemistry*, 1997, **37**, 427–438.

[17] A. T. Eppink and D. H. Parker, *Review of Scientific Instruments*, 1997, **68**, 3477–3484.

[18] S. M. Bellm, J. R. Gascooke and W. D. Lawrance, *Chemical Physics Letters*, 2000, **330**, 103–109.

[19] S. M. Bellm, R. J. Moulds and W. D. Lawrance, *The Journal of Chemical Physics*, 2001, **115**, 10709–10717.

[20] F. Mazzoni, M. Pasquini, G. Pietraperzia and M. Becucci, *Physical Chemistry Chemical Physics*, 2013, **15**, 11268–11274.

[21] G. Pietraperzia, M. Pasquini, N. Schiccheri, G. Piani, M. Becucci, E. Castellucci, M. Biczysko, J. Bloino and V. Barone, *The Journal of Physical Chemistry A*, 2009, **113**, 14343–14351.

[22] R. J. Lipert and S. D. Colson, *The Journal of chemical physics*, 1988, **89**, 4579–4585.

[23] H. H. Tsui and T. van Mourik, *Chemical physics letters*, 2001, **350**, 565–572.

[24] Y. C. Park and J. S. Lee, *BULLETIN-KOREAN CHEMICAL SOCIETY*, 2007, **28**, 386.

[25] G. Piani, L. Rubio-Lago, M. A. Collier, T. N. Kitsopoulos and M. Becucci, *The Journal of Physical Chemistry A*, 2009, **113**, 14554–14558.

[26] M. Pasquini, G. Piani, F. Mazzoni, G. Pietraperzia and M. Becucci, *Journal of Molecular Structure*, 2011, **993**, 510–515.

[27] G. Berden, W. L. Meerts, M. Schmitt and K. Kleinermanns, *The Journal of chemical physics*, 1996, **104**, 972–982.

[28] S. Manzhos and H.-P. Loock, *Computer physics communications*, 2003, **154**, 76–87.

[29] O. Dopfer and K. Müller-Dethlefs, *The Journal of chemical physics*, 1994, **101**, 8508–8516.

Chapter 5

Non-Covalent Interactions in Aromatic Dimers

Much similar to the phenol water cluster with respect to the dissociation dynamics is possibly the phenol dimer. The phenol dimer was known as an hydrogen bonded complex, with a T-shaped structure, one moyety acting as a proton donor and the other moyety as a proton acceptor.[1–4] The two moyeties were identified in the electronic spectrum by different set of transitions, being the transitions of the acceptor at lower energies and the transitions of the donor at higher energies with respect to the bare phenol.[3] The photodissociation of this dimer had never been directly studied, but an estimate of the binding energies in the different ground and first excited state of the neutral and in the ionic ground state was suggested by Dopfer *et al.*,[3] based on a comparison of old condensed phase NMR measurements with their ZEKE experiments.

However, another aromatic dimer was very well known in Florence and has therefore attracted our interest: the anisole dimer.[5–7] Despite the sim-

ilar chemical composition, phenol and anisole dimer show extremely different properties. The anisole dimer was proved to be the first observed case of aromatic dimer in parallel shaped, π-stacked, centersymmetric structure. A combined theoretical and experimental study using HR-LIF spectroscopy and DFT calculations (using the M05-2X functional, opportunely parametrized to consider dispersion interactions) was performed.[5] Moreover, the electronic structure was studied: an excitonic splitting in the first electronic excited state was observed.[6] Due to this splitting, the stabilized *gerade* state correspond to the S_1 electronic state, but is not optically accessible because the transition from the ground state is symmetry forbidden. The only optically accessible state is therefore the *ungerade*, destabilized, S_2 state. The energy difference between S_2 and S_1 is the excitonic coupling and it was measured thank to a REMPI study with isotopical substitution on the two moyeties of the complex.[7]

Anyway, the measure of IP and BE of the anisole dimer was missing, and a large section of this thesis was dedicated to the accurate determination of these values.

5.1 Anisole Dimer (I)

In the first part of this chapter we report on the determination of IP and BE of the anisole dimer that was obtained using an Ion Imaging spectrometer. The experiment is a replica of what previously described for the phenol-water complex.

This work was published in Physical Chemistry Chemical Physics in 2013(DOI:10.1039/C3CP50191D).[8]

Binding energy determination in a π-stacked aromatic cluster: the anisole dimer

Federico Mazzoni, *Massimiliano Pasquini, Giangaetano Pietraperzia, Maurizio Becucci*

Abstract

The binding energies of the neutral and positively charged anisole dimer have been determined in molecular beam – laser spectroscopy experiments. This is the first report on the direct experimental determination of the binding energy for an aromatic cluster in π stacked configuration. The anisole dimer is formed by two anisole molecules superimposed in a planar arrangement and it has been proposed as a model system in which the π-stacking interaction, among other intermolecular forces, plays a relevant role. Its binding energy has been determined thanks to both velocity mapping ion/electron imaging experiments and previous spectroscopic information. The binding energy amounts to $3926(250)cm^{-1}$ *in the ground state and* $4144(250)cm^{-1}$ *in the* S_2 *(first spectroscopically accessible) electronic excited state; its value for the positively charged dimer ion increases to* $6147(250)cm^{-1}$*. These values are quite higher with respect to the results of previous DFT calculations.*

Introduction

Isolated molecules and van der Waals clusters have long been a subject of interest owing to the role they play as model systems for the study of many different molecular and supramolecular properties in a controlled environment. The combination of different experimental methods allows for

the determination of many parameters which, quite often, are strictly related one to the other. For instance, the study of molecules and clusters by rotationally resolved spectroscopy methods allows for determination of the energetics of the system, the change of its structure and large amplitude motions, all properties that are strictly related to the local changes in electron density.[9–14] Also, the stability and conformation of supramolecular aggregates are controlled by different terms in the interaction potential. Systematic studies have been published on series of clusters in which a reference chromophore was bound to different molecules allowing for the exploration of the relevance and the effects of possible interaction mechanisms.[5,6,10–19] These studies show the subtle interplay between many different interaction terms, especially when there is not a single dominant interaction (e.g. ion to dipole or hydrogen bond) that rules the system. Among other parameters, the binding energies of supramolecular systems are valuable to measure as these are quantities that can be directly evaluated by classical or ab initio methods. This could lead to more efficient modeling strategies that, ultimately, will provide a better understanding of condensed phases at a very fundamental level.

The first experimental determinations of the binding energy of molecular clusters were related to the benzene dimer[20,21] or clusters formed by aromatic molecules and rare gas atoms.[22–26] Only a few of these studies were probing the ground electronic state properties while most of them were related to potential energy surfaces of the lowest electronically excited states.[27,28] While studying photodissociation a crucial issue is the determination of the recoil energy: time of flight methods were the preferential approach for its measurement. Only in the last years velocity map imaging methods (VMI) have been applied to study the photodissociation dynamics in clusters formed by aromatic molecules with rare gas atoms or

water.[24–26] Most recently also more complicated systems have been studied with a similar approach.[29,30] Also, it is worth to remember here the studies on the dissociative photodetachment of anionic clusters that allow probing dissociation dynamics on the ground neutral potential energy surface of the system even though not starting from the ground equilibrium conformation.[31–33]

Among other molecular clusters studied so far, the anisole dimer exhibits some quite interesting features as revealed by resonance enhanced multiphoton ionization (REMPI), high resolution electronic spectroscopy and theoretical studies.[5,6] It has a centro-symmetric arrangement of the two units which lie on parallel planes. The two aromatic systems are only partially overlapped but the dispersion interaction dominates the intermolecular potential. This is shown by the decomposition of the different terms obtained by symmetry-adapted intermolecular perturbation theory calculations. For these reasons the anisole dimer has been proposed as the first cluster formed by two aromatic molecules in a π-stacking configuration observed in the gas phase.

In this work we present the experimental determination of the binding energy of the anisole dimer using a combination of previous spectroscopic information with new results from VMI of electrons and ions originating from the dissociative photoionization of the system. This is the first study on the dissociation dynamics of a large molecular cluster formed by two π-stacked aromatic molecules and provides a direct determination of the binding energy in both the ground neutral and ionic states as well as in the lowest optically accessible singlet electronic excited state.

Experimental section

The ion/electron imaging apparatus used in the present work has already been described in detail elsewhere,[34,35] here we will provide only a brief summary. Cold molecules and clusters are formed in a supersonic expansion of gas in a vacuum chamber. The expanding gas mixture is prepared by flowing helium at $300kPa$ over a reservoir of anisole (Aldrich, P.A. grade) at room temperature. A pulsed valve (General Valve series 9, $500\mu m$ diameter nozzle) with $230\mu s$ opening time is used for gas injection. The free expansion is skimmed by a $1mm$ diameter skimmer (Beam Dynamics) placed $15mm$ from the nozzle and the resulting molecular beam enters the interaction chamber. A fine alignment of the nozzle with respect to the skimmer is critical in order to select the coldest part of the supersonic expansion where the density of clusters is higher and the temperature lower. The molecular beam, once in the interaction chamber, enters the electrostatic lens used for VMI experiments[36] moving along its symmetry axis. Inside the electrostatic lens the molecular beam is perpendicularly crossed by two counter-propagating laser beams for the pump and probe experiment. The pump beam is held in resonance to the first allowed electronic transition for the different molecular species. The probe laser beam is frequency tuned in different experiments in order to ionize the excited clusters with different total excitation energy. Ions or electrons, alternatively, are then accelerated by the field of the electrostatic lens towards the imaging detector (two microchannel plates – MCP – in Chevron configuration and a phosphor screen). During their flight to the detector, these charged particles form an expanding sphere that hits the detector producing a signal that is measured in two different ways: as an electric current at the back MCP anode and as the image on the phosphor screen (due to the arrival

of charged particles in different points of the imaging detector) as taken by a CCD camera. The current signal is averaged on a $500MHz$ oscilloscope. One CCD image is acquired for each laser shot. Typically 75000 images were averaged for good statistics. During the acquisition, information is stored only for pixels with signal intensity above a certain threshold in order to remove intrinsic detector background. The averaged images are then processed with the polar onion-peeling algorithm[37] in order to reconstruct the full vectorial information on the charged particles speed distribution.

The laser system consists of two frequency doubled, narrowband dye lasers, synchronously pumped by the second harmonic of a $10Hz$ Q-switched pulsed Nd:YAG source. The pump laser is fixed on the $274.85nm$ or $276.50nm$ emission, respectively in resonance with the first allowed electronic transition of anisole[38] and anisole dimer.[5,6] The probe laser is set for operation in the range of 285.00–312.50nm for the photoionization of the excited molecular systems. Every laser beam is focused, with a $300mm$ focusing lens, on the molecular beam in the TOF spectrometer.

In order to obtain a cleaner signal, a gate is applied to the MCP detector to accept events from ions of a well defined mass-to-charge ratio during ion imaging experiments or to reject the contribution from secondary electrons (i.e. those produced by the positive ions hitting the electrodes of the electrostatic lens) for electron imaging experiments. In the first case a continuous potential of $1300V$ is applied to the MCP detector input to keep it close to the threshold for operation and then a pulse of $400V$ is applied to the detector to have it fully operational. A careful timing of the pulse allows for the selection of the ions of interest. Similarly, during photoelectron spectroscopy experiments a pulse added to the bias voltage applied to the detector allows for operations only during the first $800ns$ after the laser firing, selecting only the primary events.

The design of the electrostatic lens for VMI experiments follows the one proposed by Kitsopoulos and coworkers.[39] The voltage on the repeller is set to $\pm 3000V$ (where the sign depends on setting for experiments on ions or electrons). This allows for the acceptance on the $40mm$ MCP detector of photoproducts ejected with up to about $1eV$ kinetic energy.

Results and Discussion

We were able to measure alternatively the spatial distribution of electrons or ions generated with two photon resonance enhanced excitation of the anisole dimer. The pump laser was set at $36166cm^{-1}$ ($276.50nm$), on the origin band of the first allowed electronic transition ($S_2 \leftarrow S_0$) of the anisole dimer. Spectra with different total excitation energy were recorded varying the wavelength of the probe laser in the range 283.00–312.50nm. Then, the total energy provided to the system ranges from $72332cm^{-1}$ (in resonance enhanced 2-photon 1-colour ionization – RE2P1CI – experiments) to lower energies (resonance enhanced 2-photon 2-colours ionization – RE2P2CI – experiments) down to $68165cm^{-}1$. The same measurements were carried out also on the anisole monomer in equivalent conditions (pump laser in resonance with the origin band of the $S_1 \leftarrow S_0$ electronic transition of anisole at $274.85nm$) in order to have a precise energy calibration for our experiments. If we take the equatorial slice in the plane of the detector of the reconstructed 3D particle distribution, the distance between the point of impact of a particle and the center of the particles distribution is proportional to the modulus of particle speed. The fastest ejected electrons are those leaving the parent ion in its ground state: their kinetic energy is given by the difference between the 2-photon excitation energy and the ionization potential IP of the molecule. The photoelectron spectrum of anisole is well

known[35] and from its measurement we are able to calibrate all the different sets of data as in VMI experiments the diameter of the images does not depend on the mass of the particles but only on their kinetic energy. The calibration of a VMI experiment is the same for ions of different mass, and electrons as well, if the electrostatic lens parameters are constant (in absolute value) and the alignment is well reproducible.

Fig. 5.1 shows the electron kinetic energy (EKE) spectrum of photoelectrons emitted from the anisole dimer by RE2P1CI and RE2P2CI (via the origin band of the $S_2 \leftarrow S_0$ electronic transitions). The highest energy peaks in the two spectra (marked with an arrow) are shifted by $4200(100)cm^{-1}$, in very good agreement with the difference between the total energy provided in the experiments ($\Delta\nu = 4168cm^{-1}$). We assign these peaks as related to electrons leaving the ion in the ground state (even if its intensity is much smaller with respect to the corresponding peak for the photoelectron spectrum of the anisole monomer). This leads to the determination of an ionization potential of $64178(100)cm^{-1}$ for the anisole dimer.

The first set of VMI experiments detecting the ions produced upon photoionization of the anisole dimer were performed in resonant 2-photon 1-colour configuration (for a total excitation energy of $72332cm^{-1}$ or $8.97eV$), without mass gate. Initially, a central peak in the image was observed, built on a broad base, all features with isotropic angular distribution. That was taken as an indication that part of the anisole dimer ions survived the photoionization process (giving rise to the central peak of ions with negligible kinetic energy) but others dissociate under those excitation conditions (then forming the broad distribution observed due to the recoil energy acquired in the dissociation process). When a gate was applied to the detector turning it on alternatively at the characteristic arrival time of the anisole

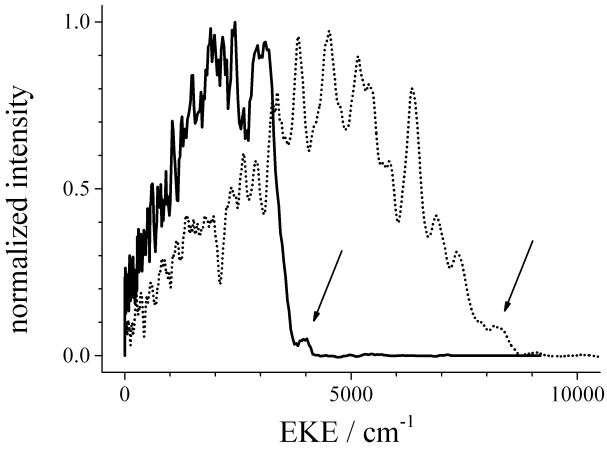

Figure 5.1: *The electron kinetic energy (EKE) spectrum after RE2P2CI (continuous line) and RE2P1CI (dotted line) of the anisole dimer (pump at* $36166cm^{-1}$*, probe at* $31998cm^{-1}$ *and* $36166cm^{-1}$*, respectively). The arrows are pointing to the highest energy peak in the two spectra, which is related to ground state ions formation.*

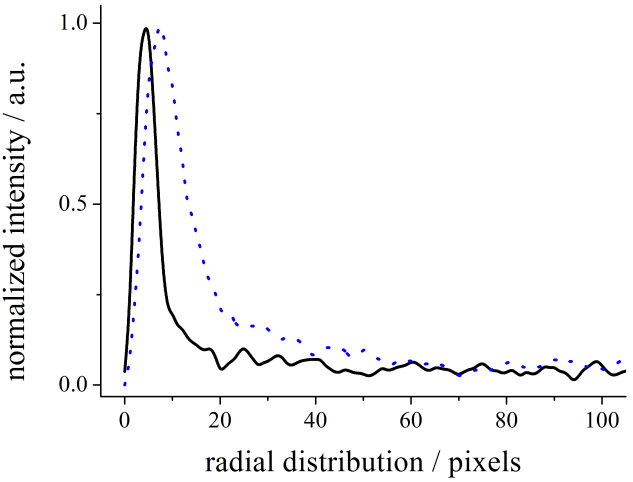

Figure 5.2: *Radial distribution of the dimer ions (solid line) or monomers ions (dotted line) generated upon photoionization of the anisole dimer clusters.*

monomer or dimer, it was possible to observe these two features separately (as shown in fig. 5.2), confirming our assignment of the central peak to the anisole dimer ions and the broad distribution to monomer ions coming from dissociation of the dimer ions.

According to the previous determination of the ionization potential of the anisole dimer, this set of experiments allows production of anisole dimer ions with internal energy up to about $7500cm^{-1}$ or $0.9eV$: an upper limit to the dissociation energy of the cation of the anisole dimer is then set because dissociation occurs under these conditions.

In order to accurately determine the binding energy of the cluster from this experiment we must have in mind that we monitor the production of the anisole parent ion and we measure its kinetic energy from recoil (which

is, by the momentum conservation law, practically equal to the one of the correlated neutral anisole fragment) but we do not know both the internal energy distribution of the two fragments produced with dissociation and the KE of the correlated photoelectron. In order to disentangle the problem we must repeat the measurement decreasing the total excitation energy down to the closure of the dissociation channel: under these conditions we assume that whatever is the distribution of energy in the dimer after photoionization the system is always below the barrier for dissociation.

We have repeated the VMI measurement of the distribution of the anisole parent ion upon photoionization of the anisole dimer at lower and lower total excitation energies. As shown in fig. 5.3, the quantum yield for anisole ion production decreases linearly with the total photon energy and the general features of the observed dynamics are not changing. Below a threshold energy, of the order of $70300 cm^{-1}$, the anisole ion yield is very low and constant. Careful measurements were needed to precisely determine the relative quantum yields for different photon energies. That was obtained carefully checking the laser power of both pump and probe beams. First the pump beam was set with pulse energy well below the threshold for 2-photon 1-color photoionization, then the probe beam was superimposed on the pump, both in space and time, and set to a power such that non-resonant 2-photon signals were completely negligible. Finally, the signals were normalized by both the pump and probe intensities. In order to check for internal consistency in the determination of the relative yields, many sets of data were taken during the same experimental session for different excitation energies. The constant signal we measured for low energy excitation at the mass of the anisole monomer ion is attributed to dissociative photoionization of larger anisole clusters in a 2 photon – 2 color process.

For the most accurate determination of the binding energy we must use

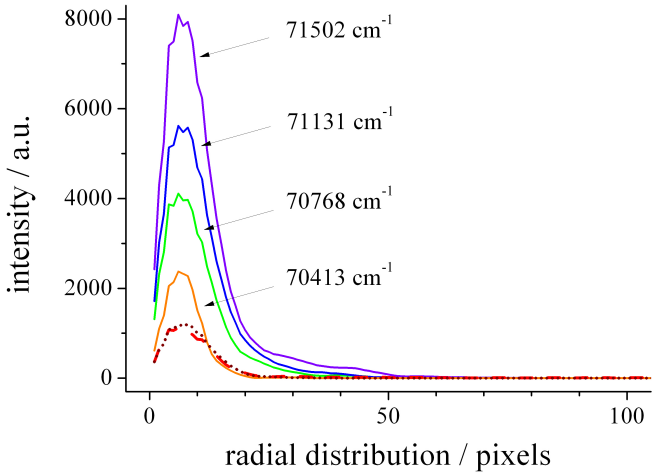

Figure 5.3: *Anisole ion radial distribution spectra after RE2P2C ionization of the anisole dimer. For high excitation energies (solid lines) the intensity of each peak increases with the excitation energy. For low excitation energies (dot and dashed lines for data at 68953 and 68165cm^{-1}, respectively) the peaks are very similar and there is no evidence of an energy dependence.*

the following equation that represents the conservation of energy in case of dissociative photoionization:

$$E = h\nu_1 + h\nu_2 = \mathrm{IP} + \mathrm{BE} + E_{\mathrm{int}} + \mathrm{TKE} \tag{5.1}$$

where E is the total available energy in the system, $h\nu_1$ and $h\nu_2$ are the energy of the pump and probe photons respectively, IP is the ionization energy, BE is the binding energy, E_{int} is the sum of the internal energies in both the neutral and ionic fragments produced, TKE total kinetic energy is the sum of KER (the kinetic energy released with the dissociation) and EKE (the photoelectron kinetic energy).

When the RE2P2C excitation provides a cluster with just enough energy to access the dissociative reaction channel in the ionic potential energy surface and dissociation occurs, then the electron is ejected with zero KE and no energy is partitioned as internal energy in the fragments (then, of course, also TKE is zero). At higher excitation energies the energy conservation law clearly indicates that dissociating ionic clusters should be associated only to very slow electrons.[32]

Fig. 5.4 shows the change in anisole parent ion quantum yield as a function of the excitation energy together with the linear fit of data in the two relevant regions, above and below the dissociation threshold. The energy at the crossing point of the two fitting lines ($70325(150)cm^{-1}$) is taken as the best possible estimate of the sum of IP and BE (both internal energy of the fragments and TKE are zero at threshold, by definition). That leads to the value of $6147(250)cm^{-1}$ for the binding energy of the positively charged anisole dimer.

Another independent determination of the binding energy comes from the measurement of the maximum KER for the molecular fragments. By

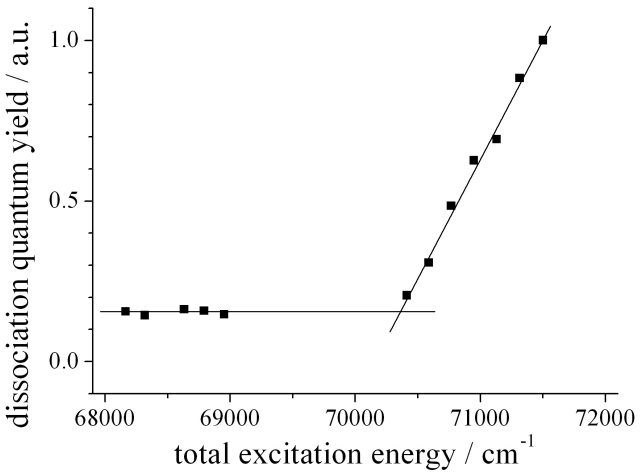

Figure 5.4: *Relative quantum yield for anisole ion production after RE2P2C ionization of the anisole dimer.*

definition, the maximum value of KER is associated to a dissociation process in which both the EKE and the internal energy in the fragments are zero. In our photoelectron spectra there is a clear evidence for production of electrons with (almost) zero kinetic energy. At the same time, there are no special reasons to think that the ground state for the fragments cannot be accessed thanks to a complete vibrational energy redistribution between the internal vibrational states initially prepared by photoexcitation and the van der Waals modes in the dimer.

Fig. 5.5 shows, in a semilogarithmic plot, the KER distribution upon dissociative photoionization at different excitation energies. In order to get the correct information, the ion KER distributions must be background corrected (i.e., we remove the ion KER distribution observed below the threshold which is attributed to the dissociative photoionization of larger anisole clusters). Fig. 5.6 shows the plot of the maximum observed KER values upon dissociative photoionization of the anisole dimer at different total excitation energies. The maximum KER values are derived from data on Fig. 5.5 by the determination of the KER value for which the ionization quantum yield decreases at a 10^{-3} signal level drop with respect to its maximum. The linear fit of the data points, shown in Fig. 5.6, indicates that zero KER (no recoil energy as to say no dissociation) should occur at $70417(200)cm^{-1}$ excitation energy. Given the value of IP, that leads to a value of $6239(300)cm^{-1}$ for the binding energy of the positively charged anisole dimer. Other authors[24] are choosing to set the maximum KER value by the determination of the KER value for which the ionization quantum yield decreases at a 10^{-4} signal level with respect to its maximum while in the present work we limit to 10^{-3} because of a limited dynamic range in the observed signal. As the signal dynamic range in the experiment limits the maximum detectable value for the kinetic energy of the fragments the

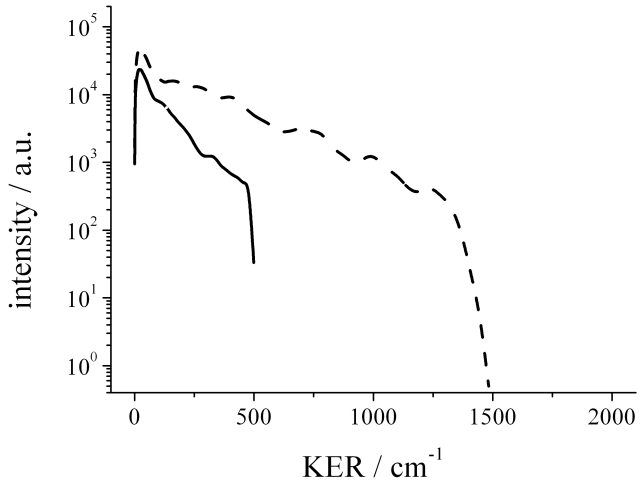

Figure 5.5: *Semi logarithmic plot of KER upon dissociative RE2P2C ionization of the anisole dimer showing exponential decay of probability for release of particles with high KE (solid lines and dashed lines for excitation at 70768 and* $71315 cm^{-1}$*, respectively).*

binding energy determined with this approach represents, more correctly, an upper limit for this parameter.

The two independent determinations of the binding energy of the positively charged anisole dimer are fully consistent within the experimental error. However, given the limitations discussed above, we assume that data derived from the quantum yield measurement of dissociation upon photoionization provide the best determination for the binding energy.

This result allows us to determine the binding energy of the anisole dimer also as a neutral system. Fig. 5.7 shows the scheme of the relevant energy levels involved in its description. The energy difference between the ground, excited and ionic state for both the anisole molecule and the

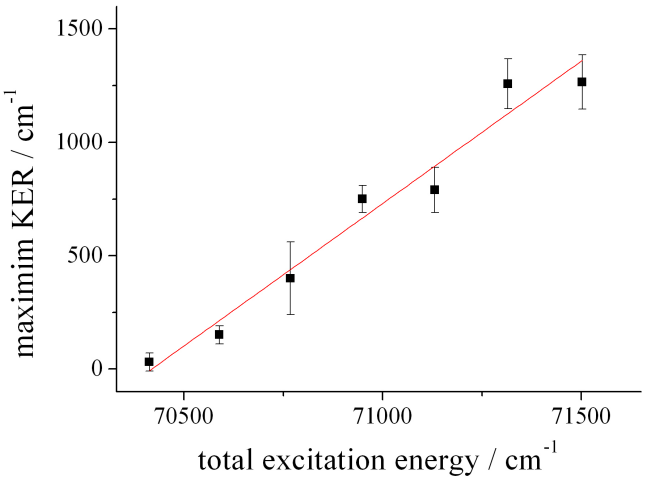

Figure 5.6: *Maximum KER release in the molecular anisole channel upon dissociative RE2P2C ionization of the anisole dimer (experimental data and linear fit). The vertical bars represent the error in the determination of the maximum KER values.*

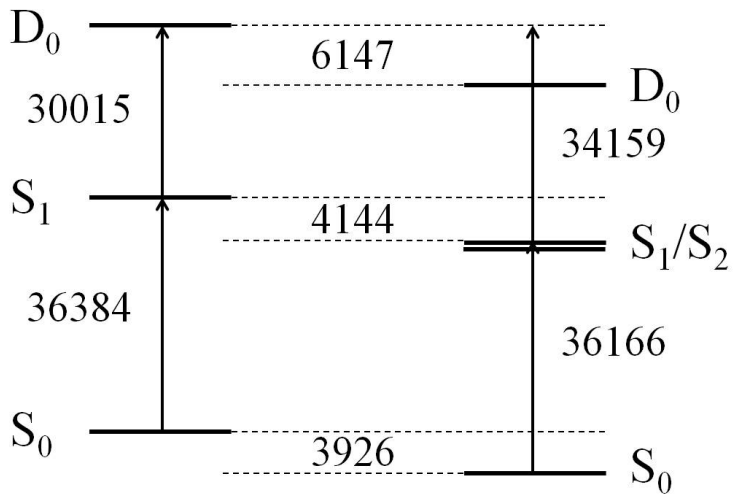

Figure 5.7: *Scheme of the relevant energy levels and excitation energies for the reference unbound system made of two anisole molecules, one in its ground state and the other in different electronic excited states (left column) and the bound anisole dimer (right column). The first singlet states and the ground ionic state (D_0) for each system are shown together with the frequency of observed spectroscopic transitions and the determined binding energies (units: cm^{-1}).*

anisole dimer are well known.[5,6,35,38] The determination of the BE for the positively charged anisole dimer allows to set the relative position of the two energy ladders. Simple combinations of these quantities allow us to evaluate the binding energy in the ground state as $3926(250)cm^{-1}$ and in the first optically allowed singlet excited state as $4144(250)cm^{-1}$. The results are summarized in Table 5.1. Recent DFT calculations on the ground state properties of the anisole dimer, carried out at the M05-2X/aug-cc-pVTZ level,[5] were reporting quite smaller values, $1480cm^{-1}$ value for the binding energy of this system in the ground state and $1806cm^{-1}$ in the electronic excited state.

Electronic State	Experimental BE/cm^{-1}	Calculated BE/cm^{-1}
S_0	3926(250)	1480
S_2	4144(250)	1806
D_0	6147(250)	

Table 5.1: *Binding energy for the π-stacked anisole dimer in its ground state, in the first optically accessible singlet electronic excited state and in the ionic ground state. Calculated values[5] were obtained in a DFT approach at the M05-2X/aug-cc-pVTZ theory level.*

Finally, we discuss the exponential decay of probability for release of fast particles during the dissociative photoionization process (as shown in Fig. 5.5). This is the characteristic signature for a statistical dissociation process. In a system like the anisole dimer, where the two moieties are not bound along a single interatomic coordinate but thanks to a partial superimposition of the molecular frames, it is difficult to imagine a single reactive coordinate which, upon direct excitation, leads to the fragmentation of the system.

The energy balance for a dissociating cluster suggests that the photoionization should occur with release of an almost zero KE electron leaving the system in a very high vibrational excited state. Most likely excitation occurs on a combination of few quanta of high energy vibrational modes (such as the C–C or C–H stretchings) in the excited electronic state. Afterwards dissociation occurs following statistical energy redistribution along the different vibrational coordinates and as soon as enough energy is in the van der Waals vibrational modes the system is above the dissociation barrier and becomes unbound. The exponential gap law for energy transfer between different molecular motions, which states that the probability of energy transfer decays as an exponential function of the energy difference between the involved levels, provides the theoretical framework for the interpreta-

tion of the present results.[40] Even though our data for the distribution of probability of KER after dissociative photoionization follow a general exponential decay law, they are not collectively described by a unique exponential decay law with a single adjustable parameter, such as, e.g., the total amount of available energy. This could be related to the specific properties of the initially prepared vibrational excited state, i.e., its anharmonic coupling to the van der Waals modes. However the dissociation quantum yield as a function of the excitation energy is, apparently, much less sensitive to the nature of the initially prepared state and a linear behavior is observed. Such a linear dependence results from the following simplified model: we assume that in a completely statistical process the distribution of probability for a given value of KER upon dissociative photoionization, for each different excitation energy, is described (in the accessible KER range) by

$$P(\mathrm{KER}, E_{\max}) \propto \exp(-\frac{\mathrm{KER}}{E_{\max}}) \tag{5.2}$$

where $E_{\max}$ is the maximum available vibrational energy in the ionized dimer (corresponding also to the maximum KER). The integration of this probability over the accessible KER range for the system is the dissociation quantum yield. Simple analytical integration shows that

$$\int_0^{E_{\max}} P(\mathrm{KER}, E_{\max}) d\mathrm{KER} \propto E_{\max} \tag{5.3}$$

which is in perfect agreement with our results (see Fig. 5.4).

This result is fully compatible with a chemical process that follows a first order kinetic law and that's definitely the case of a photodissociative process.

Conclusions

The observation of dissociative photoionization in VMI experiments provide different observables that, in combination with spectroscopic information, allows us to determine the binding energy of the anisole dimer on different electronic potential energy surfaces. The binding energy in the ground state of the neutral π-stacked anisole dimer is of the order of $0.5eV$, significantly higher than what was previously predicted on the basis of DFT quantum calculations. The dissociative photoionization process we observe for excitation energy above $70400cm^{-1}$ ($\sim 8.7eV$) is related to a statistical energy distribution among the different vibrational coordinates. The principal reaction channel after two photon resonant electronic excitation is the photoionization with the emission of a fast electron and the formation of a stable positively charged cluster. When an electron with almost zero KE is released the ionic cluster has enough energy to allow for dissociation. The momentum conservation rule suggests that the residual energy is most likely stored in internal (i.e. vibrational) coordinates. Then, as soon as IVR allows for enough energy transfer to dissociative coordinates, fragmentation occurs. This energy transfer occurs in the nanosecond regime characteristic for IVR in isolated molecules,[41] well within the timescale for our experiment. However, in very good agreement with the exponential gap law for energy transfer, only a few of the dissociating ionic clusters are able to channel all the excess energy into the translational energy release for the fragments. Both the determination of the change in quantum yield for dissociation and of the maximum KER upon dissociation allow for an accurate determination of the threshold energy for dissociative photoionization of the cluster.

5.2 Anisole Dimer (II)

As evidenced in the latter part of the previous section, a large difference between the experimental and the theoretical values of the BE was observed. Even if DFT calculations are a strong approximation for modeling π-stacking interactions, as they do not reproduce accurately dispersion interactions, the disagreement is much more than expected.

The second part of this chapter reports therefore on a different experimental and theoretical approach to the study of photodissociations in the gas phase, using a REMPI experiment with enhanced sensitivity and high level CCSD(T) calculations.

This work was accepted for publication in 2015 on Chemistry - a European Journal.

Binding energies of the π-stacked anisole dimer: new molecular beam - laser spectroscopy experiments and CCSD(T) calculations

Jan Rezac, Dana Nachtigallova, ***Federico Mazzoni****, Massimiliano Pasquini, Giangaetano Pietraperzia, Maurizio Becucci,Klaus Müller-Dethlefs, and Pavel Hobza*

Abstract

Among non-covalent interactions, $\pi - \pi$ stacking is a very important binding motif governed mainly by London dispersion. Despite its importance, for instance, for the structure of bio-macromolecules, the direct experimen-

tal measurement of binding energies in $\pi - \pi$ stacked complexes has been elusive for a long time. Only recently, an experimental value for the binding energy of the anisole dimer was presented, determined by velocity mapping ion imaging in a two-photon resonant ionization molecular beam experiment.[8] *However, in that paper, a discrepancy was already noted between the obtained experimental value and a theoretical estimate. Here, we present an accurate recalculation of the binding energy based on the combination of the CCSD(T)/CBS interaction energy and a DFT-D3 vibrational analysis. This proves unambiguously that the previously reported experimental value is too high and a new series of measurements with a different, more sensitive apparatus was performed. The new experimental value of* $1800 \pm 100 cm^{-1}$ $(5.15 \pm 0.29 kcal/mol)$ *is close to the present theoretical prediction of* $5.04 \pm 0.40 kcal/mol$. *Additional calculations of the properties of the cationic and excited states involved in the photodissociation of the dimer were used to identify and rationalize the difficulties encountered in the experimental work.*

Introduction

The dissociation energy (D_0) in non-covalently bound molecular complexes and clusters in the gas phase represents their most important fundamental characteristic. Experimental determination of this quantity is not easy as it cannot be measured directly. Experimental evaluation of the binding energy usually requires a molecular beam setup combined with multiple spectroscopic methods for inducing and detecting the fragmentation of the complex. As a result, the amount of available data is rather limited; experimental gas phase D_0 energies are now available for tens of complexes, mostly hydrogen bonded and complexes of an aromatic molecule with a

small probe. The latter complexes contain an aromatic chromophore (benzene, phenol, ...), and noble gas atom (Ar, Kr, ...), polar molecule (H_2O, NH_3 , $HCCl_3$, ...) or nonpolar hydrocarbon (CH_4, C_2H_6 ,C_3H_8 , ...).[42–51]

Another approach to the study of non-covalent complexes is the use of theoretical methods. Modern quantum-mechanical (QM) approaches reach the accuracy needed to describe intermolecular interactions quantitatively. The first and most important component of the dissociation energy, the interaction energy (potential well depth, D_e) can be defined and calculated in a straightforward manner. Among many available methods, the coupled clusters CCSD(T) approach is considered to be the most accurate and reliable method applicable to systems consisting of up to several tens of atoms. For systems of this size, an accuracy of about $1 - 3\%$ can be now reached routinely. However, in order to calculate the complete dissociation energy, further terms have to be added, namely the deformation energy accounting for changes in the geometry of the monomers upon binding, and the change in zero-point vibration energy (ΔZPVE). The latter term is difficult to calculate accurately as the proper, anharmonic vibrational analysis requires accurate description of the whole potential energy surface. As a result, the computed dissociation energies reach the accuracy of their spectroscopically determined counterparts only in the smallest model systems;[52] in the case of larger molecular complexes, the experiment still yields the most accurate binding energies available.

As noted earlier, only some classes of non-covalent complexes have been studied experimentally so far. Until recently, a system involving a $\pi - \pi$ stacking interaction was missing. Note that $\pi-\pi$ stacking interactions are of key importance in biology and the structure (and thus also function) of biomacromolecules (e.g. DNA) is mainly determined by them. Additionally, this type of interaction is rather challenging for theoretical methods and

an accurate experimental result would represent a valuable benchmark for validation of the theoretical calculations.

A first characterization of the $\pi-\pi$ stacked aromatic cluster – the anisole dimer, was performed at the LENS laboratory.[5–8] The structure of the dimer was described as parallel-displaced, stacked and centre-symmetric. A surprisingly large binding energy (D_0) was deduced from the experiment as $3926 \pm 250 cm^{-1}$ or $11.2 \pm 0.7 kcal/mol$ (throughout the paper, we use both these units as they are commonly used in the fields of spectroscopy and computational chemistry of non-covalent interactions, respectively). As the authors mentioned, the measured binding energy is much higher than the theoretical stabilization energy obtained from DFT/M05-2X/aug-cc-pVTZ calculations they performed ($4.2 kcal/mol$).

More accurate quantum-mechanical calculations presented in this article confirmed without any doubt that the true binding energy in this complex is lower than the previously reported experimental result. That conclusion initiated a new, independent attempt to determine this value experimentally. Combining the new experimental data with additional calculations has allowed us not only to obtain a new, more accurate value of D_0, but it has also allowed us to identify the properties of the system that make the measurement difficult.

The calculated binding energy presented here is based on a CCSD(T) interaction energy composed from an MP2 contribution extrapolated to the complete basis set (CBS) limit and a ΔCCSD(T) correction calculated in the aug-cc-pVDZ basis set. Before, we have shown for a set of 24 small neutral molecular clusters, the A24 data set,[53] that CCSD(T) stabilization energies are essentially already converged with respect to the order of correlation treatment. This has been demonstrated by increasing the level of theory by passing from the core-valence to an all-electron descrip-

tion, including relativistic effects, and, finally, moving from the CCSD(T) to the CCSDT(Q) level, which altogether only contribute to about a 1.5% change of the stabilization energy. In a follow-up paper[54] we have further shown that CCSDT(Q) energies are converged and passing to CCSDTQ, CCSDTQP or even to FCI levels provide negligible changes of stabilization energies. The largest source of error here is the limited size of basis sets used; the composite scheme used in this work has an average relative error of 2% in the A24 data set. Passing to D_0, the calculation of ΔZPVE is the most challenging part of the calculation. Anharmonicity generally plays an important role in non-covalent complexes and accurate theoretical D_0 energies are only obtained if ΔZPVE is calculated beyond the harmonic approximation. One should note that the ΔZPVE term becomes particularly important if some vibrations are strongly affected by formation of the complex. This is, for instance, the case for X-H...Y hydrogen bonded complexes where the X-H stretching mode is shifted to the red or blue: frequency changes can be as large as several hundred wavenumbers. On the other hand, for complexes essentially bound by dispersion energy (e.g. for aromatic stacked complexes), the interaction is not as localized as for a hydrogen bond and the vibrational modes are not affected so much by the formation of the dimer. As a result, the ΔZPVE term is rather small and its error caused by the neglect of the anharmonicity will thus not be very significant. In the present work, we use harmonic DFT calculations with empirical dispersion correction (DFT-D). Although more accurate calculations would be possible at much higher cost, the use of this approximate method introduces only rather small error ($\sim$ 0.1 kcal/mol) into the final D_0.

Calculations

In this paper the binding energy is defined to be positive; to keep this convention, we report calculated stabilisation energies which are also positive and the destabilizing terms are reported as having negative values.

Prior to the more accurate calculations, a search for the global minimum was performed at the SCC-DF-TB-D level. Multiple starting points were built and optimized, yielding a set of local minima that were re-optimized further at higher level in order to find the most stable structure.

Geometry optimization and vibrational analysis of a complex of this size cannot be performed at the CCSD(T) level and more approximate method must be used. Most often, the most economic correlated method, MP2, is employed but it is well known that it systematically overestimates the strength of $\pi - \pi$ stacking. For this reason, we resort to DFT-D, which has recently matured into a very accurate and robust approach that can treat a wide range of non-covalent interactions without systematic problems. More specifically, we use the B-LYP/def2-QZVP calculation with Grimme's D3/BJ dispersion[55,56] (referred to as DFT-D3 in the following text). It was shown that this method yields excellent results and outperforms all MP2-based approaches when tested on benchmark data sets.[57] Optimizations of the neutral dimer and the respective cation radical, calculations of their stabilisation and deformation energies as well as the vibrational analysis were carried out at this level. The resulting structure for the neutral and ionic complex are shown in Figure 5.8. For comparison, we optimized the geometry also at MP2/cc-pVTZ level, without and with counterpoise correction.[58] Deformation energies have been calculated at DFT-D3 level as the difference between subsystem energies calculated in the complex geometry and geometries of optimized isolated subsystems.

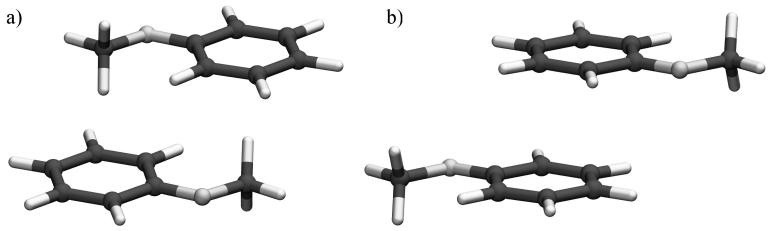

Figure 5.8: *Equilibrium structure of anisole dimer a) neutral, b) cation-radical*

The ΔZPVE energies of both dimers were calculated from harmonic vibrational analysis at the same level.

The benchmark stabilisation energy of the neutral dimer (at DFT-D3 geometry) was evaluated using the composite CCSD(T)/complete basis set (CBS) method. Specifically, the stabilisation energy was constructed as the sum of the MP2/CBS interaction energy and the ΔCCSD(T) correction term (ΔE CCSD(T) –ΔE MP2). MP2/CBS interaction energies were obtained via two-point Helgaker extrapolation of the correlation energy from aug-cc-pVTZ and aug-cc-pVQZ basis sets;[59,60] the SCF energy was taken form a aug-cc-pVQZ calculation. The ΔCCSD(T) correction was calculated with an aug-cc-pVDZ basis set. The interaction energies were corrected for the basis set superposition error (BSSE) utilizing the counterpoise correction.[58] This is the same setup we have used to construct our benchmark data such as S66x8 and X40x10.[61,62] Our tests on small model systems suggest that the error of this setup is about 3% with respect to fully converged CCSD(T)/CBS results.[53]

The excited state calculations were performed using the multi-configurational perturbation theory to the second order (CASPT2) method[63,64] in its multi-state version (MS-CASPT2);[65] throughout the study the cc-pVDZ basis set was used. This method has been shown to provide reliable description of

interacting chromophores of moderate size.[66] The active space used for calculations of the wavefunction was constructed by placing eight and seven electrons in eight orbitals for neutral and cationic anisole dimers, respectively.

Experiments

In photodissociation experiments the experimental goal is to produce detectable molecular fragments upon selective excitation of the molecular cluster. Clusters are formed by the adiabatic expansion of a gas mixture (1% anisole in helium, stagnation pressure $3 bar$) through a pulsed valve (General Valve, series 9) in a vacuum chamber. The central part of the expansion is spatially filtered in a skimmer (Beam Dynamics) and enters the measurement chamber. In order to selectively excite the cluster and produce fragments that can be easily detected, we use a R2PI (resonance enhanced two-photon excitation) scheme to produce the anisole dimer ion, as shown in Figure 5.9. A two-step excitation scheme promotes ground state clusters to the S_2 state and then above the ionization threshold. S_1 and S_2 states of the dimer are two components arising from the S_1 state of isolated anisole due to excitonic coupling; only the S_2 state is optically accessible due to the presence of a centre of symmetry in the cluster.[6] In order to observe dissociation we scan the second photon frequency and provide to the cluster a large amount of internal excitation so that the system is prepared well above the ionization threshold. The different ions eventually formed are detected by time-of-flight mass spectrometry schemes. In order to improve the experimental determination of the binding energy of the anisole dimer we have increased the sensitivity by measuring the total ion yield for both anisole dimers and anisole fragments in a conventional Wiley-McLaren

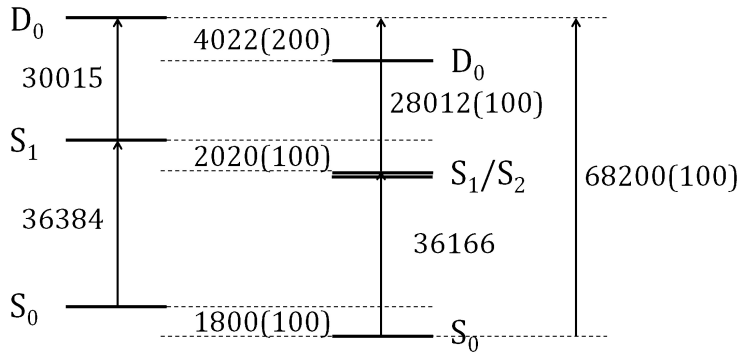

Figure 5.9: *Energy correlation diagram for anisole monomer and dimer, as derived from experimental results. S_0, S_1, S_2 correspond to different electronic singlet states, D_0 to the cationic ground state. The states are vertically displaced as a function of their relative energies, graph is not in scale. Vertical arrows represent optical transitions. In the central column the energy separation between corresponding states of monomer and dimer are reported. All values in wavenumbers, errors are reported in parentheses.*

time-of-flight mass spectrometer. Previous experiments were performed in a velocity mapping ion imaging spectrometer, which allows the measurement of the momentum of the ions but accepts only a few ions per laser shot.[8] The present spectrometer integrates the signal from all ions of the same mass and thus accepts a much larger number of ions arriving on the detector at the same time.

In order to determine correctly the binding energy of the cluster in the ground state we assume that the observed production of molecular fragments upon cluster excitation can take place efficiently with generation of fragments in their own ground state. This is the only serious limitation to the determination of the binding energy for the neutral states (either ground or excited electronic states) as all other relevant quantities are ex-

perimentally accessible with the present setup. The electronic transition frequencies for both the monomer and the cluster are known with less than $1cm^{-1}$ accuracy and the ionization threshold for the monomer is determined with similar accuracy.[5] The determination of the binding energy in the ionic state is somehow less accurate as it depends on the measurement of the cluster ionization energy. This latter experiment can be more challenging if the equilibrium geometries in the ground neutral and ionic state are very different.

Results and Discussion

Structure of the dimer. In the case of the neutral dimer, the previous experiments indicate that the structure has a centre of inversion. In our calculations multiple structures satisfying this condition were generated and optimized (although the optimization was started from structures with broken symmetry in order to find all possible minima and prevent optimizations to saddle points). The result confirms the previous findings that the dimer features two symmetric CH–π nteractions with limited $\pi - \pi$ superimposition (see Figure 5.8). To evaluate the accuracy of the geometries obtained at various computational levels, we compare the calculated principal moments of inertia with experiment. This comparison is only qualitative because the computed values were obtained in minimum energy structure, neglecting its change due to the effect of the anharmonicity in the vibrational ground state. The resulting B-LYP-D3/def2-QZVP geometry is in a perfect agreement with the experiment, the principal moments of inertia are on average within 0.6% from the experimental ones (values are presented in Table 5.2). DFT-D3 outperforms MP2 which is often used to obtain geometries of non-covalent complexes because it is the least expen-

	I''_a (umaÅ^2)	I''_b (umaÅ^2)	I''_c (umaÅ^2)
Experimental[5]	600.79(2)	1295.0(1)	1522.7(1)
M05-2X / 6-31+G(d,p)[5]	589	1297.7	1551.5
B-LYP-D3 / def2-QZVP	601.29	1289.0	1540.4
MP2 / cc-pVTZ CC	588.3	1261.7	1507.3
MP2 / cc-pVTZ	580.7	1219.7	1461.4

Table 5.2: *Comparison of the principal inertia moment of the ground state anisole dimer as derived from high resolution electronic spectroscopy, and from calculations at various levels.*

sive correlated method applicable. In this case, MP2 optimization in the cc-pVTZ basis set (recommended for $\pi - \pi$ complexes as it exhibits favorable error compensation between overbinding inherent to MP2 and basis set size effects) with and without the counterpoise correction leads to moments of inertia with errors of 1.9 and 4.4%, respectively. Even if the comparison with experiment is only qualitative, the small difference between DFT-D3 and counterpoise-corrected MP2 combined with the fact that DFT-D3 yields betterinteraction energies justifies the use of the cheaper DFT-D3 approach for the geometry optimization. The structure of the dimer cation radical was not experimentally determined and it was derived by DFT-D3 calculations. It has the same symmetry (C_i) but the binding motif is different, it is a true $\pi - \pi$ stacking structure and the methoxy groups are pointing outwards. The charge is distributed evenly between the two monomers and the reduction of electron density in the π-electron systems leads to shortening of the contact distance (measured as a distance between the plane of the benzene ring on one monomer and a centre of mass of the other one). The contact distance is 3.42Åin the neutral dimer and 3.19Åin the cation.

Energies. Computed binding and stabilisation energies of neutral and

Complex	Method	Anisole Dimer	Anisole Dimer$^+$
ΔE	CCSD(T)/CBS	6.97 ($\pm$0.21)	
	DFT-D3	7.07 ($\pm$0.71)	29.04 ($\pm$1.00)
E^{def}	DFT-D3	-0.99 ($\pm$0.10)	-2.49 ($\pm$0.25)
ΔZPVE	DFT-D3	-0.95 ($\pm$0.09)	-1.41 ($\pm$0.14)
D_0	CCSD(T)/CBS;DFT-D3	5.04 ($\pm$0.40)	
	DFT-D3	5.14 ($\pm$0.90)	25.14 ($\pm$1.39)

Table 5.3: *Total binding energies (D_0) and their components (stabilisation energy, ΔE, deformation energy, E^{def} , change of the zero point vibration energy, $\Delta ZPVE$) of the anisole dimer and its cation radical. Numbers in parentheses correspond to error estimate. All values are in kcal/mol.*

cation radical dimers are collected in Table 5.3. We also report an estimate of the uncertainty associated with the calculations. The uncertainty of the CCSD(T)/CBS interaction energy is estimated on the basis of the average accuracy of the method with respect to the benchmark data, for the other components calculated at DFT-D3 level an error of 10% is assumed (for the interaction energy in the ionic dimer, error of $1 kcal/mol$ is used instead). Stabilization energy (ΔE) in the neutral dimer is used to verify the accuracy of the DFT-D3 calculations in this particular dimer. The B-LYP-D3/def2-QZVP result is quite reliable and differs from the CCSD(T)/CBS one only negligibly, by $0.1 kcal/mol$. It gives credit to the use of DFT-D3 method for calculation of other components of the D_0 energy, for instance, the deformation and ΔZPVE energies. It also supports the reliability of the dimer geometries which were determined at this level (see also the previous paragraph). DFT-D3 stabilisation energies of neutral and cation radical dimers differ considerably and, following expectation, the latter one is much larger.

Deformation energy in the neutral dimers is close to $1 kcal/mol$ and the

harmonic ΔZPVE term has a similar value. We are aware that anharmonicity plays an important role and harmonic and anharmonic vibration modes of the dimer differ. For the evaluation of the ΔZPVE energy we need, however, the difference of zero point vibration energies of the dimer and both monomers and here we can expect cancellation of this error. Because the dispersion interaction practically does not affect electronic structure of the monomers, the intramolecular vibrations of the dimer will be similar to these in the isolated monomers and a possible inaccuracy in the description of this difference would not affect the ΔZPVE much. The ΔZPVE is thus mainly formed by six intermolecular vibrations which all are rather small. Consequently, the ΔZPVE is also small and any possible error originating both from the approximate level of calculation and from the neglect of anharmonicity will not compromise the overall accuracy of D_0.

The final D_0 energy, constructed as the sum of CCSD(T)/CBS ΔE, DFT-D3 deformation energy and DFT-D3 ΔZPVE term amounts to $5.04 kcal/mol$; if it is based only at the DFT-D3 terms it amounts to $5.14 kcal/mol$. Stabilization of the dimer originates almost exclusively from the dispersion energy; the DFT-D3 interaction energy of -7.1$kcal/mol$ is mainly determined by the dispersion energy (-9.8$kcal/mol$). Any comparison between theory and experiment requires a careful estimation the error bars on both sides. For the calculation, the error estimate described above is rather conservative, yet the resulting uncertainty in the neutral dimer is only $0.40 kcal/mol$.

In the cation dimer, the stabilisation energy is much larger: $29 kcal/mol$. The remaining terms (E def and ΔZPVE) remain similar to the ones in the neutral system. It should be also noted that the stabilisation energy in a cation radical in the geometry of the neutral system is substantially smaller at $21.8 kcal/mol$ (DFT-D3 result).

Photofragmentation experiments and results. As outlined in the pre-

vious paragraphs, in the first set of experiments we have optimized the production of the anisole dimer and determined its spectroscopic properties. Then, to determine its binding energy we prepare it in an excited state above the ionization threshold with different amounts of internal energy. The first key point in this process is that Franck-Condon factors for transitions between the S_2 excited state and the ionic state are certainly a limit for this step. Previous experiments and calculations have already shown that the geometry of the anisole dimer is quite similar in both the ground and the S_2 state. Present calculations clearly demonstrate how the equilibrium geometry of the ionic cluster is radically different with respect to that in the neutral states. Therefore, we can expect that efficient anisole dimer ion production through a R2PI excitation scheme can take place only in highly excited levels in the ionic potential energy surface corresponding to geometries much distorted with respect to the equilibrium ionic structure. The second key point is that the binding energy of the anisole dimer ion is expected to be rather large, therefore dissociation will occur only for high internal energy excitation. In a large molecular system, like anisole dimer, at high internal energy excitation the intramolecular vibrational redistribution process (IVR) is usually quite efficient and the storage of enough energy in the intermolecular modes to promote dissociation is unlikely. This factor is not so relevant for hydrogen bonded systems where a leading internal coordinate exists for dissociation. In the anisole dimer only van der Waals modes are involved in the dissociation process, as consequence the dissociation efficiency should be quite low because of energy storage in internal modes. Finally, we have experimentally demonstrated the existence of a substantial excitonic coupling in the first electronically excited state of the anisole dimer. Because the calculations predict a center-symmetric structure with even distribution of charge in the anisole dimer

cation, an excitonic splitting is expected. The second excited ionic level should therefore exist not far above the ionic ground state. In the present experiments on the anisole dimer the dissociation is taking place in excited vibrational levels far above the ionization threshold. The excitonic electronic level structure can play a role as a sink for excess excitation energy. Energy transfer between the two electronic states is allowed thanks to possibly large non-adiabatic coupling in the distorted geometry of the ionic cluster.

In the first set of experiments on the anisole dimer fragmentation we reported[8] a velocity mapping ion-imaging experiment. The production of anisole ionic fragments with different kinetic energy release was measured as a function of the excitation energy. An onset for efficient dissociation at about $70000 cm^{-1}$ total excitation energy was clearly demonstrated. Above the threshold, both the ion yield and the kinetic energy release were increasing almost linearly with the excitation energy. The independent measure of these two observables indicated the same onset for the dissociation process.

Here we present the measurement of the total anisole ion production yield as a function of the excitation energy in a conventional Wiley-McLaren time-of-flight mass spectrometer with R2PI excitation of the anisole dimer. The results are shown in Figure 5.10 for both the anisole ion and the anisole dimer ion mass channels. Both signals are recorded for resonant excitation to the $S_2 \leftarrow S_0$ electronic transition of the anisole dimer and are plotted, for better reading, while normalizing the maximum signal to 1. In absolute values, the anisole dimer ion signal is about 20 times larger than the one relative to anisole fragment ion. It indicates a very weak activity for the dissociation channel. The signal level for the anisole fragment is close to the detection limit of our apparatus.

The photoionization efficiency (PIE) of the anisole dimer in this spectral

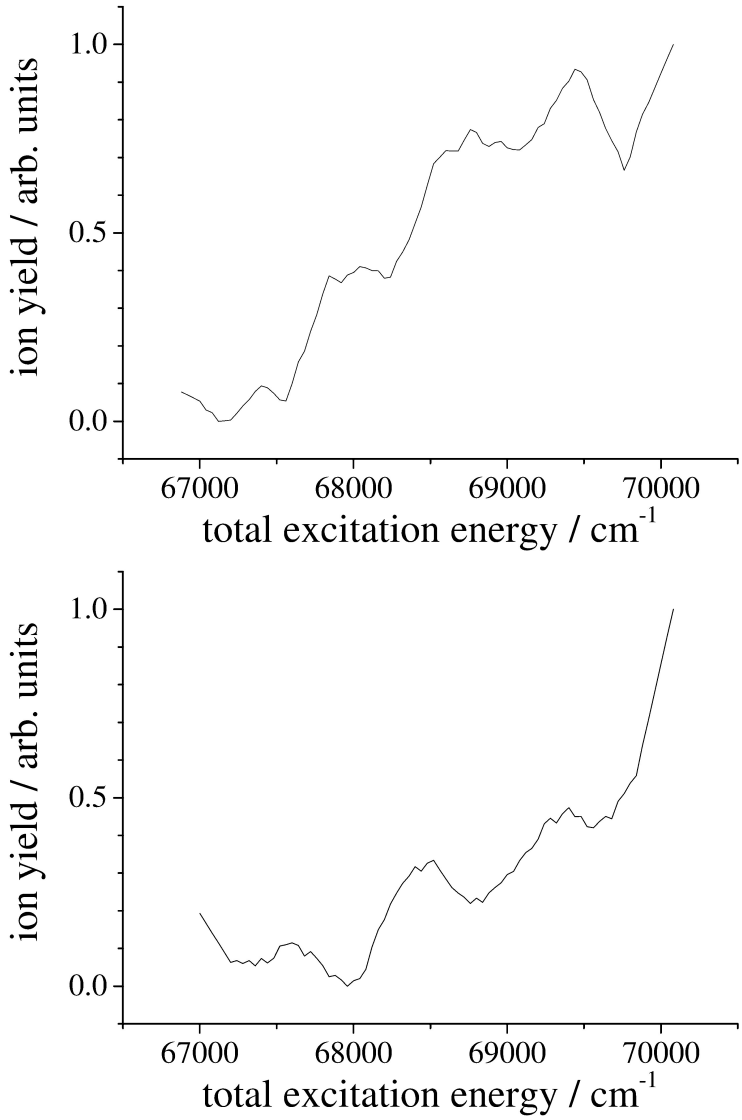

Figure 5.10: *Photoionization and photofragmentation efficiencies of the anisole dimer as a function of the total excitation energy in the R2PI experiment (top and bottom graph, respectively).*

region becomes important only above 67000 cm –1 excitation energy, well above the anisole dimer ionization energy (previously determined below $65000 cm^{-1}$). It is a clear signature of the small/negligible value of the Franck-Condon factors for ionization at threshold. The photofragmentation efficiency (PFE) shows a first small step at about $68200 cm^{-1}$ and a large step above $70000 cm^{-1}$. As the PIE signal raises at excitation energies lower than the PFE does, the excitation energy corresponding to the first step in the PFE spectrum is now taken as the new determination of the upper limit for the dissociation energy of the anisole dimer cation. As the PFE and the PIE curves show a totally different shape at higher excitation energies, the second step in the PFE curve corresponds to the opening of a more efficient dissociation pathway. The dissociation threshold determined with the previous set of measurements corresponds to the second onset observed now. In conclusion, it is very likely that the reason for the earlier discrepancy is related to the different sensitivities of the two experiments.

A reasonable hypothesis for the drastic change in the dissociation yield above $70000 cm^{-1}$ can be made assuming that the excitonic splitting for the ionic dimer provides an electronic excited state that lies below the dissociation threshold. This state cannot be reached directly by a one-photon transition from the S_2 state due to symmetry. Then the excited ionic cluster dynamics is controlled by competition between dissociative channel and relaxation to the "dark" state. As a result dissociation efficiency is strongly reduced. Only when the amount of energy provided is large enough to promote dissociation also in the electronic excited ionic state the dissociation efficiency becomes large. Under this assumption, the excitonic splitting in the ionic states D_0/D_1 can be estimated as large as $1500 - 2000 cm^{-1}$, the energy separation from the first and second thresholds in the PFE spectrum. The assumption of the large excitonic splitting is justified also by theoretical

predictions. Based on the calculations performed at the CASPT2 level, the D_0/D_1 splitting is large: $4098cm^{-1}$. This can be compared to the splitting of $266cm^{-1}$ we predict for the neutral dimer in the first electronic excited states (S_1/S_2). Such a large difference in the splitting results from different mutual orientations of the two monomers in neutral and ionic dimers (see Figure 5.8). The electronic configurations of the wavefunctions of S_1 and S_2 states are characterized by the transitions within this π-orbital space of the benzene rings. More efficient spatial overlap of this orbital space in the ionic form than in the neutral form is responsible for much higher electronic splitting in the former. We should also remark that the S_1/S_2 excitonic splitting was experimentally measured to be about $30cm^{-1}$ [6] ,the calculated values can be considered as an upper limit to the real splitting. The most relevant result is that the splitting for the D_0/D_1 states is more than 10 times larger than for the S_1/S_2 states.

The determination of the dissociation energy of the anisole dimer is based on the appearance of the anisole fragment (Figure 5.10) at $68200cm^{-1}$. We attribute this step to the onset of dissociation of the dimer cation radical and by subtracting the ionisation energy of the monomer we obtained a dissociation energy of $1800cm^{-1}$ ($5.1kcal/mol$), which compares very well with the theoretical value. In our earlier paper we attributed the strong rise in the fragment signal at $70000cm^{-1}$ to the dissociation threshold. Thanks to the improved signal-to-noise ratio of the new measurements presented here, we have been able to derive a better determination of the upper limit for the dissociation energy in the neutral dimer. In the future we are planning to extend the experiments to MATI and ZEKE measurements and we expect to obtain further improvements in the accuracy of the dissociation energy.

Comparison of experimental and theoretical D_0 energies. Present ex-

perimental and theoretical results are consistent in the determination of the dissociation energy of the anisole dimer in the ground state. The R2PI experiment allows to set the present upper limit for the dissociation of the anisole dimer in the ground state at $1800 \pm 100 cm^{-1}$ ($5.15 \pm 0.29 kcal/mol$). This compares very well with the $1760 \pm 140 cm^{-1}$ ($5.04 \pm 0.40 kcal/mol$) value obtained by the sum of CCSD(T)/CBS binding energy, DFT-D3 deformation energy and DFT-D3 ΔZPVE term. The previously reported experimental values, $11.2 \pm 0.7 kcal/mol$, can be viewed as a rough estimation of the upper limit of the dissociation energy. Two factors, the small Franck-Condon factors for preparation of the ionic cluster in R2PI experiments and the low efficiency of the photodissociation process at threshold, hampered the detection of the real onset of the process. The combination of the measured binding energy in the neutral ground state with the accurately known spectroscopic properties of both anisole monomer and dimer allows for a very good evaluation of the binding energy in the S_2 electronically excited state. It results in a slightly larger value, $2020 \pm 100 cm^{-1}$ ($5.78 \pm 0.40 kcal/mol$).

The situation is somehow different for the determination of the binding energy in the ground state of the dimer cation radical. The calculated D_0 value is rather large ($25.14 \pm 1.39 kcal/mol$ or $8793 \pm 486 cm^{-1}$). In this case we applied the DFT-D3 method and not the more accurate CCSD(T)/CBS level. The experimental value can be obtained by combining the results presented above with the measurements of the ionization potential of the anisole dimer. The previously reported value for the ionization potential of the anisole dimer is $64116 \pm 200 cm^{-1}$, leading to a value of $4022 \pm 200 cm^{-1}$ for binding energy in the ground cationic state. This large discrepancy can not be explained by insufficient accuracy of the calculations, the dominant part of the stabilization in this charged complex stems from electrostatic

and induction interactions which are covered well at the DFT-D3 level. On the other hand, the accuracy of the experimental value is limited by the possibility of accessing the real ionic ground state of the cluster. It is now quite clear that very small Franck-Condon factors make the direct optical preparation of that state in the R2PI experiment impossible. The present value of the ionization potential was deduced from the photoelectron kinetic energy spectrum. Possibly, this spectrum has almost zero intensity for the photoelectrons associated to the production of the ionic cluster in the ground state. Therefore the reported value can be taken only as a rough estimate of the lower limit of the binding energy for the ionic cluster.

Conclusions

The binding energy of the anisole dimer in different states has been newly determined in a combined experimental and computational work. The results reported for the neutral ground state, S_0 , are in perfect agreement. The accurate experimental studies on the electronic spectroscopy of both anisole monomer and dimer allow for a very good evaluation of the binding energy also in the S_2 electronically excited state. In the ground ionic state the theoretical value is still much larger than the experimental one but possible reasons for this discrepancy have been discussed.

5.3 Anisole Dimer (III)

In order to investigate the ionic states of the anisole dimer with increased accuracy and resolution, an experiment on threshold charged particles was performed. The syncronous acquisition scheme for ZEKE and MATI already described in the experimental section was used.

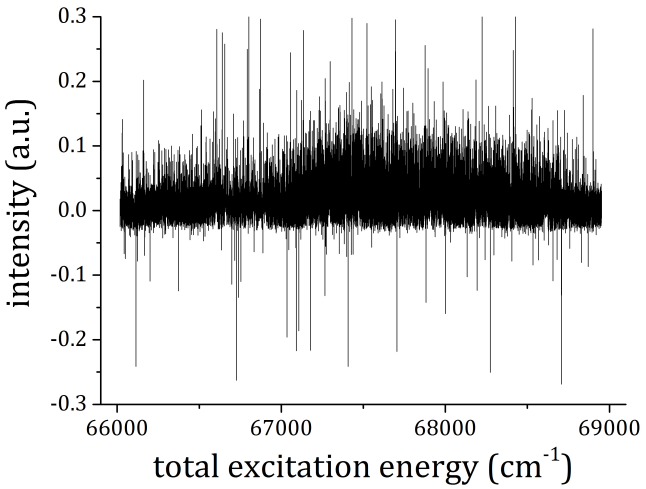

Figure 5.11: *ZEKE spectrum for total excitation energies between 66000 and* $69000cm^{-1}$*. Pump laser is in resonance with the* $S_2 \leftarrow S_0$ *transition of the anisole dimer at* $36166cm^{-1}$*. No clear ionic thresholds are evident.*

As the sensitivity for electron detection is much higher than for ions, the expected signal to noise ratio for ZEKE experiment is much higher than for MATI. Despite the high sensitivity, in the ZEKE spectrum of the dimer reported in figure 5.11 the lack of clear ionic thresholds is evident, even if a very low intensity statistical signal is observed.

As expected from the ZEKE experiment, also the MATI experiment has not provided desired results. This is in contrast with previously known systems and have no explanation at the moment, so a further analysis is necessary and we will not present here more data.

Bibliography

[1] L. Connell, S. Ohline, P. Joireman, T. Corcoran and P. Felker, *The Journal of chemical physics*, 1992, **96**, 2585–2593.

[2] M. Schmitt, M. Böhm, C. Ratzer, D. Krügler, K. Kleinermanns, I. Kalkman, G. Berden and W. L. Meerts, *ChemPhysChem*, 2006, **7**, 1241–1249.

[3] O. Dopfer, G. Lembach, T. G. Wright and K. Müller-Dethlefs, *The Journal of chemical physics*, 1993, **98**, 1933–1943.

[4] P. Hobza, C. Riehn, A. Weichert and B. Brutschy, *Chemical Physics*, 2002, **283**, 331–339.

[5] G. Pietraperzia, M. Pasquini, N. Schiccheri, G. Piani, M. Becucci, E. Castellucci, M. Biczysko, J. Bloino and V. Barone, *The Journal of Physical Chemistry A*, 2009, **113**, 14343–14351.

[6] N. Schiccheri, M. Pasquini, G. Piani, G. Pietraperzia, M. Becucci, M. Biczysko, J. Bloino and V. Barone, *Physical Chemistry Chemical Physics*, 2010, **12**, 13547–13554.

[7] M. Pasquini, G. Pietraperzia, G. Piani and M. Becucci, *Journal of Molecular Structure*, 2011, **993**, 491–494.

[8] F. Mazzoni, M. Pasquini, G. Pietraperzia and M. Becucci, *Physical Chemistry Chemical Physics*, 2013, **15**, 11268–11274.

[9] M. Schmitt, M. Böhm, C. Ratzer, C. Vu, I. Kalkman and W. L. Meerts, *Journal of the American Chemical Society*, 2005, **127**, 10356–10364.

[10] M. Becucci, G. Pietraperzia, M. Pasquini, G. Piani, A. Zoppi, R. Chelli, E. Castellucci and W. Demtroeder, *The Journal of chemical physics*, 2004, **120**, 5601–5607.

[11] B. M. Giuliano and W. Caminati, *Angewandte Chemie*, 2005, **117**, 609–612.

[12] J. Ribblett, W. Sinclair, D. Borst, J. Yi and D. Pratt, *The Journal of Physical Chemistry A*, 2006, **110**, 1478–1483.

[13] M. Pasquini, N. Schiccheri, G. Piani, G. Pietraperzia, M. Becucci, M. Biczysko, M. Pavone and V. Barone, *The Journal of Physical Chemistry A*, 2007, **111**, 12363–12371.

[14] M. Biczysko, G. Piani, M. Pasquini, N. Schiccheri, G. Pietraperzia, M. Becucci, M. Pavone and V. Barone, *The Journal of chemical physics*, 2007, **127**, 144303.

[15] G. Berden, W. L. Meerts, M. Schmitt and K. Kleinermanns, *The Journal of chemical physics*, 1996, **104**, 972–982.

[16] M. Schmitt, M. Böhm, C. Ratzer, D. Krügler, K. Kleinermanns, I. Kalkman, G. Berden and W. L. Meerts, *ChemPhysChem*, 2006, **7**, 1241–1249.

[17] M. Schmitt, C. Ratzer and W. L. Meerts, *The Journal of chemical physics*, 2004, **120**, 2752–2758.

[18] C. Eisenhardt, M. Pasquini, G. Pietraperzia and M. Becucci, *Physical Chemistry Chemical Physics*, 2002, **4**, 5590–5593.

[19] G. Pietraperzia, M. Pasquini, F. Mazzoni, G. Piani, M. Becucci, M. Biczysko, D. Michalski, J. Bloino and V. Barone, *The Journal of Physical Chemistry A*, 2011, **115**, 9603–9611.

[20] A. Kiermeier, B. Ernstberger, H. Neusser and E. Schlag, *The Journal of Physical Chemistry*, 1988, **92**, 3785–3789.

[21] J. Snodgrass, R. Dunbar and M. Bowers, *Journal of Physical Chemistry*, 1990, **94**, 3648–3651.

[22] L. M. Yoder, J. R. Barker, K. T. Lorenz and D. W. Chandler, *Chemical physics letters*, 1999, **302**, 602–608.

[23] L. M. Yoder and J. R. Barker, *Physical Chemistry Chemical Physics*, 2000, **2**, 813–821.

[24] J. R. Gascooke and W. D. Lawrance, *The Journal of Physical Chemistry A*, 2000, **104**, 10328–10335.

[25] R. K. Sampson, S. M. Bellm, J. R. Gascooke and W. D. Lawrance, *Chemical physics letters*, 2003, **372**, 307–313.

[26] S. M. Bellm, R. J. Moulds, M. P. van Leeuwen and W. D. Lawrance, *The Journal of chemical physics*, 2008, **128**, 114314–114314.

[27] M. Vernon, J. Lisy, H. Kwok, D. Krajnovich, A. Tramer, Y. Shen and Y.-T. Lee, *The Journal of Physical Chemistry*, 1981, **85**, 3327–3333.

[28] R. D. Johnson, S. Burdenski, M. A. Hoffbauer, C. F. Giese and W. R. Gentry, *The Journal of chemical physics*, 1986, **84**, 2624–2629.

[29] L. Rubio-Lago, G. Amaral, A. Oldani, J. Rodríguez, M. González, G. Pino and L. Bañares, *Physical Chemistry Chemical Physics*, 2011, **13**, 1082–1091.

[30] V. Poterya, L. Šištík, P. Slavíček and M. Fárník, *Physical Chemistry Chemical Physics*, 2012, **14**, 8936–8944.

[31] M. S. Bowen, M. Becucci and R. E. Continetti, *The Journal of Physical Chemistry A*, 2005, **109**, 11781–11792.

[32] M. S. Bowen, M. Becucci and R. E. Continetti, *The Journal of chemical physics*, 2006, **125**, 133309.

[33] F. Mbaiwa, M. Van Duzor, J. Wei and R. Mabbs, *The Journal of Physical Chemistry A*, 2009, **114**, 1539–1547.

[34] G. Piani, L. Rubio-Lago, M. A. Collier, T. N. Kitsopoulos and M. Becucci, *The Journal of Physical Chemistry A*, 2009, **113**, 14554–14558.

[35] M. Pasquini, G. Piani, F. Mazzoni, G. Pietraperzia and M. Becucci, *Journal of Molecular Structure*, 2011, **993**, 510–515.

[36] A. T. Eppink and D. H. Parker, *Review of Scientific Instruments*, 1997, **68**, 3477–3484.

[37] S. Manzhos and H.-P. Loock, *Computer physics communications*, 2003, **154**, 76–87.

[38] C. Eisenhardt, G. Pietraperzia and M. Becucci, *Physical Chemistry Chemical Physics*, 2001, **3**, 1407–1410.

[39] V. Papadakis and T. N. Kitsopoulos, *Review of scientific instruments*, 2006, **77**, 083101.

[40] R. Englman and J. Jortner, *Molecular Physics*, 1970, **18**, 145–164.

[41] K. Lehmann, G. Scoles and B. Pate, *Annual Review of Physical Chemistry*, 1994, **45**, 241–274.

[42] T. Bürgi, T. Droz and S. Leutwyler, *Chemical physics letters*, 1995, **246**, 291–299.

[43] E. Walters, J. Grover and M. White, *Zeitschrift für Physik D Atoms, Molecules and Clusters*, 1986, **4**, 103–110.

[44] J. Braun, T. L. Grebner and H. Neusser, *The Journal of Physical Chemistry A*, 1998, **102**, 3273–3278.

[45] M. Mons, I. Dimicoli, B. Tardivel, F. Piuzzi, V. Brenner and P. Millie, *The Journal of Physical Chemistry A*, 1999, **103**, 9958–9965.

[46] V. Brenner, S. Martrenchard-Barra, P. Millié, C. Dedonder-Lardeux, C. Jouvet and D. Solgadi, *The Journal of Physical Chemistry*, 1995, **99**, 5848–5860.

[47] T. Droz, T. Bürgi and S. Leutwyler, *The Journal of chemical physics*, 1995, **103**, 4035–4045.

[48] C. E. Dessent, S. R. Haines and K. Müller-Dethlefs, *Chemical Physics Letters*, 1999, **315**, 103–108.

[49] X. Tong, A. Armentano, M. Riese, M. BenYezzar, S. M. Pimblott, K. Müller-Dethlefs, S.-i. Ishiuchi, M. Sakai, A. Takeda, M. Fujii *et al.*, *The Journal of chemical physics*, 2010, **133**, 154308.

[50] S.-i. Ishiuchi, Y. Tsuchida, O. Dopfer, K. Müller-Dethlefs and M. Fujii, *The Journal of Physical Chemistry A*, 2007, **111**, 7569–7575.

[51] A. Armentano, M. Riese, M. Taherkhani, M. Ben Yezzar, K. Müller-Dethlefs, M. Fujii and O. Dopfer, *The Journal of Physical Chemistry A*, 2010, **114**, 11139–11143.

[52] J. Rezac and P. Hobza, *Journal of Chemical Theory and Computation*, 2014, **10**, 3066–3073.

[53] J. Rezac and P. Hobza, *Journal of Chemical Theory and Computation*, 2013, **9**, 2151–2155.

[54] L. Simova, J. Rezac and P. Hobza, *Journal of Chemical Theory and Computation*, 2013, **9**, 3420–3428.

[55] S. Grimme, J. Antony, S. Ehrlich and H. Krieg, *The Journal of chemical physics*, 2010, **132**, 154104.

[56] S. Grimme, S. Ehrlich and L. Goerigk, *Journal of computational chemistry*, 2011, **32**, 1456–1465.

[57] L. Goerigk, H. Kruse and S. Grimme, *ChemPhysChem*, 2011, **12**, 3421–3433.

[58] S. F. Boys and F. d. Bernardi, *Molecular Physics*, 1970, **19**, 553–566.

[59] A. Halkier, T. Helgaker, P. Jørgensen, W. Klopper and J. Olsen, *Chemical physics letters*, 1999, **302**, 437–446.

[60] A. Halkier, T. Helgaker, P. Jørgensen, W. Klopper, H. Koch, J. Olsen and A. K. Wilson, *Chemical Physics Letters*, 1998, **286**, 243–252.

[61] J. Rezác, K. E. Riley and P. Hobza, *Journal of chemical theory and computation*, 2011, **7**, 2427–2438.

[62] J. Rezac, K. E. Riley and P. Hobza, *Journal of Chemical Theory and Computation*, 2012, **8**, 4285–4292.

[63] K. Andersson, P.-Å. Malmqvist and B. O. Roos, *The Journal of chemical physics*, 1992, **96**, 1218–1226.

[64] K. Andersson, P. A. Malmqvist, B. O. Roos, A. J. Sadlej and K. Wolinski, *Journal of Physical Chemistry*, 1990, **94**, 5483–5488.

[65] J. Finley, P.-Å. Malmqvist, B. O. Roos and L. Serrano-Andrés, *Chemical physics letters*, 1998, **288**, 299–306.

[66] T. Rocha-Rinza and O. Christiansen, *Chemical Physics Letters*, 2009, **482**, 44–49.

Chapter 6

Non-Covalent Interactions in Anisole Clusters.

The last chapter of this thesis is dedicated to the anisole-Ar_n complexes, with $n = 1 - 3$. The aim of this work was first of all to test the setup for the synchronous ZEKE-MATI acquisition on a simple system, due to the non conventional results on the ansiole dimer.

Since a very poor backgorund knowledge of these clusters existed before this work, a preliminary REMPI study was performed on these three clusters and then the ZEKE-MATI experiment was tested on anisole-Ar $(1:1)$ complex.

6.1 Anisole-Ar_n (n=1-3)

The content of this chapter is going to be submitted in 2015 for the publication in an international journal.

Structure and energetics of the anisole-Ar$_n$ (n=1, 2, 3) complexes through high resolution experiments and calculations

Federico Mazzoni, *Maurizio Becucci, Jan Rezac, Dana Nachtigallova, François Michels, Pavel Hobza and Klaus Müller-Dethlefs*

Abstract

Experimental resonant two-photon ionisation (R2PI) spectra of anisole-Arn complexes with n=1-3 are compared calculations at the DFT-D3 (B-LYP/def2-QZVP level with Grimme's D3 dispersion correction)level. Structure and energetics due to microsolvation effects by the direct interaction of the argon atoms with the π-system were evaluated. The photodissociation of the (1:1) cluster was probed with a synchronous ZEKE-MATI experiment. Experimental binding energies are finally compared to computational results from CCSD/CBS calculations.

Introduction

The study of molecular clusters formed by an aromatic molecule and a rare gas in supersonic jet expansions -molecular beams- have provided many insights on the nature and strength of intermolecular forces and non-covalent interactions. For many systems, a comparison to highest level quantum calculations has been possible and, for example, complexes with benzene, aniline, phenol and other analogue molecules with argon are probably the most studied.[1–8]

Typically the first argon atom interacts directly with the aromatic electron system. The interaction energy is around 400 to 500cm^{-1} in the neutral S_0 ground state and the distance between the argon atom and the

aromatic plane is about 3.5 Å. The first allowed singlet electronic transition in the cluster is normally red shifted ($\sim 30 - 40 cm^{-1}$) with respect to that of the corresponding chromophore molecule. It indicates an increase of the interaction in the excited states, where the polarization of the aromatic system is larger.

The second argon atom is usually on the opposite side of the aromatic ring, directly interacting with the π-system and causing a doubling of the band shift for the origin of the spectrum. This is the case, for example, for phenol and aniline complexes.[5,7] Less stable conformers have also been observed with the second argon atom on the same side of the ring, resulting in small blue shifts (aniline)[7] or in negligible shifts (phenol)[8] with respect to the bare molecule.

Also clusters with three argons show two possible configurations. The most stable is usually with the three argon atoms on the same side of the ring and the relative band is blue-shifted with respect to the bare molecule. The second possible configuration is to have two argon atoms on the same side of the ring and the third on the opposite side, and its signature in the spectrum is usually red shifted with respect to the bare molecule.[5–8]

The standard experimental approach for the study of these systems is the production of the clusters in a molecular beam by adiabatic supersonic jet expansion of a suitable gas mixture and their probing with laser spectroscopic methods. The most used is the resonance enhanced two-photon ionization (R2PI) scheme, coupled with ion time of flight (TOF) mass analysis and detection. A dramatic breakthrough in the energy resolved spectroscopic studies on the ionic particles was represented by the high resolution threshold ionization experiments with detection of either electrons (ZEKE) or ions (MATI). At the same time, structural properties and large amplitude motions in these systems were probed by rotationally

resolved spectroscopic methods in the ground state (microwave absorption) and/or electronic excited states (high resolution laser induced fluorescence).

The cluster binding energy was usually experimentally derived from microwave and infrared absorption spectroscopy, single and two photons ionization, dispersed fluorescence, and stimulated emission pumping.[1,9,10]

Here we present a R2PI study on the anisole-argon clusters containing from 1 to 3 argon atoms (from now on labelled as (1:n) clusters, n=1,..,3). The solvation effects of the argon atoms to the electronic functions of the anisole have been evaluated theoretically. The equilibrium geometries of the different clusters were calculated. Moreover, we present the first application of the new method[11] for the synchronous acquisition of ZEKE and MATI signals to the anisole-argon 1:1. The binding energies in the different involved quantum states are measured and compared with theoretical values.

Methods

Experimental

R2PI and MATI-ZEKE experiments have been carried on using the same apparatus described in previous reports.[12,13] Briefly, a supersonic molecular beam is formed, using Argon as carrier gas, by means of a pulsed valve General Valve Series 9, with a $500\mu m$ nozzle. The central and coldest part of the expansion, where the concentration of clusters is higher, is selected by a $1.5mm$ diameter skimmer placed about $4cm$ from the nozzle. The resulting molecular beam is crossed perpendicularly by two co-propagating laser beams in a pump and probe experimental configuration. The excitation region is located between the electrodes of a capacitor, acting as an electrostatic lens for charged particles. The UV pulsed radiation is obtained

by the frequency doubled emission of two dye lasers synchronously pumped by a Nd:YAG laser.

For the R2PI experiment, a high positive voltage is applied to the upper electrode of the capacitor after the laser excitation, in order to push downwards the ions into the RETOF spectrometer. Ions are detected by a MCP detector.

ZEKE-MATI experiments were synchronously performed using a new setup that was developed specifically for the study of van der Waals clusters photodissociation.[11] The low voltage pulse sequence employed for the synchronous ZEKE-MATI experiment is reported in Fig. 6.1, and a brief description of this sequence is reported hereafter. About $300ns$ after the laser excitation a small positive voltage ($1.2V$) is applied to the lower armour of the capacitor in order to separate directly ionized particles from neutral Rydberg particles (Rydbergs, from now on) that still fly in the same direction of the beam: the charged particles move to the upper, grounded, part of the capacitor. Then, after $17\mu s$, a negative ($-2.4V$) very short ($200ns$) pulse is applied to the same lower armour, in order to field ionize Rydberg states. Zero Kinetic Energy electrons are produced and pushed upwards over the upper grid, where they are post accelerated (a $+10V$ accurately synchronized pulse is used) into a linear TOF and collected by an MCP. Directly produced ions, ionized and neutral Rydbergs still fly for about $3\mu s$. Then, $20.34\mu s$ after the laser excitation a high voltage positive pulse is applied to the upper electrode: Rydbergs, that are still neutral, are field ionized and pushed downwards in the RETOF. In the resulting mass spectrum two peaks will therefore appear for every species: the first one being associated to direct/spontaneous ionization, and the latter, associated to field ionized Rydberg particles.

Four mass channels have been therefore monitored to probe the disso-

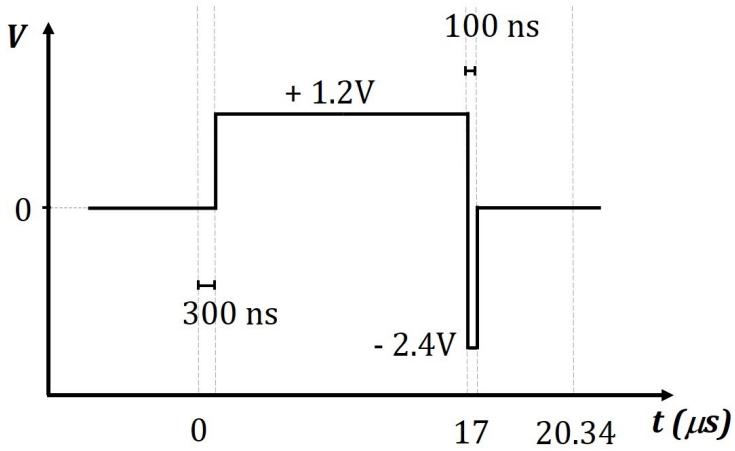

Figure 6.1: *Low voltage pulse sequence for the synchronous MATI-ZEKE experiment with a schematic view of the laser excitation and the final position of the charged particles (up) and the neutral particles (still in the beam). The zero time of the experiment is set at the laser pulse arrival time.*

ciation process of the anisole-Ar complex: two of them are related to the parent ions (R2PI and MATI signals) and the others to the ionic anisole fragments (again, R2PI and MATI signals).

Computational

Geometry optimizations, scans of the intermolecular potentials and vibrational analysis were carried out at B-LYP/def2-QZVP level with Grimme's D3 dispersion correction (we refer to this setup as to DFT-D3 in the rest of the paper).[14,15] This combination of functional and large basis set, along with the use of the Becke-Johnson damping function in the dispersion correction[16–18] had been shown to yield very accurate interaction energies. The DFT calculations were performed in Turbomole package[19] using the

resolution of identity approximation.

Interaction energies in the stationary points were calculated using the composite CCSD(T)/CBS approach with counterpoise correction for basis set superposition error. The CCSD(T)/CBS energies were obtained by combining HF/aug-cc-pVQZ energy, MP2 correlation energy extrapolated[20] from aug-cc-pVTZ and aug-cc-pVQZ basis sets and the CCSD(T) correction (defined as ECCSD(T) – EMP2) calculated in aug-cc-pVDZ basis set.

Experimental Results

The R2PI spectra of the anisole-Ar$_n$ (n=1, 2, 3) complexes have been recorded for excitation energies between 36230 and 36430cm^{-1}. In Fig. 6.2 the electronic spectra of the different complexes are compared to the origin band of the anisole electronic spectrum. For each spectrum we assign the strongest peak at lower frequency as the origin band, as it was done for similar clusters.[21] It is immediately evident that the origin bands in the electronic spectra of complexes are red shifted with respect to the origin band of anisole spectrum. The relative shifts are reported in Table 6.1. It is important to note that the band shift for the origin of the (1:2) complex spectrum is twice the one of the (1:1), while the shift for the (1:3) complex is almost the same as for the (1:2). As the spectra of the (1:2) and (1:3) clusters are very similar, we show their details in Fig. 6.3. The existing differences demonstrate that these two spectra are independent and not dominated by contamination arising from dissociation of larger clusters.

The (1:1) cluster was then studied in details with the synchronous ZEKE-MATI experiment. Contemporary ZEKE, PIE and MATI spectra have been recorded between 66100 and 66900cm^{-1} with the first laser held

	$S_1 \leftarrow S_0/cm^{-1}$	Shift/cm^{-1}
anisole	36384	-
(1:1)	36346	-38
(1:2)	36307	-77
(1:3)	36308	-76

Table 6.1: *Origin band shifts for R2PI spectra of the complexes. The shifts are calculated with respect to the bare anisole origin band.*

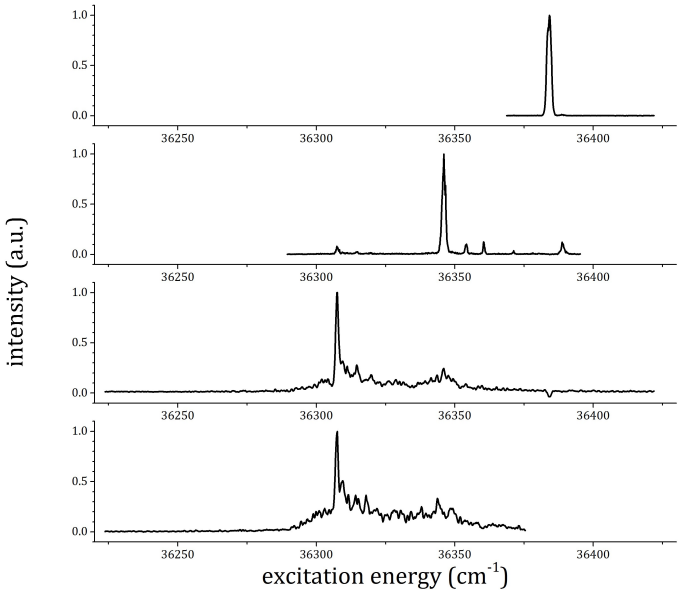

Figure 6.2: *Comparison between the observed R2PI spectra of anisole-Arn complexes. The origin band of R2PI spectrum of anisole is also reported. The probe laser is set to* $31250cm^{-1}$*. Starting from the top, the spectra refer respectively to anisole, (1:1), (1:2) and (1:3) complexes.*

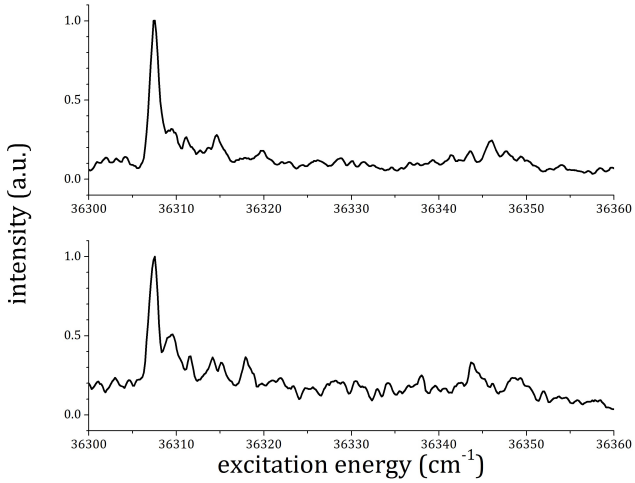

Figure 6.3: *Detail of (1:2) and (1:3) clusters R2PI spectra in the origin band spectral region. Different features are present in the two spectra, showing that both spectra are not dominated by the fragmentation of larger clusters.*

Total excitation energy/cm^{-1}	Frequency shift cm^{-1}	Total excitation energy/cm^{-1}	Frequency shift cm^{-1}
66203	0	66784	581
66222	19	66791	588 (581+7)
66238	35	66800	597 (581+16)
66253	50	66805	602 (581+21)
66266	63	66816	613 (581+32)
66279	76	66828	625 (581+46)
66292	89	-	-

Table 6.2: *Observed transitions in the ZEKE spectrum with pump laser in resonance with the origin band of the R2PI spectrum.*

in resonance with the origin band of the (1:1) cluster at $36386cm^{-1}$. The same experiment has been carried on with the pump laser in resonance with the first and the second vibronic bands. Among these data-sets, the only one showing a significant signal is the highly sensitive ZEKE with excitation through the first vibronic band, so we will not present the others. Fig. 6.4 shows the ZEKE spectra with the pump laser held in resonance with the origin band and with the first vibronic transition of the R2PI spectrum. In the first spectrum two different band sets are evident, one starting at $66203cm^{-1}$ and the second one at $66784cm^{-1}$. In the second the only transition observed in the spectrum is the one at $66203cm^{-1}$. That excitation energy is therefore assigned to the ionization potential (IP) of the complex. Table 6.2 reports all the observed transitions when the excitation occurs through the origin band of the electronic spectrum. The resulting red shift with respect to the monomer IP [22] ($66399cm^{-1}$) is $196cm^{-1}$.

In Fig. 6.5 the MATI and PIE spectra for the parent mass channel are reported. Comparing the MATI spectrum with the ZEKE one, the first set of transitions is easily recognised while the second band set is not

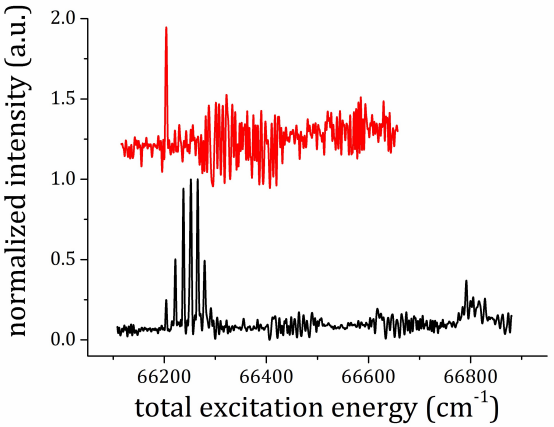

Figure 6.4: *ZEKE spectrum of the anisole-Ar complex. The pump laser is in resonance with the origin band of the R2PI spectrum at* $36346cm^{-1}$ *(lower trace) and with the first vibronic transition at* $36354cm^{-1}$ *(upper trace). The first accessible transition, corresponding to the IP of the cluster, is at* $66203cm^{-1}$.

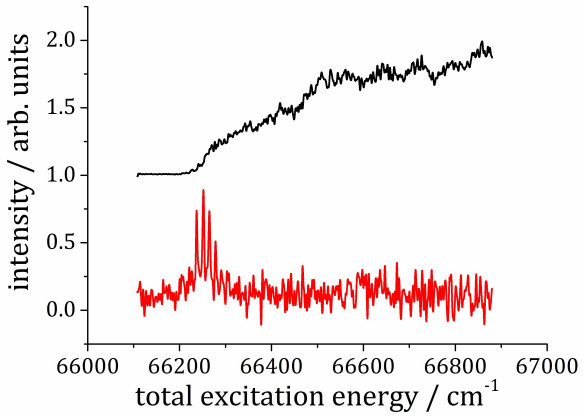

Figure 6.5: *PIE (upper trace) and MATI (lower trace) spectra recorded at the mass channel of the (1:1) cluster*

present. As usual, the signal to noise ratio is much higher in ZEKE than in MATI experiments. In Fig. 6.6 the traces of PIE and MATI spectra for the daughter mass channel are presented. In the PIE spectrum the signal starts rising above $66800 cm^{-1}$, clearly indicating the spectral region where dissociation occurs. It is important to note that the second band set in the ZEKE spectrum occurs in the same spectral region where the dissociation occurs. Probably, it is quite difficult to see the MATI signal in the fragment channel due to the low signal-to-noise ratio and to the relative weakness of this band set with respect to the first one. Anyway, by the comparison of fragment PIE and ZEKE, the band at $66784 cm^{-1}$ in the ZEKE spectrum can be taken as the upper limit for the dissociation energy of the complex, being the lowest optically accessible state in the region where dissociation occurs. This determination leads to a value of $581 \pm 5 cm^{-1}$ for the binding energy in the ionic ground state, and consequently $423 \pm 5 cm^{-1}$ in the neutral first excited state and $385 \pm 5 cm^{-1}$ in the neutral ground state, as indicated by the correlation diagram reported in Fig. 6.7.

Computational Results

Geometry of the complexes. The geometries of the complex of anisole with one and two argon atoms are well defined and can be easily optimized. Energetically most favourable binding mode is the interaction of the argon atom with the aromatic ring of the anisole; in the (1:2) complex, the two atoms are placed symmetrically on the opposite side of the ring plane (see Fig. 6.8). The third argon atom lies in the plane of the ring. To obtain all the possible positions it can occupy, we performed a scan of the potential energy surface at the DFT-D3 levels. The six minima obtained from the scan were further optimized using DFT-D3 and on the final energies,

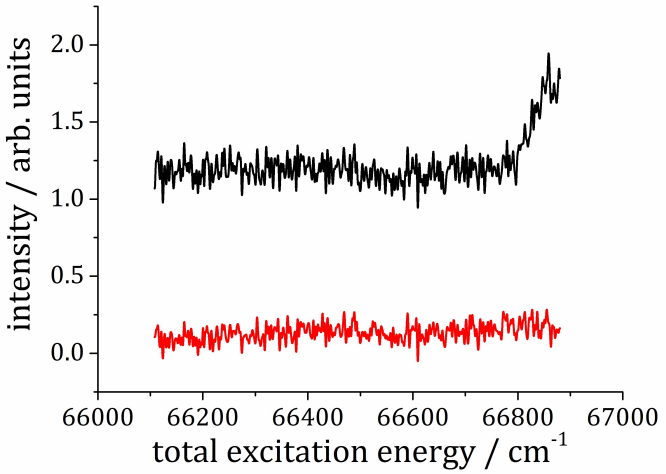

Figure 6.6: *PIE (upper trace) and MATI (lower trace) spectra recorded at the mass channel of the anisole fragment. It is clearly evident that a dissociation occurs above* $66800cm^{-1}$*. Almost no evidence for a clear dissociation threshold in the MATI spectrum is present, probably because of the low signal-to-noise ratio.*

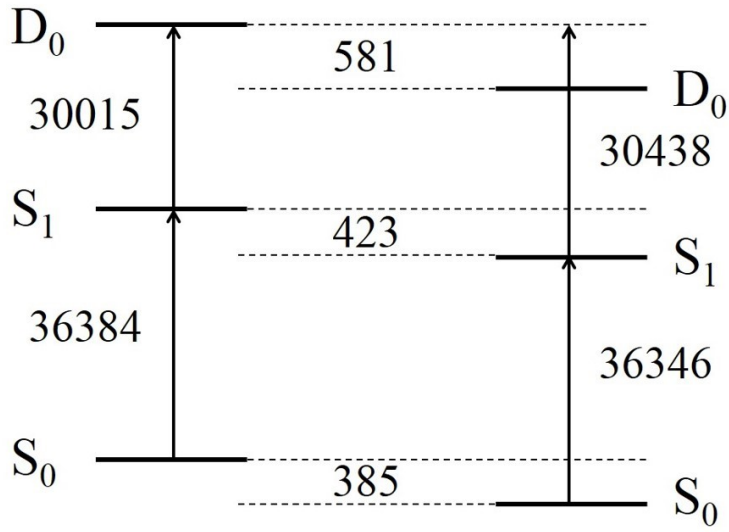

Figure 6.7: *Correlation diagram for the electronic states of anisole monomer (left) and anisole-Ar 1:1 complex (right). All values are in cm^{-1}.*

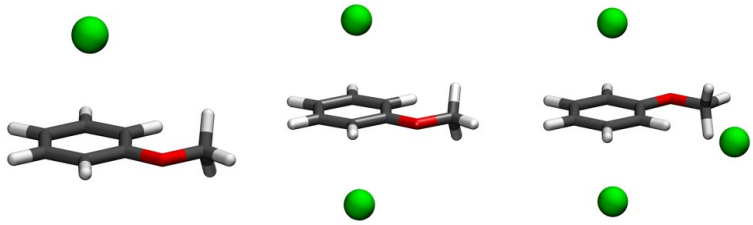

Figure 6.8: *Optimized geometries of the complexes of anisole with one, two and three argon atoms.*

interaction energies were calculated at the CCSD(T)/CBS level. The positions of the minima along with their CCSD(T)/CBS interaction energies are shown in the potential plotted in Fig. 6.9. The minima are energetically very close and the barriers separating them are very low.

The most important geometric characteristics of the complexes is the distance between the plane of the aromatic ring and the argon atoms. In the (1:1) complex it amounts to 3.524 Å. No significant change can be detected when the other argon is added at the opposite side and when the third one is added.

Anisole ··· Ar dissociation energy. For both the neutral and positively charged (1:1) complex the dissociation energy was calculated as a sum of the interaction energy ΔE, change of zero point vibrational energy ΔZPVE and deformation energy Edef (the dissociation energy is defined as positive). Table 6.3 lists the individual components as well as the final D_0 based on the CCSD(T)/CBS interaction energy. The D_0 in the neutral complex is $1.11 kcal/mol$ ($389 cm^{-1}$), in the cationic complex it amounts to $1.73 kcal/mol$ ($605 cm^{-1}$).

To test the validity of the harmonic approximation used in in the calculation of ΔZPVE, we have calculated the anharmonicity of the intermolec-

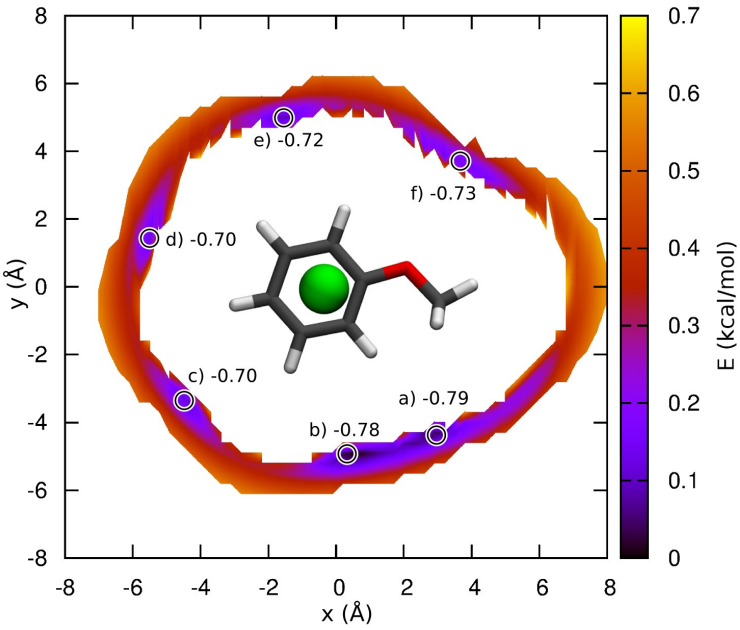

Figure 6.9: *Potential energy (in kcal/mol) of the third Ar atom added to the (1:2) complex. The six minima, labelled a) to f), were optimized and their CCSD(T)/CBS energies are provided in the plot.*

component	method	neutral	cation
ΔE	CCSD(T)/CBS	1.31	1.76
	DFT-D3	1.19	1.84
ΔZPVE	DFT-D3	-0.19	-0.02
E_{def}	DFT-D3	-0.004	-0.01
D_0		1.11	1.73

Table 6.3: *Components of the dissociation energy and the final D_0 (in kcal/mol) in neutral and cation-radical anisole-argon 1:1 complex.*

ular stretching mode which contributes to the ΔZPVE with $25cm^{-1}$. At the DFT-D3 level, we performed a scan along the normal mode and fitted it with Morse potential for which the vibrational energy levels can be expressed analytically. However, the anharmonic zero point energy in this mode differs from the harmonic one only marginally, by $-0.4cm^{-1}$.

Excited states of anisole ··· Ar(n) complexes. The results of the calculations of the calculations of the vertical energies of the lowest excited states of anisole... Ar(n) complexes are shown in Table 6.4. For all complexes, the wavefunction of the first excited state is characterized mainly by HOMO (π) $\rightarrow$ LUMO (π*) electronic configuration. The interaction of Ar atoms with π system of anisole decreased the excitation energies by 40 and $43cm^{-1}$ when placed from one or both sides of the aromatic ring, respectively. Only negligible shift in the excitation energy was observed when Ar atom was placed in the plane of the anisole ring. The interaction energy (with corrections for BSSE) of Ar and anisole in the first excited state of anisole... Ar complex was calculated using ADC(2) [23–25] method as -1.211*kcal/mol*. Thus, the interaction energy is about 15% larger than that of the ground stated (-1.053*kcal/mol*) interaction energy calculated at the same level.

n	ΔE_{exc}	ΔE_{shift}
0	39600	-
1	39560	-40
2	39517	-83
3	39514	-86

Table 6.4: *The vertical excitation energies (in cm$^-$1) in anisole...Ar(n) complexes. ΔE_{shift} is the difference in excitation energies with respect to anisole*

Further Discussion

The calculated geometries of (1:1) and (1:2) clusters of anisole...Ar(n) look almost the same as the most stable geometries of the corresponding aniline and phenol clusters.[5,7,8] However, the (1:3) cluster geometry shows a very peculiar feature: the most stable structure has the first two argon atoms on opposite sides of the aromatic ring while the position of the third argon is in the plane, where different minima of comparable energy exist. It is therefore possible that more than one isomer is formed and even that the third argon atom is allowed to move from one position to the other.

The microsolvation effects due to the presence of a direct interaction between the argon atom and the π-system are the same as in the case of the simplest reference systems (again, phenol and aniline) and are accurately reproduced by the quantum calculations at the used level of theory. The direct interaction results in a red shift of the electronic functions of about $40cm^{-1}$ and their effect is additive when the argon atom lie on opposite sides of the ring. In this case we can observe that the effect of the in-plane argon atom is instead negligible, as the interaction is not with the π-system, but with the σ orbitals of the hydrogens on the ring.

As the differences of the (1:1) complex structure and energetics with respect to the reference systems are negligible,[2,4] the binding energies are

extremely similar, being $385 \pm 5cm^{-1}$ in the neutral ground state ($364 \pm 13cm^{-1}$ for phenol-Ar and $380 \pm 15cm^{-1}$ for aniline) and $581 \pm 5cm^{-1}$ in the ionic state ($535 \pm 3cm^{-1}$ for phenol-Ar and $495 \pm 15cm^{-1}$ for aniline).

Conclusions

The structure and the energetic properties of the Anisole-Arn (n=1, 2, 3) complexes have been studied in the neutral and first excited state both experimentally and theoretically. R2PI spectroscopy and DFT calculations reveal that the contribution of the Ar atom to the electronic functions of the anisole ring has been highlighted. This contribution is additive for n=1 and n=2, when the Ar is positioned over the ring and is negligible for n=3 when the third Ar atom is lying somewhere else on a PES without clear absolute minima.

For the (1:1) complex the IP and the BE have been determined, with an improved ZEKE, MATI and PIE experiment. The observed BEs are all relatively smaller (about $30cm^{-1}$) with respect to the observed ones for the Phenol-Ar.

Furthermore, the BE in the neutral ground state can be reproduced accurately with quantum calculations using the M06-2X functional and the appropriate basis set. Further studies will be necessary for the BEs and the IPs of the (1:2) and (1:3) complexes.

Bibliography

[1] H. Neusser and H. Krause, *Chemical Reviews*, 1994, **94**, 1829–1843.

[2] C. E. Dessent, S. R. Haines and K. Müller-Dethlefs, *Chemical Physics Letters*, 1999, **315**, 103–108.

[3] X. Tong, A. Armentano, M. Riese, M. BenYezzar, S. M. Pimblott, K. Müller-Dethlefs, S.-i. Ishiuchi, M. Sakai, A. Takeda, M. Fujii *et al.*, *The Journal of chemical physics*, 2010, **133**, 154308.

[4] Q. Gu and J. Knee, *The Journal of chemical physics*, 2008, **128**, 064311.

[5] A. Armentano, J. Černỳ, M. Riese, M. Taherkhani, M. B. Yezzar and K. Müller-Dethlefs, *Physical Chemistry Chemical Physics*, 2011, **13**, 6077–6084.

[6] S. R. Haines, C. E. Dessent and K. Müller-Dethlefs, *Journal of Electron Spectroscopy and Related Phenomena*, 2000, **108**, 1–11.

[7] P. Hermine, P. Parneix, B. Coutant, F. Amar and P. Bréchignac, *Zeitschrift für Physik D Atoms, Molecules and Clusters*, 1992, **22**, 529–539.

[8] S.-i. Ishiuchi, M. Miyazaki, M. Sakai, M. Fujii, M. Schmies and O. Dopfer, *Physical Chemistry Chemical Physics*, 2011, **13**, 2409–2416.

[9] Y. Haas and S. Kendler, *Israel journal of chemistry*, 1997, **37**, 427–438.

[10] J. Braun, T. Mehnert and H. Neusser, *International Journal of Mass Spectrometry*, 2000, **203**, 1–18.

[11] *Michels et al., in publication*.

[12] H.-J. Dietrich, R. Lindner and K. Müller-Dethlefs, *The Journal of chemical physics*, 1994, **101**, 3399–3402.

[13] R. Lindner, H.-J. Dietrich and K. Müller-Dethlefs, *Chemical physics letters*, 1994, **228**, 417–425.

[14] S. Grimme, J. Antony, S. Ehrlich and H. Krieg, *The Journal of chemical physics*, 2010, **132**, 154104.

[15] S. Grimme, S. Ehrlich and L. Goerigk, *Journal of computational chemistry*, 2011, **32**, 1456–1465.

[16] A. D. Becke and E. R. Johnson, *The Journal of chemical physics*, 2005, **122**, 154104.

[17] A. D. Becke and E. R. Johnson, *The Journal of chemical physics*, 2005, **123**, 154101.

[18] E. R. Johnson and A. D. Becke, *The Journal of chemical physics*, 2006, **124**, 174104–174104.

[19] R. Ahlrichs, M. K. Armbruster, R. A. Bachorz, M. Bär, H.-P. Baron, R. Bauernschmitt, F. A. Bischoff, S. Böcker, N. Crawford, P. Deglmann,

F. D. Sala, M. Diedenhofen, M. Ehrig, K. Eichkorn, S. Elliott, F. Furche, A. Glöss, F. Haase, M. Häser, C. Hättig, A. Hellweg, S. Höfener, H. Horn, C. Huber, U. Huniar, M. Kattannek, W. Klopper, A. Köhn, C. Kölmel, M. Kollwitz, K. May, P. Nava, C. Ochsenfeld, H. Öhm, M. Pabst, H. Patzelt, D. Rappoport, O. Rubner, A. Schäfer, U. Schneider, M. Sierka, D. P. Tew, O. Treutler, B. Unterreiner, M. von Arnim, F. Weigend, P. Weis, H. Weiss, N. Winter, TURBOMOLE 6.5; Universität Karlsruhe, 2009. Available at: http://www.turbomole.com.

[20] T. Helgaker, W. Klopper, H. Koch and J. Noga, *The Journal of chemical physics*, 1997, **106**, 9639–9646.

[21] M. Becucci, G. Pietraperzia, N. Lakin, E. Castellucci and P. Bréchignac, *Chemical physics letters*, 1996, **260**, 87–94.

[22] M. Pradhan, C. Li, J. L. Lin and W. B. Tzeng, *Chemical physics letters*, 2005, **407**, 100–104.

[23] J. Schirmer, *Physical Review A*, 1982, **26**, 2395.

[24] A. Trofimov and J. Schirmer, *Journal of Physics B: Atomic, Molecular and Optical Physics*, 1995, **28**, 2299.

[25] C. Hättig, *Advances in quantum chemistry*, 2005, **50**, 37–60.

Chapter 7

Conclusions

The aim of this thesis was to investigate covalent and non-covalent bonds from a spectroscopic and photochemical point of view. As model systems, aromatic molecules (phenol, substituted phenols, anisole) and their van der Waals clusters with noble gases (Ar), small polyatomic molecules (water) and other aromatic molecules (anisole), were chosen. Time resolved and energy resolved ultraviolet spectroscopy experiments were performed on gas phase, jet cooled, samples. Using high power laser sources, non-linear multiphoton absorption was induced on the molecular systems in order to produce reactive excited electronic states.

Reactions along the O-H coordinate in the first excited S_1 state of phenol and substituted phenols (guaiacol and syringol) have been investigated in collaboration with the group of Dr. Stavros at the Warwick University. The production of H radicals through tunneling photodissociation was probed with a TR Ion Imaging approach. In the substituted phenols, it has been shown how the presence of intramolecular H-bond with the oxygen of the methoxy groups influences the dissociation dynamics, quenching

the dissociation totally in guaiacol and only partially in syringol. Moreover, it was possible to observe a quantum beat in the ionization yield of the guaiacol and syringol parent ions, i.e. their ionization yield oscillates as a function of the delay between the pump and the probe laser shots. A possible interpretation of this behavior was given, due to the difference in geometry between excited and ionic ground state. Indeed, both the S_1 excited state and the D_0 ionic ground state of phenol are similar and planar, so that the FC factors for the transition are always favorable and no quantum beat is observed. In the case of guaiacol and syringol instead, the ionic ground states are planar, while the excited states are non-planar, due to substituents lying out of plane. A combination of internal vibrations involving the torsion of substituents makes the geometry of the excited state planar at a given time. When the excited state geometry is planar, the FC factors for the absorption of UV light are large, when it is non-planar the FC factors are small.

If the hydrogen of the phenol hydroxyl group is involved in an intermolecular bond the O-H reaction coordinate is quenched as in the case of intramolecular bond. A typical example of supramolecular system where this happens is the phenol-water (1:1) cluster. In this complex a different reaction pathway is active, due to the presence of the non-covalent interaction between the two moieties. A statistical dissociation pathway through the D_0 PES was known from literature[1] for this complex and the BEs were determined with ZEKE and MATI high resolution techniques. In this work, the phenol-water cluster was used as a reference system to validate the energy resolved Ion imaging experiment in VMI setup and discuss some possible limitations. This approach allows usually for two independent determinations of the BE: one related to the total ion yield of the fragment and one related to the maximum KER of the fragment. In the first case,

for the determination of the dissociation threshold, it is necessary to repeat the acquisition of images for different excitation energies. In the latter case, it can be sufficient just one single acquisition for a given excitation energy: when the dissociation process is active, it is possible to calculate the energy excess provided to the system by the laser excitation by measuring the maximum kinetic energy release of the fragments following the energy conservation law.

The BEs of the phenol water cluster were determined with the total ion yield analysis. Their values were respectively $1975 \pm 60 cm^{-1}$, $2327 \pm 60 cm^{-1}$ and $6586 \pm 60 cm^{-1}$, for the neutral ground state, neutral first singlet excited state and ionic ground state. The agreement with data reported in literature[1,2] (1916 ± 50 in the neutral ground state and 6520 ± 50 in the ionic ground state) was excellent. Despite this, it was not possible to determine the energy with the analysis of the KER. This limitation was explained in terms of momentum conservation: as the phenol/water mass ratio is ~ 5, the maximum KER allowed for the phenol$^+$ fragments is very small in the examined spectral range and the spatial distribution of the phenol$^+$ fragments is comparable with the distribution of the parent ions.

In order to increase the degree of complexity of the examined system, an aromatic dimer was studied. As phenol dimer dissociation was already known from Dopfer *et al.*,[3] anisole dimer was chosen as model system. The choice was also due to the background knowledge of the dimer properties that was already present in Florence, where it was spectroscopically characterized.[4–6]

A first experiment was performed on the anisole dimer with the same setup that was used for the phenol-water complex. In this case, as the mass ratio between the two moieties is much more favorable than in the previous example, the two independent determinations were possible and they both

converged to the determination of a threshold at $70325 \pm 150 cm^{-1}$. From the Electron Imaging experiment the IP was estimated to be $64178 \pm 100 cm^{-1}$. Consequently the measured BEs were $3926 \pm 250 cm^{-1}$, $4144 \pm 250 cm^{-1}$, and $6147 \pm 250 cm^{-1}$ respectively for the neutral ground state, neutral first excited state and ionic ground state. Surprisingly, the difference between experimental and calculated values, was much larger than expected. The calculations at the DFT (M05-2x/aug-cc-pvdz) level predicted $1480 cm^{-1}$ for the ground state and $1806 cm^{-1}$ for the first excited state.[4] It was not possible to explain a similar difference in terms of approximations in the calculation methods and the experimental values seemed consistent, due also to the validation of the method that was made with phenol-water. A different experimental and computational approach was therefore employed. First of all, in collaboration with the computational group of professor Hobza in Prague, high level CCSD(T) calculations at the limit of the CBS were performed for an accurate evaluation of the BE in the neutral ground state. A new value of $1762 \pm 140 cm^{-1}$ was obtained. Moreover, calculations on the ionic geometry were also performed: even if the predicted structure was still centersymmetric a large difference from the neutral geometry was evidenced, leading to poor FC factors for the ionization.

Then, a REMPI-TOF experiment was performed, trying to enhance as much as possible the sensitivity of the instrument. Monitoring the fragmentation yield, two onset for the dissociation were observed. The first one, very inefficient and at excitation energies well below the ones reported in the previous work, was correlated to the effective dissociation threshold. The second one instead, was responsible for a very efficient process opening at excitation energies much similar to those reported in the previous work. Anyway, as the ionization yield of the parent and the fragmentation yield were quite different, it was not possible to relate this behavior simply

to a FC factor increasing. An explanation for the presence of this double threshold in terms of excitonic coupling in the ionic state was proposed. The dissociation immediately above the first threshold is probably quenched by the presence of a "dark" electronic state that acts as a sink for the energy; only at much higher energies the fragmentation mechanism becomes efficient. This hypothesis was supported by calculations: the presence of an excitonic coupling in the ionic state was predicted. The experimental values for the BEs were in this case $1800 \pm 100 cm^{-1}$, $2020 \pm 100 cm^{-1}$ and $4022 \pm 200 cm^{-1}$ for respectively ground and first excited state for the neutral, and ionic ground state. It is important to note that the experimental value in the neutral ground state is in excellent agreement with the computational value.

In order to investigate in depth the properties of the ionic state for the anisole dimer, a high resolution experiment was performed in collaboration with the group of professor Müller-Dethlefs, in the laboratories of the Manchester University. First of all a new setup for the synchronous acquisition of ZEKE and MATI signals was designed specifically for the study of big polyatomic clusters. The efficiency of this method was tested first of all on a single molecule like the well known anisole. After this test, the new setup was used for the anisole dimer. Unfortunately, the results of this study were controversial (the signal from ionic thresholds was missing and only a statistical signal was probed) and a possible interpretation is actually extremely difficult.

Finally, this setup was used and validated on a much simpler system as the Anisole-Ar complex. A preliminary REMPI study was performed on the anisole-Ar_n complexes, with $n = 1 - 3$ and the electronic spectrum for each species was recorded. The origin bands of the complexes resulted red shifted with respect to the origin of the bare anisole. The red shifts were

respectively $38cm^{-1}$ for the origin of the (1:1) complex, $77cm^{-1}$ for the origin of the (1:2) complex and $76cm^{-1}$ for the origin of the (1:3) complex. It is therefore evident that for (1:2) and (1:3) the red shifts are twice the red shift for the (1:1). Again, a comparison with calculation performed in Prague by the group of professor Hobza, allowed to explain this behavior in terms of microsolvation effects to the electronic functions of the anisole due to the presence of Ar atoms. In the case of the (1:1) complex the most probable calculated structure predicts a direct interaction of the Ar atom with the aromatic ring. In the case of (1:2) complex, also the second Ar atom directly interacts with the ring, but on the opposite side with respect to the first one, in a symmetric position. In the case of the (1:3) instead, the third Ar atom lies in the plane of the ring. The interaction is therefore not direct with the π-system and its influence on the electronic functions is minimal. It is not possible to determine univocally where the third Ar atom is placed, as the potential energy surface shows different minima at comparable energies that are not separated by real energy barriers. Also the red shifts of the clusters origin bands with respect to the anisole origin band were accurately reproduced by the quantum calculations, as the calculated values are respectively $40cm^{-1}$ for the (1:1) complex, $83cm^{-1}$ for the (1:2) complex and $86cm^{-1}$ for the (1:3) complex.

The synchronous ZEKE-MATI experiment on the (1:1) anisole-Ar complex was then performed. In this case, several clear ionic thresholds were observed in the ZEKE and MATI spectra. Moreover, it was possible to relate these thresholds to ionization and dissociation of the cluster. The IP was determined as $66203 \pm 4cm^{-1}$ and the BEs as $385 \pm 5cm^{-1}$, $423 \pm 5cm^{-1}$ and $581 \pm 5cm^{-1}$. The calculated BE at the CCSD(T) level is $389cm^{-1}$ in the neutral ground state and $605cm^{-1}$ in the ionic ground state, so the agreement between experiment and theory is excellent.

In summary, we investigated the photochemical reaction dynamics in different phenols and clusters involving phenol and anisole as chromophores. We have shown how much intramolecular and intermolecular interactions can affect the fission of the O-H bond or the clusters dissociation. New fundamental information were obtained experimentally on these molecular systems, thanks also to the development of new experimental methods and strategies. The results have been discussed with support of advanced quantum calculations. The overall work was made possible thanks to the collaboration with different European research groups and institutions.

Bibliography

[1] J. Braun, T. Mehnert and H. Neusser, *International Journal of Mass Spectrometry*, 2000, **203**, 1–18.

[2] O. Dopfer, G. Reiser, K. Müller-Dethlefs, E. W. Schlag and S. D. Colson, *The Journal of chemical physics*, 1994, **101**, 974–989.

[3] O. Dopfer, G. Lembach, T. G. Wright and K. Müller-Dethlefs, *The Journal of chemical physics*, 1993, **98**, 1933–1943.

[4] G. Pietraperzia, M. Pasquini, N. Schiccheri, G. Piani, M. Becucci, E. Castellucci, M. Biczysko, J. Bloino and V. Barone, *The Journal of Physical Chemistry A*, 2009, **113**, 14343–14351.

[5] N. Schiccheri, M. Pasquini, G. Piani, G. Pietraperzia, M. Becucci, M. Biczysko, J. Bloino and V. Barone, *Physical Chemistry Chemical Physics*, 2010, **12**, 13547–13554.

[6] M. Pasquini, G. Pietraperzia, G. Piani and M. Becucci, *Journal of Molecular Structure*, 2011, **993**, 491–494.